RESPONSE PREDICTION AND DAMAGE ASSESSMENT OF FLEXIBLE RISERS(Dissertation_全文)

AUTHOR(S):

Riveros Jerez, Carlos Alberto

Response Prediction and Damage Assessment of Flexible Risers

Carlos Alberto Riveros Jerez

Department of Civil and Earth Resources Engineering

Kyoto University

A thesis submitted for the degree of

Doctor of Engineering

September 2008

THIS THESIS IS DEDICATED TO GOD AND HIS PROPHETS
KELIOM Y SHAMAH

Acknowledgements

I would like to express my deepest gratitude to my advisor, Dr. Tomoaki Utsunomiya, for teaching me so much over the past three years and for inspiring me with the example of his hard work and his intensity. Thank you for all the knowledge and experience that you have shared with me so freely and for giving me the exposure and the opportunities that have helped my career. Without his guidance, none of this would be possible. I would also like to extend my deepest gratitude to Dr. Katsuya Maeda of NMRI and Dr. Kazuaki Itoh of JAMSTEC for their continuous support and guidance throughout the research presented in this thesis.

I am also extremely grateful to Dr. Yozo Fujino of Tokyo University for his supervision, support, encouragement, and understanding in various aspects during my master studies. I am also greatly indebted to Dr. Eiichi Watanabe for his encouragement and motivation. I would also like to extend my appreciation to my committee members: Dr. Kunitomo Sugiura and Dr. Hiromichi Shirato for their valuable contributions to the successful completion of this thesis.

I would like to thank Mr. Mitsuyoshi Takahashi and Mr. Masahiro Yoshida for giving me the opportunity to experience japanese budo. Also warmest thanks must go to my host family in Tokyo, Mr. Tetsuo Kato and Ms. Kyoko Kato, whose patience, invaluable support, and impeccable understanding allowed me to have a wonderful experience in Japan and write this thesis. I also would like to thank my host family in Kyoto, Mr. Meiji Anahara and his wife, for their encouragement and support.

Thanks to the people of the Structural Mechanics Laboratory. Special thanks to Beatriz Wills for her constant support; it was invaluable. Also special thanks to Mr. Edwin Garcia, Mr. Abbas Khayyer, Mr. Carlos Palacio and Mr. Hiroshi Ogura for their kindness and continuous support. Thanks to Carlos Sanchez and Daniel Canas for the support they have given me. I extend my thanks to the Ministry of Education, Culture, Sports, Science and Technology (Government of Japan: MEXT) for the financial support to make this study as possible.

Finally, on the personal level, there are no words that can adequately express my deep gratitude to my mother, she is simply perfect. I cannot ask for more from my mother. Her love and encouragement during my studies provided the solid foundation of this work. Mother, I love you. Thank you very much for your incredible support, everalsting love, special care and patience. I would also like to give a special mention to my brother Javier, who has been always my best friend and an incredible source of inspiration and encouragement. Heartful thanks to Sandra and Franchesca for their unconditional love and continuous support. To my beloved Avash for all her love, care, patience and inspiration, which have been essential for the completion of this thesis. I love you all. Thank you for believing in me.

Kyoto, August 2008

Carlos Alberto Riveros Jerez

Abstract

Several research efforts have been directed toward the development of models for response prediction of flexible risers. The main difficulties arise from the fact that the dynamic response of flexible risers involves a highly nonlinear behavior and a self-regulated process. This thesis presents a quasi-steady approach for response prediction of oscillating flexible risers. Amplitude-dependent lift coefficients and an increased mean drag coefficient model during synchronization events are considered. Experimental validation of the proposed model is carried out using a 20-meter and a 35-meter riser models. Large variations in hydrodynamic force coefficients, a low mass-ratio value and synchronization events are the main features of the models presented in this thesis. Numerical results are compared with experimental data showing good agreement in amplitude response. In the second part of this thesis, a statistical pattern recognition technique based on time series analysis of vibration data is presented. Structural damage is associated with fatigue damage. Therefore, hinge connections are used to represent several damage scenarios. Then, the statistical pattern recognition technique is employed to identify and locate structural damage using vibration data collected from sensors strategically located. A modal-based damage detection approach is also numerically implemented and its results are compared with the ones obtained from the statistical pattern recognition technique. Similar comparisons are conducted using a nonlinear principal component algorithm for fault detection. The comparative study shows that the statistical pattern recognition technique performed the best and that damage in oscillating flexible risers can be assessed using the presented statistical pattern recognition technique.

Contents

List of Figures

List of Tables

Nomenclature

Roman Symbols

a	lower limit of beam element
B	width of the computational domain
b	upper limit of beam element
c	ARX first limit
D	diameter of cylinder
d	ARX second limit
f	flow oscillation frequency in the in-line direction
H	Hankel matrix used for system identification
L	length of riser
S	frontal area of a body measured orthogonal to streamwise
s	Mahalanobis distance covariance
T	time period
t	time
U	mean uniform flow velocity
v	instant velocity moving cylinder

w	submerged weight of riser
x	x-axis the direction of the flow velocity
y	y-axis cross-flow direction
Y	Markov's parameter used for system identification
z	z-axis same direction of axis of riser

Greek Symbols

β	beta parameter defined as Re/KC
Δ	small increment
E_x	ARX residual error healthy state
E_y	ARX residual error after damage
γ	damage index defined for deterministic damage detection
ϕ_{drag}	phase of the drag with respect to cylinder's displacement
μ	mean value of time series
ν_i	ARX first coefficients
ω	natural frequency of structure without fluid surrounding
ϕ	phase angle transverse force
π	$\simeq 3.14159\ldots$
ρ	fluid density
ϕ_{lift}	phase angle with respect to cross-flow
ψ	mode shape of riser
σ	standard deviation of time series
τ_j	ARX second coefficients

$\theta(z)$ initial phase angle for long flexible riser

Υ peak-to-peak amplitude in the cross-flow direction

ν kinematic viscosity of fluid

φ_{xj} AR coefficients

ς eigenvector expansion coefficient used for NLPCA

ξ damping coefficient

Superscripts

$(\ddot{})$ double differentiation with respect to time

$(\dot{})$ differentiation with respect to time

$(^*)$ differentiation with respect to time

$\left(^d\right)$ damaged state

$\left(^h\right)$ healthy state

$(^-)$ mean value

$\left(^T\right)$ transverse matrix

Subscripts

0 amplitude

Other Symbols

A_y cross-flow amplitude

C_{Dinc} increased mean drag coefficient

C_{Dmean} mean drag coefficient

C_{it} cross-flow added mass coefficient

C_i added-mass coefficient

C_{Lmax} maximum lift coefficient

C_L lift coefficient

C'_L r.m.s. lift coefficient

C_m inertia coefficient

C_D fluctuating drag coefficient

E Young's modulus

EI flexural stiffness

e_x AR residual error

F_{drag} drag force

$F_{inertia}$ inertia force

F_{lift} fluctuating lift force

F_{Lo} lift force per unit length of structure oscillating case

F_{Ls} lift force per unit length of structure shear flow case

f_L dominant frequency of cross-flow motion

f_N natural frequency of cylinder

F_{oscl} total force oscillating cylinder

F_{osc} total force stationary cylinder under oscillatory flow

f_{osc} actual vibration frequency of cylinder

f_S vortex shedding frequency

f_V cross-flow vibration frequency of cylinder

F_p pressure force moving cylinder

$F_{Tx,y}$ external fluid force acting on a riser

KC Keulegan-Carpenter Number

KC^* upper limit third regime $KC(C_{Dmean}, C_m)$

KC_{md} upper limit second regime $KC(C_{Dmean}, C_m)$

KC_r upper limit first regime $KC(C_{Dmean}, C_m)$

k_{x1} stiffness parameter

L_e length of beam element

m^* mass ratio (mass of a body divided by the mass of the fluid displaced)

Re Reynolds number

S_t Strouhal number

T_t tension applied at the top end of riser

T_f period of the oscillatory flow motion

U_0 relative in-line maximum velocity

U_1 instantaneous velocity of the fluid in the in-line direction

U_r reduced velocity (path length per cycle over model width)

u_x instantaneous in-line displacement of oscillating body

u_y instantaneous cross-flow displacement of oscillating body

$u_{x,y}$ deflection of riser

$x(t)$ standardized signal used for the AR-ARX prediction model

Y_{rms} root mean square antinode amplitude

$y(t)$ centered observations used for NLPCA

Chapter 1

Introduction

1.1 Motivation

The increase in demand for oil has recently motivated the oil industry to actively invest in deepwater oil projects. One of the most critical components is the slender flexible pipe (riser) employed to transport oil from the seabed to the offshore facilities. However, at water depths of more than 2000 m, the use of composite materials shifts the response of a riser into a dangerous region in which there is a large interaction between the riser and its surrounding fluid due to the reduced weight of this type of riser. Several experimental and numerical studies have pointed out that the main difficulties related to the use of reduced weight for risers are associated to the increase of the cross-flow displacements, a wider regime of the lock-in region controlled by the reduced velocity, the inclusion of an additional branch of response and a rapid rise of the lift (transverse) coefficients in the lock-in region. In addition, the frequency, at which lock-in occurs, varies depending on the value of the mass-ratio (calculated as the mass of the cylinder divided by the mass of the fluid displaced). At low values of mass and damping, the classical definition of lock-in stated as the matching of the natural and response frequencies is not appropriate and therefore, as previous studies recommended, a more convenient definition of the frequency during lock-in events can be stated as the matching of the periodic wake vortex mode with the response frequency.

Existing riser models mainly rely on large databases of experimentally derived hydrodynamic force coefficients obtained under different modeling consid-

erations. As a result, the quality of a semi-empirical model strongly depends on the force coefficients provided by the aforementioned databases. The main limitation of this approach is associated with the high cost of the experimental facilities needed to obtain these force coefficients. On the other hand, turbulence remains poorly understood making Computational Fluid Dynamics (CFD)-based approaches restricted for industrial design. Most of the progress that has been recently achieved in numerical prediction of Vortex-Induced Vibration (VIV) is mainly restricted to low-Reynolds number regime. Current semi-empirical prediction programs used large databases of experimentally determined coefficients to predict VIV. Although these programs are widely used for practical applications, different models for the prediction of VIV can give different results among these programs. Several experiments have also been conducted recently to better understand the VIV response of risers. Some of these experiments were carried out to measure the hydrodynamic input coefficients for the aforementioned semi-empirical prediction programs to validate analytically derived models of risers. The main conclusion that can be drawn from these experiments is that VIV response is an inherently nonlinear, self-regulated, multi-dof phenomenon. Therefore, in order to meet the demands of developing deepwater oil fields, there is an ongoing research targeting the accurate prediction of deepwater risers.

On the other hand, current inspection techniques for riser systems are expensive and based on the practical experience of the engineers who carry out these inspections. The development of maintenance procedures must accompany the newly developed dynamic response prediction models for risers in order to reduce the overall cost of deepwater oil projects. An innovative approach to assess the current health state of civil engineering structures is the use of structural dynamic properties to detect damaged sites; the main idea behind this approach is that considerable changes in the modal properties such as natural frequencies, mode shapes and damping ratios provide quantitative information about the health condition of a structure. Nevertheless, in offshore structures due to variation of mass or marine growth the measured modal parameters show large variability. Therefore, the research community has been recently exploring the use of pattern recognition techniques to tackle the problem of reliable damage detection.

1.2 Objetives

The overall objective of the research reported here is to propose a response prediction model for oscillating flexible risers and a damage assessment methodology using acceleration records collected from sensors located along the riser. According to the above summary of all considerations in the process of the development of a prediction model and a damage assessment methodology for flexible risers, the specific objectives of the research reported in this thesis are as follows:

1. To numerically implement a newly developed prediction model for flexible risers.

2. To experimentally validate the proposed prediction model using long flexible riser models tested under different conditions.

3. To numerically implement vibration-based damage detection methodologies in flexible risers including the widely used modal-based approach.

4. To study the efficiency of the damage assessment methodology using the previously developed response prediction model for flexible risers.

1.3 Overview

In this thesis a response prediction model and a damage assessment methodology for flexible risers are proposed. Long flexible risers models are used to experimentally validate the proposed response prediction model. The damage assessment methodology uses acceleration records collected from the sensors using simulated data from the proposed response prediction model.

In the second chapter of this thesis the classification of riser systems is discussed based on the advantages and limitations of each system. The main concepts related to the behavior of a stationary cylinder in uniform and oscillatory flow are provided. The key factors that influence the response of bluff bodies are also discussed. Special emphasis is given to the effects of cylinder motion on wake. The chapter finishes with the description of fluid-structure interaction pointing out the current limitation in the understanding of this important phenomenon.

The third chapter discusses the development of the proposed response prediction model for flexible risers. A discussion of the challenges in modeling these types of structures is provided. Experimental models are then used to validate the proposed response prediction models considering a wide range of experimental validation. An additional hanging model is used for validation purposes.

Chapter four presents the implementation of three vibration-based damage detection methods using the previously developed prediction model. Here, different damage scenarios are studied. A modal-based damage detection approach is also considered. The chapter finishes with the numerical implementation of a statistical pattern recognition technique in a long flexible riser model.

A summary and conclusions of the presented work are given in chapter five. A section describing the pros and cons of the proposed methodology is provided in this chapter. Conclusions regarding the implementation of the damage assessment methodology to riser systems are also discussed. Finally, some possibilities for future research in the area of response prediction and damage assessment for flexible risers are provided.

Chapter 2

Flexible Risers

2.1 Riser Systems

A flexible riser is a structure whose natural bending frequencies are located in the range of expected vortex shedding frequencies when placed in a flow stream. Therefore, a flexible riser vibrates in flexure due to vortex shedding. This results in a very complex phenomenon commonly referred to as fluid-structure interaction [Pantazopoulos (1994)]. Chakrabarti (2002) reported that as part as the Norwegian deepwater project, the Reynolds number range for two-months records of the Helland-Hansen drilling riser was from about 0.9×10^5 to 6×10^5. There are basically two existing riser systems, namely the Steel Catenary Riser (SCR) and the Hybrid Riser Tower (HRT). The former system consists of individual hanging off risers and the second one consists of bundled risers arranged in a vertical tower. Saint-Marcoux (2004) compared these two systems in terms of their suitability for deep water field developments. According to Saint-Marcoux (2004), the HRT system is more suitable for ultra-deep water field developments beyond 2000 m. SCR systems are still widely used, mostly in the Gulf of Mexico and Campos Basin (Brazil) as well as newly field developments in Nigeria. However, construction and installation experience of HRTs to date has been good providing a very in-sensitive interface with both the seabed and the floating support unit [Sworn (2005)]. Based on the above-mentioned, in the following sections some characteristics of these two systems are provided.

2.1.1 Steel Catenary Riser SCR

A SCR system is based on the concept of a steel flowline that is connected from the seabed to the floating production facility using pipelay technology with offshore welding. Therefore, the main concept related to this system is a flexible pipe suspended from its support facility in a catenary shape and laying down to the seabed and therefore continuing into a horizontal flowline or simply connected to an existing horizontal flowline as shown in Fig. 2.1[1]. The main concern for this system is therefore the Touch-Down Point (TDP), where the interaction between the seabed and the SCR creates a very fatigue sensitive region. Therefore, SCR is a fatigue dominated structure [Saint-Marcoux (2004)].

There are several nonlinearities involved in the global analysis of SCR systems. Hydrodynamic forces and contact forces between the seabed and the SCR account for most of those nonlinearities leading to the use of dynamic simulation in time domain to predict its dynamic response [Campos & Martins (2001)]. A flex or taper joint is commonly used as the connection mechanism between the SCR and the floating production facility, this mechanism absorbs the dynamic moment variations generated by the motions of the floating production facility. On the other hand, at the TDP, an anchor system is sometimes used in order to stabilize the SCR axially and eliminate undesired motions [Saint-Marcoux (2004)].

2.1.2 Hybrid Riser Tower HRT

A HRT system is defined as a free-standing vertical riser composed of steel lines and flexible composite lines within the same configuration. A near surface cylindrical buoyancy tank is commonly employed in order to apply a tension force to the HRT. The connection of the HRT at the seabed is achieved by using an anchor base in which the riser is connected to a mechanical device that acts as a flex or taper joint. A HRT system is depicted in Fig. 2.2[2].

The global analysis of a HRT system is dominated by buoyancy forces rather than gravity forces and it is usually compared to an upside down pendulum. Therefore, buoyancy forces dominate the dynamic response of a HRT system

[1] 2H Offshore©
[2] Acergy©

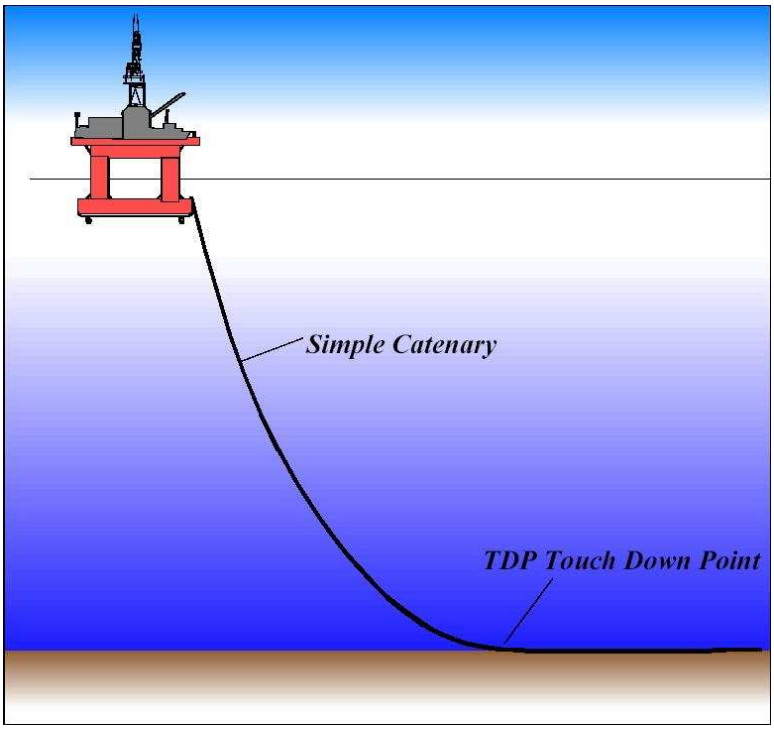

Figure 2.1: Steel Catenary Riser

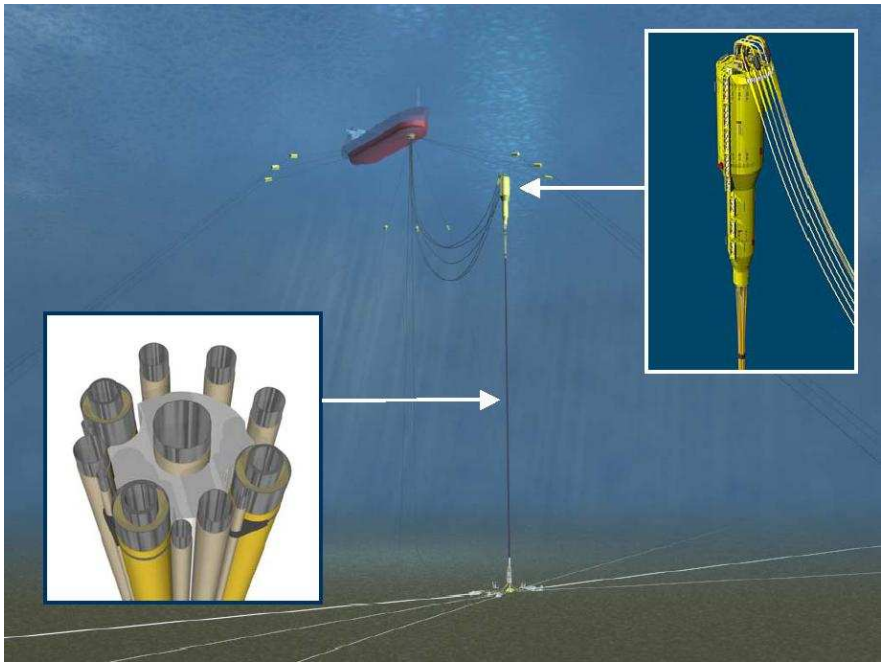

Figure 2.2: Hybrid Riser Tower

leading to instability of the HRT system when loss of a critical level of buoyancy is produced [Sworn (2005)]. Blevins *et al.* (2006), highlighted some advantages of the HRT system when compared with the SCR system. Basically, large diameter risers can be accommodated, field layout is simplified allowing future expansion, demanding flow assurance requirements can be met, riser loads on the floating production facility are reduced and in place riser fatigue is low.

2.1.3 Riser System Selection

Based on the fact that the number of components of the SCR system are less than the HRT system, at first glance seems easier to manage compared to the HRT. However, SCRs are fatigue-prone structures. Most of the fatigue damage in the SCR system is concentrated in the connection region with the floating production unit as well as the TDP. On the other hand, the HRT system is subject to little fatigue damage when in operation.

The seabed interface requires special consideration in both SCR and HRT systems. In the HRT systems more components are needed. However, the interface between the HRT system and seabed is considered to be an engineering issue and it is therefore related to the technology employed in the construction of the interface. On the other hand, the interface between the SCR system and seabed is associated to technical issues and lack of sufficient understanding of the TDP mechanism leading to the use of anchors to secure the long term stability of the SCR system [Saint-Marcoux (2004)].

The interface with the floating support unit represents one of the major advantages of the HRT system due to the lower loads transmitted to the floating support system. Therefore, the top tension transferred to the floating support unit can be reduced by several thousand tons. On the other hand, the SCR system is sensitive to dynamic motion of the floating support unit leading to a design issue related to hang-off balcony that must remain as close as possible to the centre of gravity of the floating structure [Saint-Marcoux (2004)].

Inspection, maintenance and repair play a vital role in the selection of the riser system. As previously mentioned, the SCR system is a fatigue-prone structure. However, the HRT system has more components potentially subject to failure.

In this respect, both systems are affected by several uncertainties and therefore maintenance-based riser system selection is case dependent. However, the inspection activities for the HRT system can be carried out more efficiently than the SCR system due to its free-standing vertical configuration.

Finally, the HRT system tends to be a more expensive solution in water depths of at least 1000 m. On the other hand, the use of the SCR system in field developments beyond 2000 m causes the overall cost to significantly increase due to large top tensions and therefore the need of expensive installation vessels.

2.1.4 Composite Risers

Deep water drilling currently reaches water depths down to more than 2000 m. However, riser weight and riser control are still considered as critical conditions. Therefore, composite materials, especially glass-epoxy and carbon-epoxy composites, have been investigated as an alternative to save weight in riser systems [Ohtsubo & Sumi (2000)]. High strength and stiffness commonly associated to composite materials as well as low specific weight, high corrosion resistance and fatigue characteristics make them potentially valuable for use in riser systems. In the past, the needs of aeronautical engineers led to the development of composite materials as structural materials as well as mass production of composites. A metal-composite riser is considered to be suitable for riser systems due to leakproofness provided by its inner layer. The main objective of the inner layer is to resist corrosion and abrasion. By using composite materials, the riser weight and the expenses for tensioners can become much lower [Beyle *et al.* (1997)].

The fluid force on a composite riser is the same as the homogeneous riser when the risers are stationary. Forcing response is related to the geometry of the riser. Therefore, even if the cross section of the riser is made of steel or a composite material it renders the same fluid force when no vibration exits. When the riser vibrates, the fluid force is influenced by the riser motion. As a result, Vortex-Induced Vibration (VIV) will modify the fluid force for risers of two different materials. Finally, a composite riser has a different structural damping behavior [Rakshit *et al.* (2008)].

One of the main concerns related to the use of composite risers for ultra-deep water field developments is that the reduced weight of a composite riser shifts the dynamic response of the riser into a range where fluid-structure interaction problems increase. The main difficulties related to the use of reduced weight for risers are associated to the increase of the cross-flow displacements, a wider regime of synchronization between the frequency of the riser and vortex shedding frequencies, a more complex dynamic response and a rapid rise of the cross-flow force during synchronization events.

2.1.5 Internal Flow

With increasing operating depths, the thermal behavior of the fluid transported in a riser must be increasingly taken into account. According to Williams *et al.* (2005), ultra-deep water field developments are typically from shallow reservoirs with oil well temperatures in the region of 60 °C - 100 °C. Low temperatures imply greater difficulties with heat conservation making ultra-deep water field developments sensitive to the problems of wax and hydrate formation. In addition, petroleum reservoirs located in deep waters tend to be low-energy having relatively low pressures compared to conventional reservoirs. Therefore, the lower pressures available invariably mean that pressure maintenance is required through injection of one sort of another and an artificial lift may be needed such as gaslift injection, electrosubmersible or hydraulic submersible pumps or subsea multiphase booster pumps [Pickering *et al.* (2001)].

Even though several studies target the development of response prediction for risers, the modeling of a riser with the inclusion of internal flow inside the pipe has rarely been considered. The traveling fluid inside a deflected riser experiences coriolis accelerations due to the curvature of the riser itself and the relative motion of the fluid with respect to the time-dependent riser motion. Therefore, the dynamic response of the riser is affected causing additional vibrations. Guo & Lou (2008) developed an experimental set-up for a riser model considering internal fluid flow and external current. Basically, it was found that in still water the internal fluid flow reduced the natural frequency of the riser model. On the other hand, when the riser model was placed in current, the amplitude of the strain in

in-line and cross-flow vibrations increased. Finally, the effect of internal flow is more dominant with higher relative internal flow speed.

2.2 Vortex-Induced Vibration VIV

Consider a cylinder held in a fixed position without any external forces other than the fluid flow passing it. In this case, if a fluid particle that is moving in the direction of the fluid velocity is traced, then, the resulting line is called a streamline. As a result, it is obtained a family of curves that are instantaneously tangent to the velocity vector of the flow and if the computed streamlines do not vary with time the flow is defined as *steady*. However, if those streamlines vary with time the flow is defined as *unsteady*. Ideal fluids are based on the potential theory that considers the fluid to be incompressible and inviscid. Fig. 2.3 shows experimentally obtained streamlines[1].

However, a real fluid such as water is viscous and therefore internal friction exists, which causes the particle in contact with the cylinder to remain at rest. Therefore, a boundary layer is created due to the rapid change in velocity that exists between the particles at rest attached to the cylinder and the nearby particles moving at the mean stream velocity. This variation of velocity is produced in a very short distance. For laminar flow problems, this boundary layer is very narrow and therefore can be approximately neglected.

Gradual increment of the mean stream velocity causes the flow to separate from the cylinder. The two boundary layers, located in each side of the stagnation point (point located in the upstream face of the cylinder where mean stream velocity is zero), remain attached to the cylinder. However, as the mean stream velocity increases, these boundary layers separate from the cylinder at the downstream face causing the flow to curls up since two shear layers are created after separation of the particles of the boundary layers. The region located between these two shear layers experiences reduced flow activity, dominated by low pressure and therefore is defined as *wake*, which is a low-pressure region compared to the pressure on the upstream side.

[1] Armfield Engineering Education©

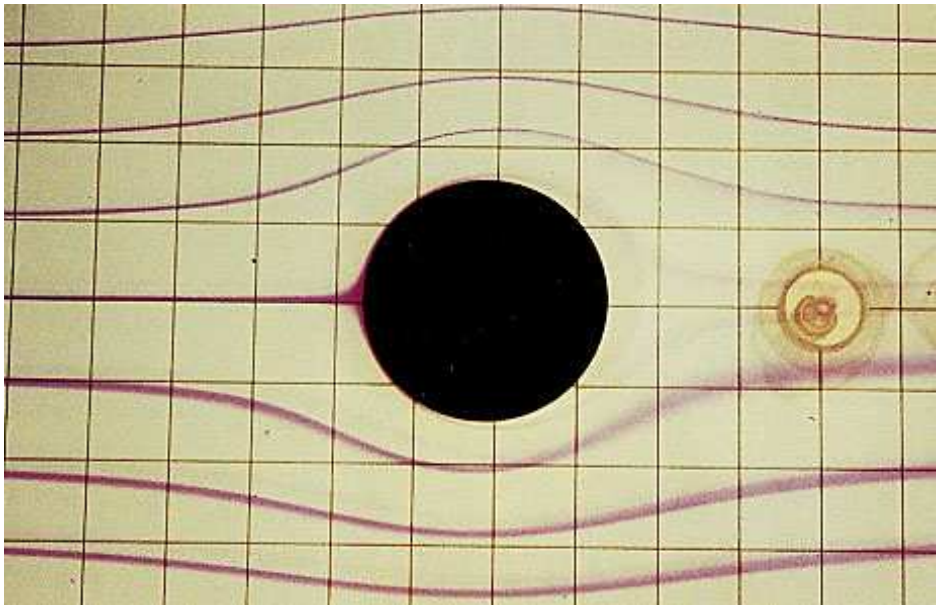

Figure 2.3: Potential Flow Over a Cylinder (A.E.E.)

In the *wake* the flow becomes turbulent in contrast to other regions away from the cylinder where the flow remains laminar. The upward roll of the shear layer introduces discrete swirling vortices, which form alternately on either side aft of the cylinder and the separation of these vortices from the cylinder, referred as *shedding*, is associated with frequencies with which the vortices are shed. These frequencies are widely known as *vortex shedding frequencies*. Finally, an asymmetric pressure distribution is created due to a regular pattern of vortices originated behind (downstream) the cylinder. The resulting effect is the introduction of a drag force and a fluctuating lift force [Chakrabarti (2002)].

2.2.1 Drag Force

As previously mentioned, the *wake* is associated to a low pressure region. The difference in pressure between the *wake* and the upstream region originates a drag force. The force experienced by the cylinder is found to vary with the square of the mean flow velocity, U, as shown in Eq. (2.1)

$$F_{drag} = \frac{1}{2}\rho C_{Dmean} S U^2 \tag{2.1}$$

where S is the frontal area of the body measured orthogonal to streamwise and ρ is the fluid density. Although C_{Dmean} is a constant parameter which mainly depends on Re, other parameters such as the shape of the body and roughness of the surface are also important. For the case of a circular cylinder across the flow Re can be expressed as:

$$Re = \frac{UD}{\nu} \tag{2.2}$$

where D is the cylinder's diameter and ν is the kinematic viscosity of the fluid. According to Henderson (1995), when Re is less than 50 the flow is *steady* and symmetric about the centerline of the *wake*. At $Re \approx 50$ this configuration becomes unstable leading to the initiation of the vortex shedding, which results in the widely know *Kármán* vortex street. Basically, the contributions to the value of the drag coefficient can be divided into viscous drag coefficient and pressure drag coefficient. Henderson (1995) highlighted the fact that experimental values of drag coefficients are difficult to obtain, especially at $Re \leq 1000$, and the available data show considerable scatter. Henderson (1995) presented computed values of C_{Dmean} obtained from high-resolution computer simulations, which correspond to the challenging region of $Re < 1000$ as shown in Fig. 2.4.

Blevins (1990) stated that the Re number range $300 < Re < 1.5 \times 10^5$ is called *subcritical* and it is mainly characterized by strong periodic vortex shedding. In the *transitional* range, $1.5 \times 10^5 < Re < 3.5 \times 10^6$, the cylinder boundary layers become turbulent leading to a drag coefficient drop to 0.3. In the *supercritical* range, $Re > 3.5 \times 10^6$, regular vortex shedding is re-established with a turbulent cylinder boundary layer. The above-mentioned process was graphically described by Lienhard (1966) as shown in Fig. 2.5.

2.2.2 Lift Force

As previously mentioned, the *wake* formed behind the cylinder and its associated vortex shedding cause an asymmetric pressure distribution. In addition, it has been experimentally found that the shedding of vortices alternates on the two sides and does not take place at the same time. Therefore, an additional force is

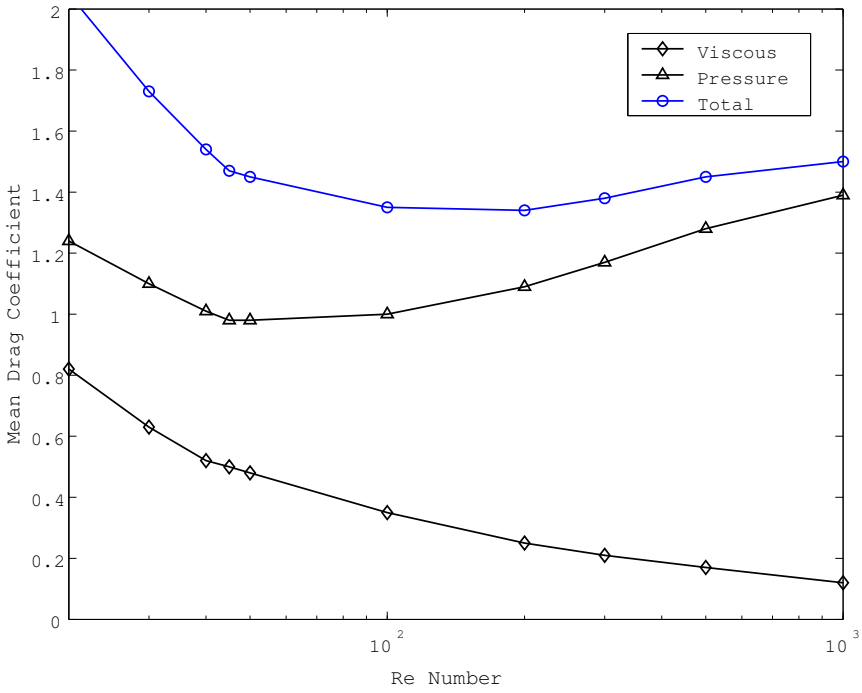

Figure 2.4: Pressure and Viscous Drag Coefficients Versus Re Number

generated transverse to the flow, which is widely known as fluctuating lift force and is written in a form similar to the inline drag force as:

$$F_{lift} = \frac{1}{2}\rho C_L S U^2 \tag{2.3}$$

According to Chakrabarti (2002), the formation of vortices and the associated *wake* field are irregular with respect to time. According to Norberg (2003), despite the vast amount of experiments there has not been real consensus on $C_L(Re)$, especially for $Re < 6 \times 10^3$. The range from about $Re = 190$ (the approximate onset of intrinsic three-dimensional flow) to $Re \approx 6 \times 10^3$ has been greatly overlooked on the past. Therefore, this fact reflects several difficulties recently encountered in experimental and numerical studies. Therefore, F_{lift} is irregular and C_L is not well defined. The Strouhal number (S_t) is the dimensionless proportionality constant between the predominant frequency of the vortex shedding and the mean uniform flow velocity divided by the cylinder width as shown in Eq. (2.4)

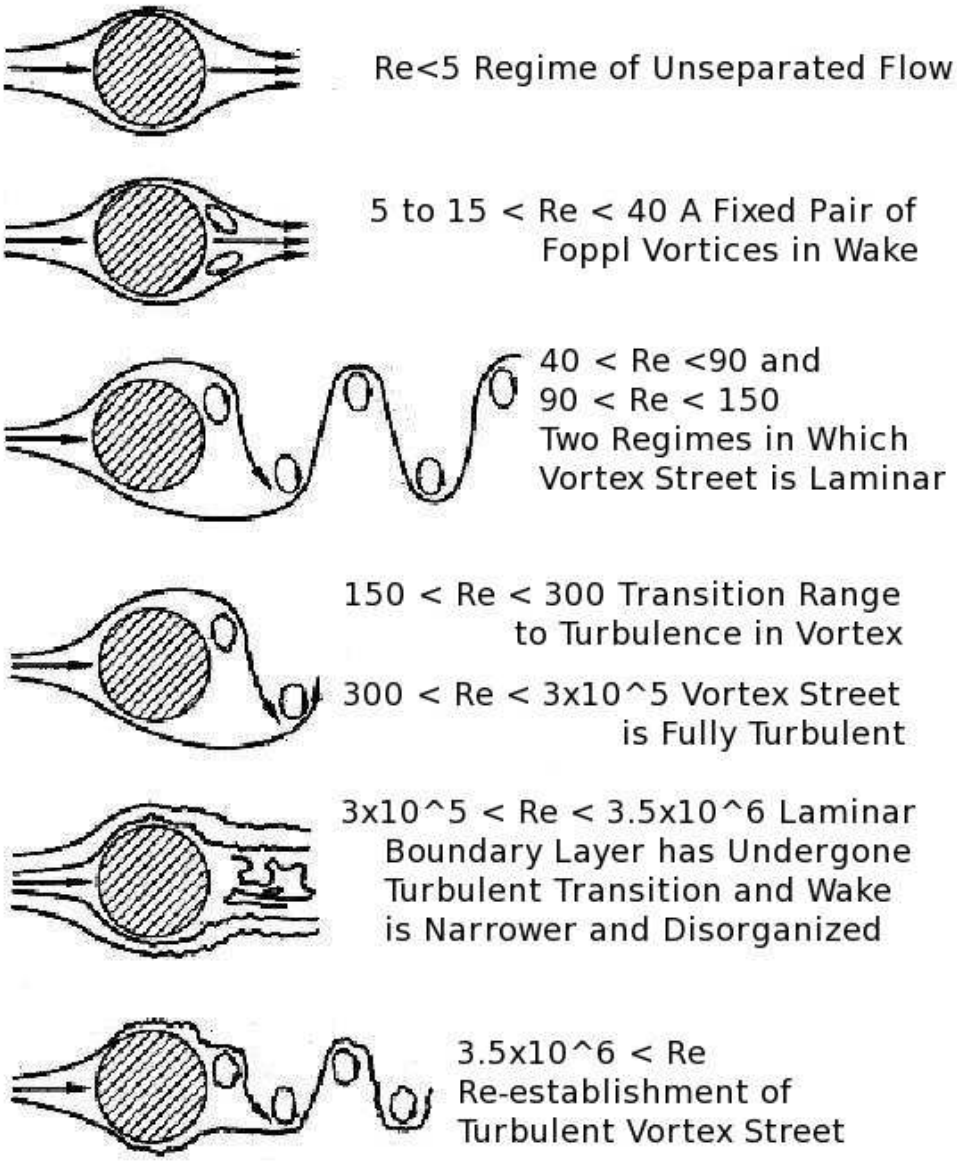

Figure 2.5: Regimes of Fluid Flow Across Smooth Circular Cylinders [Lienhard (1966)]

$$f_S = \frac{S_t U}{D} \tag{2.4}$$

Norberg (2003) presented a compilation of $S_t(Re)$ from selected experiments and 2-dimensional numerical simulations and developed an empirical formulation for $S_t(Re)$, which is shown in Fig. 2.6.

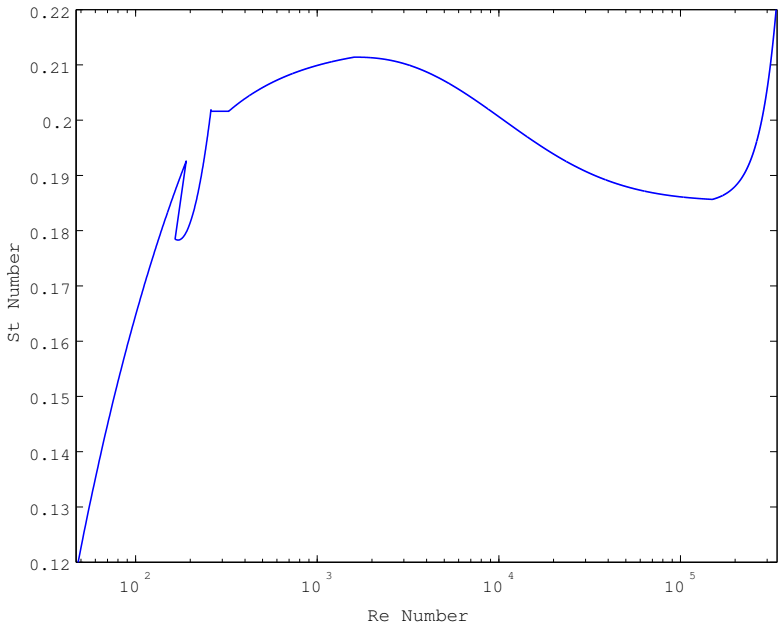

Figure 2.6: S_t Number Versus Re Number

According to Norberg (2003), a vast amount of quantitative data have been reported and numerous compilation graphs on the variation of $C_L(Re)$ have been presented. Norberg (2003) based on several experimental and numerical studies, employed the r.m.s. (root-mean-square) lift coefficient, C_L', to present a formulation of C_L' versus Re as shown in Fig. 2.7.

2.3 Oscillatory Flow Past a Stationary Cylinder

According to Chakrabarti (2002), it can be demonstrated that the case of an oscillating structure in calm fluid is equivalent and kinematically identical to oscillating fluid flowing past a stationary structure. Taking the length of the

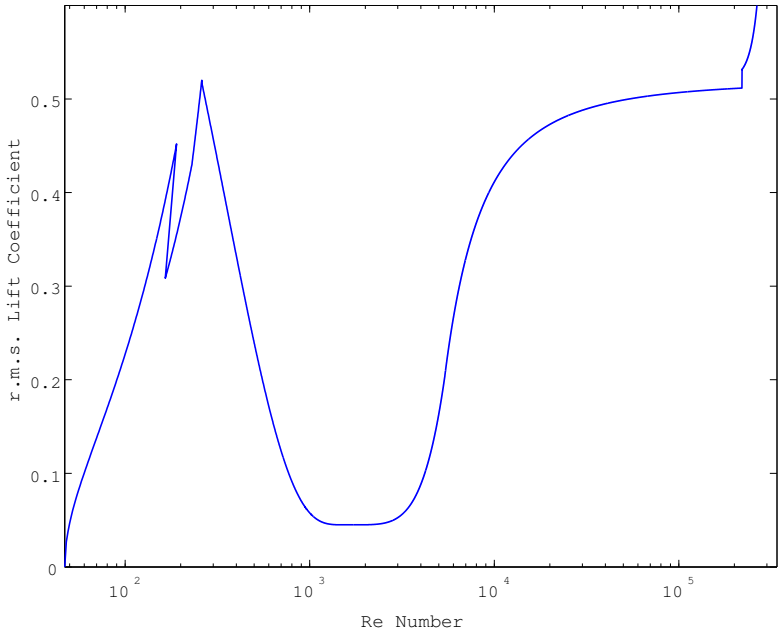

Figure 2.7: C_L' Versus Re Number

cylinder as unity, the inline force experienced by a cylinder in oscillatory flow is similar to Eq. (2.1) as shown in Eq. (2.5), but using the absolute sign to take into account the changing direction of the force and the instantaneous velocity, U_1.

$$F_{drag} = \frac{1}{2}\rho C_{Dmean} D \left|U_1\right| U_1 \tag{2.5}$$

For a stationary cylinder excited by oscillatory flow the inertia force can be written using the inertia coefficient, C_m, as shown in Eq. (2.6)

$$F_{inertia} = \rho C_m \frac{\pi}{4} D^2 \dot{U}_1 \tag{2.6}$$

Combining the two force components related to C_m and the mean drag coefficient, C_{Dmean}, the total force per unit length experienced by a stationary cylinder under oscillatory flow, F_{osc}, is obtained and corresponds to the widely known Morison's equation [Morison *et al.* (1950)], which is described by the following equation:

$$F_{osc} = \rho C_m \frac{\pi}{4} D^2 \dot{U}_1 + \frac{1}{2} \rho C_{Dmean} D \left| U_1 \right| U_1 \tag{2.7}$$

It has been proved that C_m and C_{Dmean} are functions of Re and Keulegan-Carpenter (KC) numbers. In the case of oscillatory flow past a stationary cylinder Re and KC are expressed in terms of the amplitude of the oscillatory motion, U_0, and the period of the oscillatory motion, T_f, as shown in the following equations:

$$Re = \frac{U_0 D}{\nu}; \quad KC = \frac{U_0 T_f}{D} \tag{2.8}$$

Sarpkaya (1977a) introduced a viscous-frequency parameter β, which is shown in the following equation:

$$\beta = \frac{D^2}{\nu T_f} = \frac{D^2 f}{\nu} = \frac{Re}{KC} \tag{2.9}$$

2.3.1 Determination of C_m and C_{Dmean}

C_m and C_{Dmean} are either obtained from experiment or from numerical solution of the Navier-Stokes equations. However, at sufficiently low KC, which is characterized by laminar and two-dimensional causing the flow to remain attached to the cylinder, Wu (1981) derived the following analytical forms for C_m and C_{Dmean} (Valid for $KC << 1$, $Re \times KC << 1$ and $\beta >> 1$):

$$C_m = 2 + 4 \left(\pi\beta\right)^{-\frac{1}{2}} + \left(\pi\beta\right)^{-\frac{3}{2}} \tag{2.10}$$

$$C_{Dmean} = \frac{3\pi^3}{2KC} \left[\left(\pi\beta\right)^{-\frac{1}{2}} + \left(\pi\beta\right)^{-1} - \frac{1}{4} \left(\pi\beta\right)^{-\frac{3}{2}} \right] \tag{2.11}$$

Basically, the Morison's equation (2.7) is commonly used to obtain C_m and C_{Dmean} through standard Fourier averaging process applied to computed time histories of the in-line force. The variation of C_m and C_{Dmean} from cycle to cycle at low values of KC number is small but at larger KC, where there is shedding of strong vortices, the variations can become large [Lin *et al.* (1996)].

According to Zhou & Graham (2000), the magnitude of KC indicates the relative importance of drag and inertia forces. When $KC \leq 5$, *inertia regime*,

the cylinder is mainly subject to inertia force. However, Zhou & Graham (2000) pointed out that due to the existing relationship between drag force and hydrodynamic damping, for certain types of problems the contribution of drag force is relevant. When $5 \leq KC \leq 25$, *inertia/drag regime*, the drag and inertia force are both important. Finally, beyond $KC \geq 25$, *drag regime*, the drag force becomes dominant, but changes in the inertia force may sometimes be significant in affecting natural frequencies of the cylinder.

Zhou & Graham (2000) also classified the flow around a circular cylinder into four regimes according to the variation of C_m and C_{Dmean} with respect to KC. In the first regime, $KC < KC_r$, as KC increases C_{Dmean} decreases while C_m is independent of KC, this regime is defined as *inertia regime*. In the second regime, $KC_r < KC < KC_{md}$, C_{Dmean} decreases reaching its minimum value at KC_{md} where the flow has just separated and turbulence occurs successively, C_m keeps nearly constant. In the third regime, $KC_{md} < KC < KC^*$, C_{Dmean} increases and C_m decreases as KC increases and reach maximum and minimum values, respectively, at KC^*. Finally, in the fourth regime, C_{Dmean} decreases and C_m increases as KC increases further.

2.3.2 Patterns of the Vortex Shedding

The magnitude of KC also indicates different flow modes. Several authors have described the flow regimes observed in oscillatory flow past a stationary cylinder. Among many others descriptions, the ones provided by Bearman *et al.* (1981) and Williamson (1985) are cited most frequently. According to Lin *et al.* (1996), at low values of KC, $1 < KC < 2$, depending on β, the flow is symmetrical and remains attached to the cylinder. At $KC \approx 4$, the flow separates but remains symmetrical as concentrations of vorticity are swept back over the cylinder when the flow reverses. Then, the asymmetric shedding of a pair of opposite sign vortices is observed in each half cycle for $4 < KC < 7$. Obasaju *et al.* (1988) stated that above KC=7 a new regime is achieved as KC is increased in increments of about 8 leading to one more full vortex to be shed per half cycle of flow oscillation. At $7 < KC < 15$ most of the vortex shedding activity is concentrated on one side of the cylinder. At $15 < KC < 24$ the flow enters the diagonal shedding mode

consisting of a pair of oppositely signed vortices that convects away at about 45° to the main flow in one half cycle and another pair of vortices that convects in a diametrically opposite direction in the next half cycle. At $24 < KC < 32$ three full vortices are shed during each half cycle and three vortex pairs convect away from the cylinder for a complete cycle. This trend is maintained as KC increases with more and more vortex pairs being formed and shed per flow cycle. Blevins (1990) provided an approximate formulation to predict the value of the vortex shedding frequency, f_S, based on KC as shown in the following relationship:

$$\frac{f_S}{f} = 2, 3, 4, 5, ... = \ an\ integer\ \approx 0.2KC\ (assuming\ S_t = 0.2) \tag{2.12}$$

Based on the previous relationship (2.12), Blevins (1990) presented the following classification for $f_s(KC)$

Table 2.1: Patterns of Vortex Shedding

KC Number	Regime	$\frac{f_S}{f}$
$4 < KC < 8$	Asymmetric	2
$8 < KC < 15$	Transverse	2
$15 < KC < 22$	Diagonal	3
$22 < KC < 30$	Third Vortex	4
$KC > 30$	Quasi-steady	$\approx 0.2KC$(2.12)

2.4 Fluid-Structure Interaction

The cases of an stationary circular cylinder excited by shear and oscillatory flows were presented in previous sections. Hydrodynamic forces on a oscillating cylinder are much more complex than the resulting hydrodynamic forces from a stationary cylinder. In-line hydrodynamic forces can be represented by including in the Morison's equation (2.7) the contribution of the structure to the total force as shown in Eq. (2.13).

$$F_{oscl} = -m\ddot{u}_x + \rho C_m \frac{\pi}{4} D^2 \dot{U}_1 - \rho C_i \frac{\pi}{4} D^2 \ddot{u}_x + \frac{1}{2}\rho C_{Dmean} D \left|U_1 - \dot{u}_x\right| (U_1 - \dot{u}_x) \tag{2.13}$$

where u_x is the instantaneous in-line displacement of the oscillating body. Three force parameters are included in Eq. (2.13), the mean drag coefficient C_{Dmean} , the inertia coefficient C_m and the added-mass coefficient C_i, with

$$C_m = C_i + 1.0 \tag{2.14}$$

According to Dutsch *et al.* (1998), the added value of 1.0 in Eq. (2.14) is the result of the uniform pressure gradient occurring in a globally accelerated flow. Hydrodynamic force on an oscillating cylinder includes added mass and damping forces in addition to lift. Furthermore, in the case of an oscillating cylinder the lift force may be substantially different from that measured on an equivalent stationary cylinder [Pantazopoulos (1994)]. Sarpkaya (1995) made a clear distinction between vortex-shedding excitation and *attenuating damping*. The latter is associated to an oscillating body in a fluid otherwise at rest and implies a decrease of the amplitude of the externally imparted oscillation by forces in anti-phase with velocity. It is clear that the unseparated flow about the oscillating body does not give rise to oscillatory forces in any direction and, thus, it cannot excite the body. Sarpkaya (1995) highlighted that *hydrodynamic damping* is still used to lump into one parameter the existing inability to predict the dynamic response of fluid-structure interactions. Pantazopoulos (1994) pointed out that added mass and *hydrodynamic damping* are important in water but insignificant in air. Added mass in air is very small in comparison with the mass of the cylinder for typical engineering structures and therefore contributes little to the overall response of the system. Lift forces at resonance are equilibrated by *hydrodynamic damping*, this signifies that damping force generated on a cylinder in water is of the same magnitude as lift force. On the other hand, damping force generated in air is related to the damping provided by the supports or material, aerodynamic damping is generally very small [Pantazopoulos (1994)]. Hartlen & Currie (1970) and Sarpkaya (1977b) assumed a harmonic function for the hydrodynamic force and decomposed it into one in phase with cylinder

velocity and a second one out of phase (180°) with cylinder acceleration. The former related to *hydrodynamic damping* adds or subtracts energy to the vibrating cylinder, while the latter related to *added mass* performs no net work over one cycle.

As reported by Dowell & Hall (2001), in order to model fluid-structure interaction it is neccesary to model both the structure and the fluid. On one hand, in the analysis of complex structures the Finite Element Method (FEM) has been widely and successfully used. On the other hand, when using a Computational Fluid Dynamics (CFD) approach it is possible to consider not only the potential-flow models of irrotational flow, but also the inviscid rotational models of the Euler equations and indeed the viscous models of the Navier-Stokes equations. However, the computational resources needed to solve the Navier-Stokes equations are even today beyond existing capabilities. Therefore, several empirical models of turbulence have been developed in order to make the Navier-Stokes equations computationally tractable. Despite of these efforts, the use of CFD remains computationally prohibited for the solution of fluid-structure interaction problems encountered in most engineering applications.

2.4.1 Effect of Cylinder Motion on Wake

Effects on lift force resulting from the cylinder motion on the *wake* include changes in the lift force magnitude, frequency and correlation length. Cross-flow vibration with frequency at or near f_S organizes the *wake*. Vibration increases the correlation of the vortex shedding along the cylinder axis. The correlation is a measure of the three-dimensionality of the flow in the cylinder *wake*. Therefore, a correlation of 1.0 implies two-dimensional flow [Blevins (1990)]. When the cylinder oscillation frequency deviates from f_S, correlation length drops off quickly toward the values of stationary cylinders [Pantazopoulos (1994)].

Cylinder vibration with frequencies near f_S influences the pattern and phasing of the vortices. As the cylinder vibration passes through f_S, there is an remarkably clear and rather abrupt 180° phase shift. Zdravkovich (1982) found before the phase shift, shedding of vortices takes place at maximum cylinder amplitude from the cylinder edge (farthest from the *wake* centerline). After the phase shift,

shedding of vortices takes place at maximum cylinder amplitude from the *inside* cylinder edge. An increment in transverse amplitude to values of approximately $1.5D$ leads to break up of the symmetric pattern of alternate vortices. As a result, it is observed that an amplitude of $1.0D$, three vortices are formed per cycle of vibration instead of the stable pattern of two per cycle at lower amplitudes. Therefore, this break up implies that the vortex sheeding forces applied to the cylinder are a function of cylinder amplitude and may be self-limiting at large vibration amplitudes [Blevins (1990)].

2.4.2 Synchronization or Lock-in

According to Gabbai & Benaroya (2005), at low flow speeds, f_S is the same as that obtained from a stationary cylinder following the Strouhal relationship. As the flow speed is increased, f_S approaches the vibration frequency of the cylinder f_V. In this regime of flow speeds, f_S no longer follows the Strouhal relationship. Instead, f_S becomes *locked-in* or *synchronized* to f_V ($f_V \approx f_S$). If f_S is close to the natural frequency of the cylinder f_N, large body motions are observed and the cylinder undergoes near-resonance vibration. Therefore, the motion of the cylinder organizes the *wake* and causes f_S to suddenly change from its nominal value to f_N.

Synchronization or lock-in is frequency-dependent, and will occur for certain periodic motions of the cylinder at or near f_S indicated for a stationary cylinder. Therefore, a dimensionless parameter called *reduced velocity* U_r, is defined as the path length per cycle over the model width (cylinder=D) as shown in Eq. (2.15).

$$U_r = \frac{U_1}{f_{osc} D} \tag{2.15}$$

The *reduced velocity* is widely used to define the *lock-in region*. f_{osc} is defined as the actual vibration frequency. Therefore, as f_S approaches to f_N the following relationship can be obtained:

$$f_N \approx f_S = \frac{S_t U_1}{D} \quad or \quad \frac{U_1}{f_N D} \approx \frac{U_1}{f_S D} = \frac{1}{S_t} \approx 5 \tag{2.16}$$

Blevins (1990) stated that the fundamental cross-flow vibrations ordinarily occur over the reduced velocity range $4 < U_r < 8$ leading to *locked-in* resonant oscillations characterized by large-amplitude vibrations. Then, *lock-in region* can be approximately defined as contained in the aforementioned limits. According to Pantazopoulos (1994), in the *lock-in region*, lift, added mass, and damping forces cannot be distinguished, and only amplitude and phase of the total hydrodynamic force can be determined. At frequencies far above the *lock-in region*, added mass is equal to its nominal value of unity. At frequencies above the *lock-in region*, added mass increases near 2.0, which is similar to the case of a oscillatory flow past a stationary cylinder taking its length as unity. At frequencies below the *lock-in region*, the cross-flow added mass coefficient, C_{it}, becomes negative. This variation tends to change the natural frequency of the cylinder toward the *lock-in region*. As a result, C_{it} is generally frequency-dependent, but relatively insensitive to amplitude and there is a tendency for the negative added mass values to increase as the cross-flow amplitude A_y increases [Pantazopoulos (1994)].

The damping coefficient is strongly dependent on A_y and somewhat less sensitive to frequency outside the *lock-in region*. This dependence is much stronger at frequencies above the *lock-in region* than frequencies below the *lock-in region*. At frequencies above and below the *lock-in region*, the damping coefficient is consistent with typical drag coefficient data. Within the *lock-in region*, it is not possible to separate damping from lift as previously mentioned and therefore the resulting force term proportional to cylinder velocity is frequency and amplitude dependent [Pantazopoulos (1994)].

2.4.3 Increased Mean Drag Coefficient

Blevins (1990) showed that the average (steady) drag on a cylinder vibrating at or near f_S is a strong function of A_y. Substantial increases in drag can occur for a cylinder vibrating in resonance with vortex shedding. C_{Dmean} is known to increase two or three times (even four times in some experiments) over the value for stationary cylinder as a result of lock-in [Kim & Perkins (2003)]. Mean drag amplification was first discovered by Bishop & Hassan (1964). Since then empirical formulas for increased drag, valid for the *lock-in region*, have been

proposed by several investigators [Vandivier (1983), Skop *et al.* (1977), Sarpkaya (1978)]. Most of these expressions give similar values (within 15%).

Vandivier (1983) proposed an empirical relation for the prediction of drag coefficients under lock-in conditions at Re numbers up to 22000. Vandivier (1983) used data from field experiments and concluded that drag coefficients in excess of 3.0 are possible under lock-in conditions. The empirical relation for increased mean drag coefficient, C_{Dinc}, proposed by Vandivier (1983) using the root mean square antinode amplitude, Y_{rms}, is shown in Eq. (2.17).

$$\frac{C_{Dinc}}{C_{Dmean}} = 1 + 1.043 \left(\frac{2Y_{rms}}{D} \right)^{0.65} \tag{2.17}$$

Chaplin *et al.* (2005b) more recently showed the validity of Eq. (2.17) using experimental data obtained from a riser model in stepped flow. The experimental model was pinned at its bottom end and had a length of 13.12 m, a diameter of 0.028 m and a mass ratio of 3 (calculated as the mass of the riser divided by the mass of the fluid displaced). The stepped current effect was achieved by mounting the riser model on a towing carriage with the upper 55% of the model in still water condition while the lower 45% was exposed to current.

Kim & Perkins (2003) presented a methodology to compute C_{Dinc}, based on the empirical formula derived by Skop *et al.* (1977) that was developed in order to consider lock-in events using the peak-to-peak amplitude, 2Υ, in the cross-flow direction as shown in the following equations:

$$\frac{C_{Dinc}}{C_{Dmean}} = 1 \;\; if \;\; w_r < 1 \;\; otherwise \;\; 1 + 1.16 \left(w_r - 1 \right)^{0.65} \tag{2.18}$$

$$w_r = \left(1 + \frac{2\Upsilon}{D} \right) \left(U_r S_t \right)^{-1.0} \tag{2.19}$$

Khalak & Williamson (1999) conducted an experimental work involving the transverse oscillations of a mounted rigid cylinder. Measurements of drag and lift showed large amplification of maximum mean and fluctuating forces on the cylinder. Khalak & Williamson (1999) compared the experimental values of C_{Dinc} with the values computed from the empirical formula developed by Sarpkaya

(1978). Good agreement was found in these comparisons. The empirical formula developed by Sarpkaya (1978) is shown in Eq. (2.20).

$$\frac{C_{Dinc}}{C_{Dmean}} = 1 + 2\left(\frac{A_y}{D}\right) \tag{2.20}$$

2.4.4 Concluding Remarks

There is still a limitation in the appropriate understanding of the main parameters related to fluid-structure interaction. In this chapter, the fundamental theory related to the cases of a stationary cylinder under uniform flow and oscillatory flow as well as an oscillating body in calm water was presented. The concepts presented in this chapter will be used in the following chapter to develop a response prediction model for oscillating flexible risers.

Chapter 3

Response Prediction of Flexible Risers

A great deal of attention has been given in recent years to meet the industry demands of providing riser systems for profitable oil extraction at water depths of 1000 m or more. In addition, there is an ongoing interest in the use of riser systems for carbon dioxide injection in deep sea. As a result, the research community is actively working on developing response prediction models for risers in order to comply with the aforementioned demands. However, the self-regulated nature of the Vortex-Induced Vibration (VIV) process, caused by vortices shed from a riser, is highly nonlinear and therefore its accurate prediction is still not possible.

Numerical methods have been extensively used to solve the coupled problem of VIV of risers. There are basically three methods, namely 1)the direct numerical simulation, 2)the vortex method and 3)the Finite Element Method (FEM) [Gabbai & Benaroya (2005)]. Numerical-based approaches have many limitations considering the large number of variables that must be included in the analysis; in addition, modal response in sheared current, in which the velocity varies along the riser's axis, is still not well understood. The fluid motion and the motion of the riser must be coupled in order to obtain a good prediction model; especially in the lock-in region, where the vortex shedding frequency matches or collapses onto the natural frequency. It is still challenging to numerically predict the dynamic behavior of this coupled system. Most of the numerical simulations are restricted to the lower end of the Re number spectrum.

There are basically two approaches for predicting the dynamic response of a flexible riser. The main difference between these two approaches is related to the procedure employed to calculate hydrodynamic forces. A CFD-based procedure to solve the Navier-Stokes equations is employed for the first approach in order to compute two-dimensional flow around the riser for each of the horizontal planes in which the riser is divided along its length. According to Sarpkaya (2004), there currently exist several issues to be understood related to the complex nature of the coupling mechanism between the dynamics of the near-wake and that of the riser. Most of the existing implementations of Navier-Stokes solvers for response prediction of flexible risers have been developed for the case in which the riser is excited by steady current. However, a marine riser is also affected by oscillatory flow due to waves and oscillating forces at its top connection. Moreover, an oscillating riser exhibits a more complex response because the shedding frequency can be locked to a natural frequency of the riser several times in contrast to a riser under the action of steady current.

Basically, Direct Numerical Simulation (DNS) and Large Eddy Simulation (LES) are capable of providing better representation of the wake-boundary-layer mechanism as compared to two-dimensional unsteady Reynolds-Averaged Navier-Stokes (RANS) simulations [Sarpkaya (2004)]. However, as noted by Al-Jamal & Dalton (2005), neither 2-D nor 3-D LES simulation is capable of calculating the full flow past stationary cylinder, much less an oscillating one. On the other hand, DNS simulations are extremely computational demanding to be used in practical applications. Finally, turbulence remains poorly understood making CFD-based approach restricted for industrial design as reported by Sarpkaya (2004).

The second approach is referred to as semi-empirical. In this approach, a flexible riser is usually modeled as a beam with low flexural stiffness making use of hydrodynamic force coefficients derived from experiments to calculate the hydrodynamic forces acting on the riser. Therefore, accurate response prediction is strongly related to the availability of reliable experimental data for the modeling conditions involved in a simulation. Chaplin *et al.* (2005a) presented a comprehensive study on response prediction of risers using experimental data obtained from a riser model excited in stepped current and blind predictions from 9 different response prediction models. Chaplin *et al.* (2005a) showed that the

semi-empirical approach is more successful at predicting the cross-flow response of a flexible riser than the CFD-based approach.

The quasi-steady assumption states that the dynamic response of an oscillating flexible riser can be approximated by using hydrodynamic force coefficients derived from experiments performed in fixed cylinders. Therefore, it is commonly accepted the use of force coefficients experimentally derived from oscillatory flow acting on a fixed cylinder to obtain the dynamic response of oscillating flexible risers. Furthermore, Obasaju *et al.* (1988) stated that *even though many different vortex patterns are exhibited in oscillatory flow, the basic mechanism that governs the rate at which vortices develop may be the same as in steady flow.*

VIV can occur in both steady currents and oscillating flow. In steady currents, during lock-in events, the VIV process may also induce large oscillating amplitudes in the riser as the reduced velocity is increased, but when the cross-flow amplitude reaches a certain value, the vortex shedding changes and then the cross-flow amplitude decreases. The oscillating flow case exhibits more complex behavior because the lock-in conditions can be achieved several times. As a result, the later case must be the core of the development of a dynamic response scheme for deep-water risers, which combines steady currents with oscillating flow.

3.1 Response Prediction Model for Flexible Risers in Sheared Flow

The VIV process in a flexible riser causes large-amplitude vibrations as the shedding frequency f_S approaches to one of the natural frequencies of the riser. f_S increases proportionally to the in-line fluid velocity and S_t. The surface roughness and the Re number are commonly used to describe the variation of S_t and it is widely recognized that in the subcritical range, $300 < Re < 1.5 \times 10^5$, $S_t \approx 0.2$. On the other hand, the natural frequencies of a flexible riser obtained in still water are also a function of C_m and the mass ratio, m^*. As previously mentioned, during a lock-in event, f_S usually locks onto a natural frequency of the riser leading to large cross-flow displacements and an increased mean drag coefficient.

A numerical scheme to simulate the VIV response of risers in sheared flow is presented in this section. The Finite Element Method (FEM) is employed in conjunction with the harmonic model to predict the transverse response of the riser during lock-out and lock-in events using experimentally derived transverse lift coefficients from previous research works. The increased mean drag coefficient model presented in Eq. (2.17) is also embedded in the proposed prediction model.

The static and dynamic response of a structure excited by a fluid flow can be represented by the governing differential equation presented in Eq. (3.1).

$$\begin{aligned} m\ddot{u}_x + 2m\xi\omega\dot{u}_x + k_{x1}u_x &= \rho C_m \frac{\pi}{4} D^2 \dot{U}_1 - \rho C_i \frac{\pi}{4} D^2 \ddot{u}_x \\ &+ \frac{1}{2}\rho C_{Dmean} D \left|U_1 - \dot{u}_x\right| \left(U_1 - \dot{u}_x\right) \end{aligned} \tag{3.1}$$

where ω is the natural frequency of the structure without fluid surrounding it and k_{x1} is the stiffness parameter related to the combination of the physical constants of the structure such as Young's modulus and Poisson's ratio and its moments of the inertia. The numerical representation of the transverse (lift) force F_L is incorporated into the numerical model using the time-harmonic model presented by Norberg (2003). This model assumes that regular shedding of vortices produces a sinusoidal force (transverse lift force), which is proportional to the square of U_1 at a given time, t, as shown in Eq. (3.2).

$$F_{Ls} = \frac{1}{2}\rho U^2 D \sqrt{2} C_L' \sin 2\pi t f_S \tag{3.2}$$

Norberg (2003) provided a thorough review of investigations concerning lift forces acting on a stationary circular cylinder in cross-flow and based on those investigations developed empirical functions for the Reynolds number dependence of S_t and C_L'. The empirical formulation proposed by Norberg (2003) is used herein to calculate the lift force, F_L, acting on a riser in the lock-out region. Under lock-in events C_L' is calculated based on experimental data provided by Khalak & Williamson (1999) using experimental models tested at low m^* and ξ. The increased mean drag coefficient model selected in the proposed model corresponds to the one developed by Vandivier (1983) as shown in Eq. (2.17).

3.1.1 Numerical Implementation

The commercial software ABAQUS (2007) is used to assemble the FE model of the riser and an in-house FORTRAN subroutine developed by the author is used to input the hydrodynamic forces to the riser. Due to the inherently nonlinear behavior of a flexible riser response, a nonlinear time-domain method is selected. The Hilber-Huges-Taylor operator is used to solve the resulting nonlinear equilibrium equations at each time increment using Newton's method. A static stress analysis is performed in order to apply the self-weight of the riser. As a result, geometric nonlinearity is included during this step, which is related to large deformations as compared to the original dimensions of the riser. The dynamic response of the riser is then computed using the direct-integration method. The FE model is assembled using 2-node cubic Euler-Bernoulli elements. A total number of 16 elements are used to numerically represent the experimental model presented by Chaplin *et al.* (2005a). A time increment of 0.1 sec. is used during the dynamic step. The FE model initially excited during 20 sec. in order to achieve the steady state without considering the increased mean drag coefficient model, during this stage the in-house FORTRAN subroutine computes the displacements in the cross-flow direction at all nodes in order to calculate the Y_{rms} value. Finally, the dynamic response of the riser including the increased mean drag coefficient model is computed for an equivalent time of ten vortex-shedding cycles. A total number of 16 elements are used to numerically represent the experimental model presented by Chaplin *et al.* (2005a). A time increment of 0.1 sec. is used during the dynamic step. The FE model initially excited during 20 sec. in order to achieve the steady state without considering the increased mean drag coefficient model, during this stage the in-house FORTRAN subroutine computes the displacements in the cross-flow direction at all nodes in order to calculate the Y_{rms} value . Finally, the dynamic response of the riser including the increased mean drag coefficient model is computed for an equivalent time of ten vortex-shedding cycles.

3.1.2 Experimental Model

The experimental model used for the validation of the proposed prediction model was developed by Chaplin *et al.* (2005a). They compared experimental data obtained from a riser model in sheared flow with blind predictions using 9 different numerical models. The experimental model is pinned at its bottom end and has a length of 13.12 m, a diameter of 0.028 m and a mass ratio of 3. The stepped current effect was achieved by mounting the riser model on a towing carriage with the upper 55% of the model in still water condition while the lower 45% was exposed to current. Further details can be found in Chaplin *et al.* (2005a). Blind predictions were carried out using 9 different models mainly divided into two groups. In the first group, CFD approach is used to compute hydrodynamic forces in two-dimensional planes and then input to a model of the riser, four codes are used in the first group as follows: NorskHydro [Herfjord & Kvamsdal (1999)], USP [Yamamoto *et al.* (2004)], DeepFlow [Etienne (1999)] and VIVIC [Willden & Graham (2004)]. The second group is composed of the following five semi-empirical prediction codes: VIVA [Triantafyllou (2003)], VIVANA [Larsen (2000)], VICoMo [Moe *et al.* (2001)], SHEAR7 [Vandivier (2003)] and ABAVIV [Lambrakos & Maher (1999)]. Finally, the test conditions for the nine cases presented by Chaplin *et al.* (2005a), as shown in Table 3.1, are used to validate the proposed prediction model.

Table 3.1: Test Conditions for Blind Predictions Chaplin *et al.* (2005a)

Case	Speed (m/s)	Top Tension (N)
1	0.16	405
2	0.21	407
3	0.31	457
4	0.40	506
5	0.54	598
6	0.60	670
7	0.70	743
8	0.85	923
9	0.95	1002

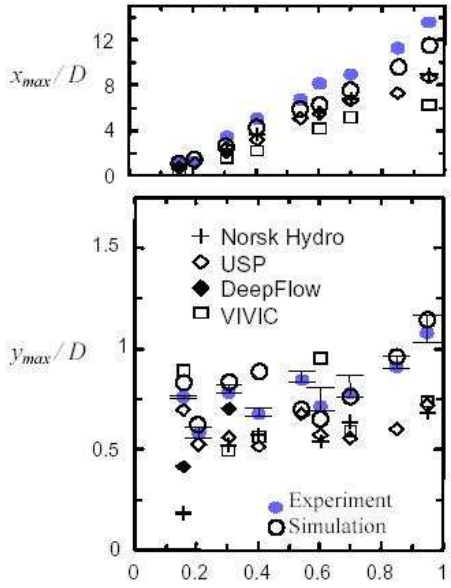

Figure 3.1: Group No.1 U_{x0}

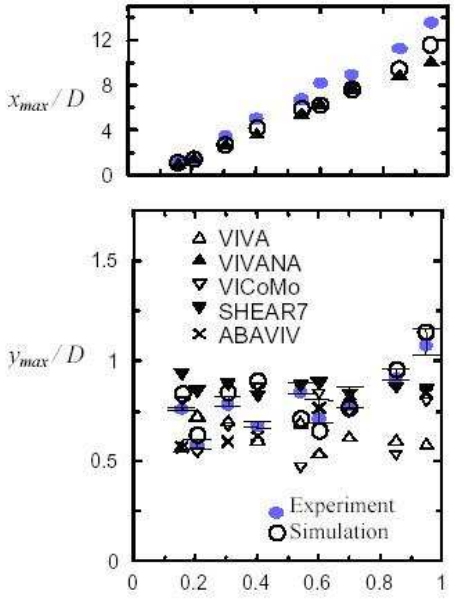

Figure 3.2: Group No.2 U_{x0}

3.1.3 Simulation Results

The value of C_{Dmean} used in the simulations was 0.7 and the value of C_i was 1.0 [Chaplin *et al.* (2005a)]. During lock-in events the values of the maximum and minimum C_L' used in the simulations were 1.25, which corresponds to a $U_r = 5$, and 0.5 at $U_r = 6$, respectively [Khalak & Williamson (1999)]. The natural frequencies of the riser were computed in still water using an eigenvalue extraction procedure prior to the dynamic analysis and during lock-in events, the computed shedding frequency was locked to the nearest lower natural frequency as previously explained. The simulation results obtained with the proposed prediction model are shown in Figs. 3.1 and 3.2. The maximum in-line and cross-flow displacements are represented by x_{max} and y_{max}, respectively.

3.1.4 Concluding Remarks

In this section, a dynamic prediction model for risers in sheared flow was presented. Experimental data obtained from a flexible riser model were compared

with the simulation results obtained from the proposed numerical scheme. Additional comparisons were made using simulations results obtained from 9 numerical models. Good agreement is observed in both in-line and cross-flow response. The increased mean drag coefficient model accurately represents the increment of the in-line forces during lock-in events leading to an increment of the in-line velocity and lift forces.

Although the calculation of the natural frequencies of a riser is based in several assumptions and may deviate from its real values, the methodology proposed in this section captures most of the VIV process during lock-in events. It is still challenging the numerical representation of the lock-in process, when a riser is excited under lock-in events the shedding frequency is expected to lock onto the nearest lower natural frequency. However, a flexible structure such as a riser, usually has several natural frequencies having values lower than the oscillating frequency of the riser. Therefore, the selection of the lock-in frequency may involve errors in its selected value.

Another important issue to be considered for further studies is the influence of the mass ratio in the maximum displacement that can be achieve by the riser under lock-in events. It is widely accepted that for low mass-damping values the expected maximum cross-flow displacement is lower than 1.2 diameters. The experimental and simulation results presented by Chaplin *et al.* (2005a) are located in this region as well as the results obtained from the proposed prediction model. Several issues need further study. The values of the lift coefficients during lock-in events may considerably deviate from the values obtained under lock-out events. In addition, the Strouhal law may not be followed by the shedding frequency when is approaching to a natural frequency of a riser leading to inaccuracies in the lock-in numerical models. Finally, at resonance the hydrodynamic damping plays an important role in limiting the maximum cross-flow displacements.

3.2 Response Prediction Model for Short Flexible Risers

A response prediction model for short flexible risers without considering lock-in events is presented in this section. In-line motion is numerically represented using Eq. (3.1). The analytical representation of F_{Lo} is incorporated into the numerical scheme by using the quasi-steady procedure presented by Obasaju *et al.* (1988). This model is used in conjunction with the left-hand side of the Eq. (3.1) to represent the cross-flow response of the structure using the corresponding stiffness parameter and the relative displacement of the structure in the cross-flow direction. Therefore, F_{Lo} can be represented as shown in Eq. (3.3), where the phase angle, ϕ, is considered.

$$F_{Lo} = \frac{1}{2}\rho U_0^2 D C_{Lmax} \sin\left(2\pi t f_L + \phi\right) \tag{3.3}$$

3.2.1 In-line Response Validation

The numerical scheme is implemented in free-end riser models, these models are sinusoidal excited at their top end and free supported at their bottom end. Hong & Koterayama (2004) developed a new analytical scheme for dynamic response of flexible risers under controlled environmental conditions and compared the results obtained from their analytical scheme with experimental data. Transverse force was not considered in the numerical scheme [Hong & Koterayama (2004)]. The experimental model has a length of 6.5 m, Young's modulus of 8.847 MPa, outer diameter of 0.0225 m, inner diameter of 0.0127 m and density of 1476 kg/m^3. A bottom weight is added to the model in order to keep it straight during the dynamic tests. This bottom weight has a diameter of 0.034 m, a total length of 0.093 m and a weight in water of 3.489 N.

The experimental riser model presented by Hong & Koterayama (2004) is simply supported at its top end and free supported at its bottom end. The riser model is excited at its top end by a sinusoidal forced oscillation motion in the in-line direction with amplitude of 0.1 m and forced oscillation periods of 2 sec., 6 sec. and 10 sec. The FE model is assembled using 20 pipe elements; one circular

element is used for the bottom weight. At the water level there is no horizontal velocity component and geometric non-linear procedure is used to load the riser by its self-weight and the bottom weight during the static step. Then, drag and inertia loads are applied to the riser during the dynamic step.

The experimental model presented in this section is sinusoidally excited at Re numbers up to 2000 and KC numbers up to 28. This regime is named the third vortex $22 < KC < 30$ by Obasaju *et al.* (1988). In this regime three full vortices are formed during each half cycle and three vortex pairs convect away from the cylinder during a complete cycle. Experimental studies had shown that the dominant frequency is 4 times the in-line oscillating frequency. In this numerical implementation, the in-line maximum velocities for each of the 20 pipe elements are used to compute the dominant frequencies f_L. Another important parameter to be considered in the quasi-steady model is β, because several experimental studies have shown that hydrodynamic force coefficients depend on β at low KC numbers ($KC < 15$), but in the third vortex region can be assumed without loss of accuracy that hydrodynamic force coefficients only depend on the KC number at low Re numbers ($Re < 14200$) as reported by Senga & Koterayama (2005).

The FE model is initially excited without considering F_{Lo}, during this stage the in-house FORTRAN subroutine computes the maximum displacements and velocities at all nodes. A time increment of 0.1 sec. is used during the dynamic step. The KC numbers and C_{Lmax} for all sections are calculated using the maximum displacements and velocities computed in the previous stage. The procedure to calculate the ϕ is based on the time difference between the time required for each section of the FE model to achieve its maximum displacement and the required time at the top end to achieve the same condition. The in-house FORTRAN subroutine computes and applies F_{Lo} to each element of the FE model using Eq. (3.3).

The time-history responses of the riser at the selected positions are calculated for an excitation period of 2 sec. The simulation and experimental results obtained by Hong & Koterayama (2004) are presented in Figs. 3.3 and. 3.5. The simulation results obtained from the proposed numerical scheme are shown in Figs. 3.4 and. 3.6.

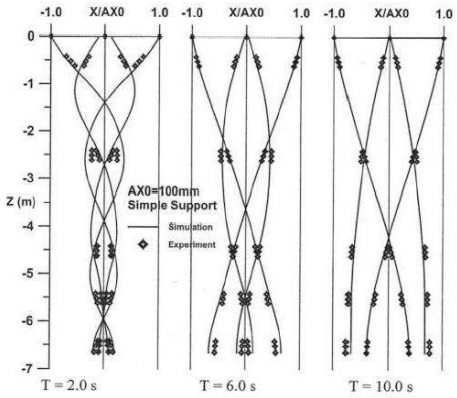

Figure 3.3: u_{x0} Hong & Koterayama (2004)

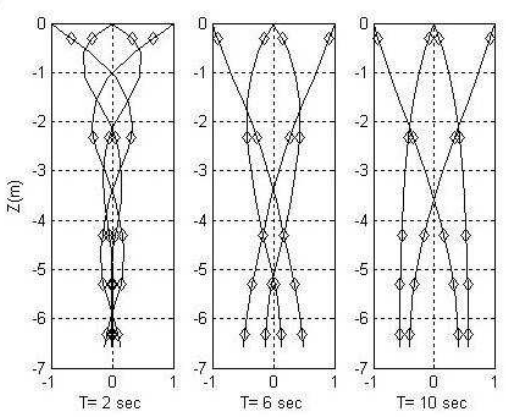

Figure 3.4: u_{x0} Proposed Model

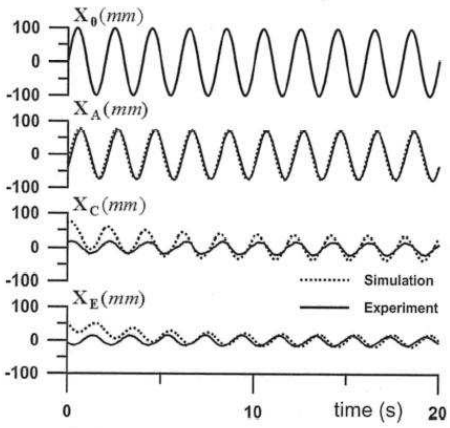

Figure 3.5: $u_x(t)$ Hong & Koterayama (2004)

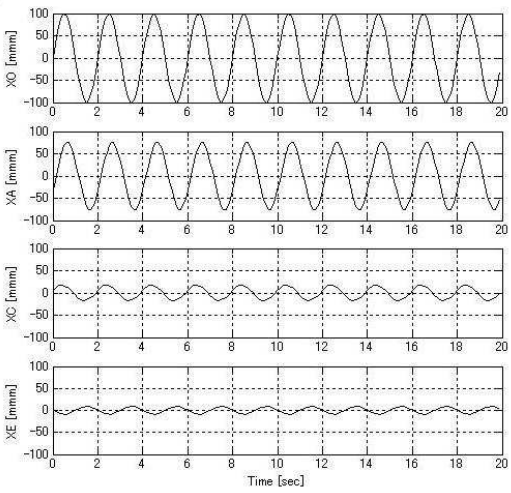

Figure 3.6: $u_x(t)$ Proposed Model

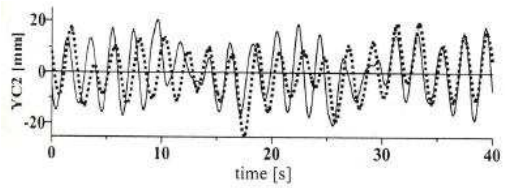

Figure 3.7: $u_y(z = -4.31, t)$ Senga & Koterayama (2005)

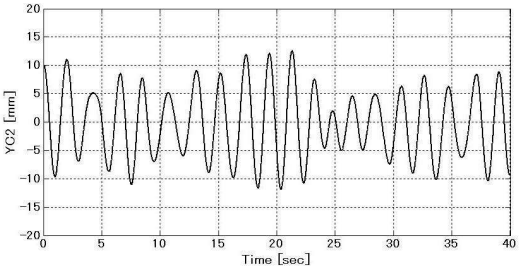

Figure 3.8: $u_y(z = -4.31, t)$ Proposed Model

3.2.2 Cross-Flow Response Validation

Senga & Koterayama (2005) improved the previous analytical scheme, [Hong & Koterayama (2004)], by including the transverse (lift) force, which was represented by a sinusoidal equation using the instant vortex shedding frequency and the instant in-line velocity. A second riser model, having the same material and geometric properties from the model previously presented, is used to carry out the transverse response validation. The boundary condition at the top-end is simply supported. The experimental riser model is excited by a sinusoidal forced oscillation motion with amplitude of 0.1 m and forced oscillation period of 8 sec. According to Senga & Koterayama (2005) the oscillation parameters avoid the lock-in condition, because the oscillating frequency is located in between the nearest natural frequencies of the model. The riser model developed by Senga & Koterayama (2005) has fundamental periods of 11 sec., 4.8 sec., 3.1 sec. and 2.3 sec. The simulation and experimental results obtained by Senga & Koterayama (2005), using the transverse response of the riser model at a depth of 4.31 m, are shown in Fig. 3.7. The simulation results obtained from the proposed numerical scheme are shown in Fig. 3.8. In the proposed numerical scheme the hydrodynamic coefficients were obtained from experiments conducted by Koterayama & Nakamura (1988), and the maximum lift coefficients were obtained from Bearman *et al.* (1984).

3.2.3 Concluding Remarks

Experimental data obtained from a flexible riser model were compared with the simulation results obtained from the proposed response prediction model. Good agreement is observed between simulation and experimental results. Two free-end riser models were used to validate the in-line and the transverse response. The in-line response is accurately represented by the proposed response prediction model and the transverse response also shows good agreement. The lock-in condition, when the vortex shedding frequency approaches to a natural frequency of the riser is not achieved. Therefore, an amplification model for C_{Dmean} was not included in the proposed response prediction model. The experimental and analytical results presented by Hong & Koterayama (2004) and Senga & Koterayama (2005) are successfully simulated by the proposed response prediction model.

3.3 Response Prediction Model for Tensioned Flexible Risers

The Euler-Bernoulli beam equation is used herein to model a riser idealized as a beam with low flexural stiffness following the procedure proposed by Huera-Huarte *et al.* (2006) as shown in Eq. (3.4). A Cartesian reference is defined in the x-axis by the direction of the flow velocity in the case of a stationary body or the in-line motion in the case of an oscillating body, the z-axis is defined in the direction of the riser's axis and the y-axis is perpendicular to both Fig. 3.9. Where $AX0$ is used to define the amplitude of the in-line motion, $u_{x,y}$ is the deflection, m is the mass of the riser per unit length, ξ is the damping coefficient, EI is the flexural stiffness, T_t is the tension applied at the top end of the riser, L is the length of the riser and w is the submerged weight.

$$EI\frac{\partial^4 u_{x,y}(z,t)}{\partial z^4} - \frac{\partial}{\partial z}\left[(T_t - w(L-z))\frac{\partial u_{x,y}(z,t)}{\partial z}\right] + \xi\frac{\partial u_{x,y}(z,t)}{\partial t} + m\frac{\partial^2 u_{x,y}(z,t)}{\partial t^2} = F_{Tx,y}(z,t) \tag{3.4}$$

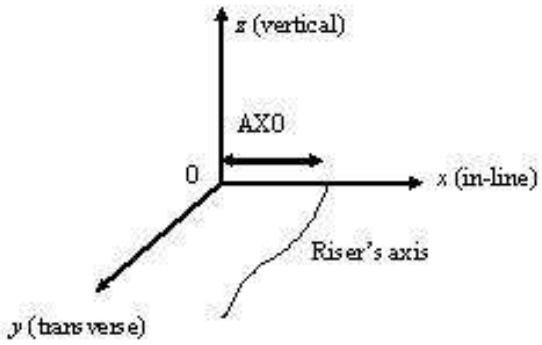

Figure 3.9: Riser Motion and Coordinate System

The analytical representation of in-line forces acting on a riser presented by Carberry *et al.* (2005) is used herein to model the external fluid force acting in the x-axis as shown in Eq. (3.5).

$$F_{Tx}(z,t) = \rho C_m \frac{\pi}{4} D^2 \dot{U}_1 - \rho C_i \frac{\pi}{4} D^2 \ddot{u}_x + \frac{1}{2}\rho D \left|U_1 - \dot{u}_x\right| \left(U_1 - \dot{u}_x\right) \left[C_{Dmean} + C_D \sin\left(2\left(2\pi t f_L + \phi_{drag}\right)\right)\right] \tag{3.5}$$

where f_L is defined as the most dominant frequency in the y-axis or cross-flow direction based on the fact that transverse response in flexible risers is a multi-frequency phenomena. ϕ_{drag} is the phase of the drag with respect to the cylinder's displacement in the cross-flow direction. It is widely recognized that the dominant frequency of the drag force is two times the dominant frequency in the cross-flow direction ($2f_L$). Therefore, ϕ_{drag} is used to relate the phase of the drag to the displacement of the riser in the cross-flow direction and it is experimentally derived from drag traces whose correlation coefficient with a sinusoidal signal is greater than 0.6 as proposed by Carberry *et al.* (2005). f_L is related to the cross-flow motion and is used to calculate the transverse force as shown in Eq. (3.6).

$$F_{Ty}(z,t) = \frac{1}{2}\rho U_0^2 D C_L \sin\left(2\pi t f_L + \phi_{lift} + \theta\left(z\right)\right) \tag{3.6}$$

$\theta(z)$ is related to an initial phase angle that is used to couple in-line and cross-flow motions allowing the correct application of a particular section of the riser and considering the existing difference in the values of phase angle of the traveling wave originated at the top end of the riser and the remaining regions in the case of a riser excited at its top end, which is the case considered in this section. Detailed explanation related to the numerical calculation of this parameter is provided in Section 3.3.2. f_L mainly depends on the KC number and S_t. Obasaju *et al.* (1988) showed that the vortex patterns around a circular cylinder in oscillating flow can be approximately divided into five regimes, namely the asymmetric ($4 < KC < 8$), the transverse ($8 < KC < 15$), the diagonal ($15 < KC < 22$), the third vortex ($22 < KC < 30$), and the quasi-steady ($KC > 30$). Each of these regimes is characterized by an approximate f_L.

Sarpkaya (1995) decomposed the instantaneous cross-flow force using a two-coefficient model into inertia and drag components in order to study its dependency on the cross-flow amplitude A_y. Three representative values of A_y/D ($=$ 0.25, 0.50 *and* 0.75) were used to experimentally proved that the drag component of the instantaneous cross-flow force becomes negative in the vicinity of the synchronization region defined as the matching of the shedding frequency and the natural frequency of the cylinder in the cross-flow direction. This negative component of the drag force is commonly defined as *negative damping* and therefore produces amplification of the oscillations. It was found by Sarpkaya (1995) that the maximum negative amplitude of the drag component of the cross-flow force is achieved around $A_y/D = 0.5$ and then decreases. The oscillations become self-limiting for A_y/D larger than about unity. As noted by Sarpkaya (2004), the larger the amplitude of VIV oscillations, the more nonlinear is the dependence of the lift forces on A_y/D. Blevins (1990) proposed an empirical formulation to represent the variation of the lift coefficient with respect to the amplitude of the cross-flow motion A_y. The three-term polynomial derived by Blevins (1990), presented in Eq. (3.7), is used in this section to calculate the lift coefficients required for the numerical implementation of Eq. (3.6). Basically, the empirical formulation presented by Blevins (1990) assumes that as A_y approaches to $1.0D$, a breakdown of regular vortex street is produced and the value of the lift coefficient decreases.

$$C_L = 0.35 + 0.6\left(\frac{A_y}{D}\right) - 0.93\left(\frac{A_y}{D}\right)^2 \tag{3.7}$$

Sarpkaya (2004) defined synchronization or lock-in as a phase transformer due to the fact that synchronization produces a rapid inertial force decrement and a rapid increment of the absolute value of the drag force. Sarpkaya (2004) stated that synchronization is achieved when the reduced velocity, U_r, reaches a value between 4 and 8. Sarpkaya (2004) found an increase of 3.5 times in the mean drag coefficient of an oscillating cylinder involving simultaneous oscillations in the in-line and the cross-flow directions when is compared with the case of static cylinder. Park *et al.* (2003) using a rubber pipe (length of 6 m and diameter of 0.02 m) with its upper end fixed to a towing carriage and setting its bottom end to be free concluded that it was only possible to achieve good agreement between experiments and numerical simulation if enhanced drag coefficients due to vortex induced vibrations are considered. The increased mean drag coefficient used in this section corresponds to Eq. (2.20).

Khalak & Williamson (1999) highlighted the importance of appropriately defining the oscillation frequency and based on their experimental study found that the *classical* definition of synchronization as *frequency matching* between the oscillating frequency and the natural frequency of an oscillating body is not appropriate for the low mass-damping ($m^*\xi$) case, where m^* is the mass ratio calculated as the mass of a body divided by the mass of the fluid displaced and ξ is defined as the ratio of ((structural damping)/(critical damping)). Khalak & Williamson (1999) concluded that a more appropriate definition of synchronization can be stated as the matching of the frequency of the periodic wake vortex mode with the body oscillation frequency. This statement is adopted in the response prediction model presented in this section. Based on the aforementioned fact, it is important to note that the dynamic response of a flexible riser with a value of m^* lower than 3.3 is more complex due to the existence of 3 modes of response, in contrast with the 2 modes of response found in risers with values of m^* larger than 10. On the other hand, the damping force acting on a flexible riser is due to structural damping and fluid damping. In water structural damping will often be relatively small compared to fluid damping, and may therefore be of a

secondary influence. Therefore, the mass-damping parameter plays a crucial role in the type of response achieved by a flexible riser. Moreover, the peak amplitude in the cross-flow direction is strongly related to this parameter. Khalak & Williamson (1999) collected experimental and simulation data in order to establish a confident range for this peak value. Some differences were found when the flow acting on a cylinder corresponds to low Reynolds numbers. A peak value of $0.6D$ was found by Khalak & Williamson (1999) for low Re numbers and $1.2D$ for high Re numbers. A more recent study presented by Willden & Graham (2006) at Re numbers between 50 and 400 stated that for the low-Re region, the peak amplitude in the cross-flow direction is independent of the mass-ratio parameter showing a peak value of $0.5D$.

3.3.1 Experimental Validation

In recent years, several experiments have been conducted in order to validate response prediction models for risers. Chaplin *et al.* (2005a) conducted a series of experiments using a riser model (13.12 m long and 0.028 m diameter) in stepped current. The Re numbers achieved in the experiments conducted by Chaplin *et al.* (2005a) ranged from 4480 to 26600 and by comparing the experimental data with 11 different numerical models it was found that the in-line and cross-flow displacements were underpredicted by 20% to 40% and by 10% and 30%, respectively. On the other hand, risers are usually subjected to a combined loading of waves and currents. Therefore, some of the riser models have been tested under oscillatory flow or oscillating body conditions as previously explained. Duggal & Niedzwecki (1995) conducted a large-scale experimental study to investigate the dynamic response of a riser model constructed from ABS plastic tubing having a length of 17.18 m, a diameter of 0.032 m and pinned at its both ends. The model was excited at KC numbers ranging from 10.6 to 52.7 and based on the analysis of the experimental data Duggal & Niedzwecki (1995) concluded that the cross-flow response show similarities with previous research work using oscillatory flow in rigid cylinders. More recently, Jung *et al.* (2005) tested a highly flexible free hanging pipe in calm water. The pipe was 6 m long, 0.02 m diameter and was excited by top-end oscillations. Comparisons between experiments and

numerical results using the model developed by Jung *et al.* (2005) showed that in-line displacements were well predicted at the upper part of the model, but some differences were found in the lower part due to large interaction between in-line motion and vortex-induced transverse motion.

In this section, large-scale experiments are conducted to validate the proposed prediction model. A 20-meter riser model, pinned at its both ends, is sinusoidally excited at its top end using a wide range of KC numbers in accordance with the regimes proposed by Obasaju *et al.* (1988). The forced oscillation experiments are carried out in the deep-sea basin of the Integrated Laboratory for Marine Environmental Protection located in the National Maritime Research Institute (NMRI). This deep-sea basin is depicted in Fig. 3.10 and consists of a circular basin (depth: 5 m, effective diameter: 14 m) and a deep pit (depth: 30 m, effective diameter: 6 m). The underwater 3-dimensional measurement equipment is composed of 20 high-resolution digital cameras (2 units/set x 10 sets).

The properties of the model are presented in Table 3.2. Fig. 3.11 shows the experimental model placed in its initial position before being excited. Its coordinate system is defined in the x-axis by the in-line motion, the y-axis corresponds to the transverse motion and the z-axis is defined in the direction of the riser's axis as illustrated in Fig. 3.9. The model is sinusoidally excited in still water along the x-axis. Steel bars are added to the riser model in order to increase its self-weight. The total weight of the riser, including the steel bars, is 68.14 N. The tension force applied at the top end of the model in the z-axis corresponds to a value of 63.5 N. The experimental validation of the proposed response model is carried out for different values of amplitudes and periods regarding the oscillation force at its top end as shown in Table 3.3. Depending on the value of KC the cases presented in Table 3.3 can be classified into either three[1] or six[2] regimes.

3.3.2 Numerical Implementation

The Finite Element Method (FEM) is used herein to numerically solve the differential equation governing the static and dynamic response of a flexible riser

[1] Zhou & Graham (2000)
[2] Obasaju *et al.* (1988)

Figure 3.10: Deep-sea Basin (NMRI)

Figure 3.11: Experimental Riser Model (NMRI)

Table 3.2: Properties of the Riser Model

Material	Polyoxymethylene
Model length (m)	20
Outer diameter D (m)	0.016
Inner diameter (m)	0.0108
Density (Kg/m^3)	1410
Young's modulus E (MPa)	2.937

Table 3.3: Excitation Cases of the Riser Model

Case	Amp. (m)	T (sec.)	Re	KC	Regime[1]	Regime[2]
1	0.010	2	499	3.9	inertia	symmetric
2	0.020	2	1011	7.9	inertia/drag	asymmetric
3	0.027	3	904	10.6	inertia/drag	transverse
4	0.040	4	1005	15.7	inertia/drag	diagonal
5	0.060	2	3021	23.6	inertia/drag	third vortex
6	0.080	2	4091	31.4	drag	quasi-steady

presented in Eq. (3.4). The commercial software ABAQUS (2007) is selected to carry out this numerical implementation. The riser is modeled as an assembly of 40 cubic pipe elements. Therefore, the actual shape function of a nonlinear beam is more closely fit due to the element cubic shape functions employed in this procedure. Geometric nonlinearity is considered by using a nonlinear time-domain method during the application of the riser's self-weight. The dynamic response of the riser is then computed employing the direct-integration method. An in-house FORTRAN subroutine (developed by the author) computes displacements, velocities and accelerations at each time step in order to generate the data needed for the numerical implementation of the amplitude-dependent lift and increased mean drag coefficient models. The developed subroutine compares current and previous results. Therefore, representative peak values can be found at each stage of the simulation.

Carberry *et al.* (2005) experimentally proved that the wake states for forced oscillations are remarkable similar to the response branches of elastically mounted

cylinders. Khalak & Williamson (1999) found an intermittent switching between the upper and the lower branch amplitudes and phase angles in the cross-flow direction. On the other hand, there is a hysteretic response from the initial to the upper branch. Both of the mode transitions are related to jumps in amplitude and frequency and a 180° jump occurs only when the flow moves between the upper and the lower branches. This complex hysteretic behavior adds uncertainties in the numerical implementation of Eq. (3.5). The identification of the exact value at which an increment of U_r produces a jump to a new branch cannot be assessed with good accuracy considering the length of the riser model presented in this section. Therefore, ϕ_{lift}=0° is assumed for this numerical implementation. The value of the phase angle, ϕ_{drag}, is obtained from Carberry *et al.* (2005). They found that the nature of the in-line motion tends to be less sinusoidal than the cross-flow motion showing a jump of approximately 240° in the transition between the lower and initial branches. The variability of ϕ_{drag} is markedly larger than ϕ_{lift} , but when the shedding frequency matches the oscillating frequency its value tends to be zero. C_D=0.3 is selected according to Carberry *et al.* (2005).

The KC numbers achieved by the riser model presented in this section correspond to the symmetric, asymmetric, transverse, diagonal, third vortex and quasi-steady regimes providing a wide range of experimental validation. It is important to highlight that Lin *et al.* (1996) identified the existence of a region located around KC=10 where there is a rapid rise of C_{Dmean} and decrease of C_m. The mean drag coefficient rises approximately from 1.5 at KC=6 to 2.1 at KC=10. According to Lin *et al.* (1996), two-dimensional simulation around KC=10 fails to predict this peak due to three-dimensional flow features. On the other hand, there is a rapid decrease of C_m in the same region ($6 < KC < 10$). Obasaju *et al.* (1988) presented a comprehensive study of a circular cylinder in planar oscillatory flow at KC numbers ranging from about 4 to 55. It was experimentally proved that there is a range of the β parameter in which C_{Dmean} is not sensitive to changing β. It was also identified that the upper boundary of this range lies between $\beta = 964$ and 1204. The maximum value of the β parameter achieved by the riser model is 128. Therefore, C_{Dmean} and C_m coefficients experimentally computed by Obasaju *et al.* (1988) at $\beta = 196$ are used for the

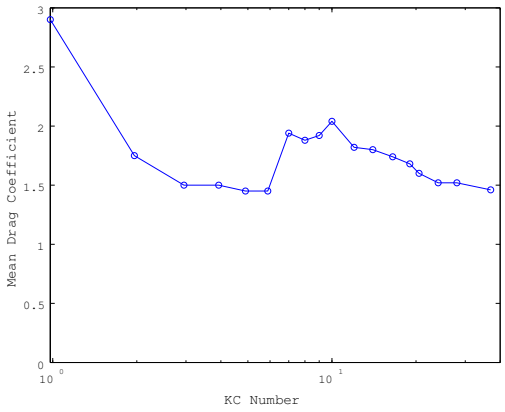

Figure 3.12: Values of C_{Dmean}

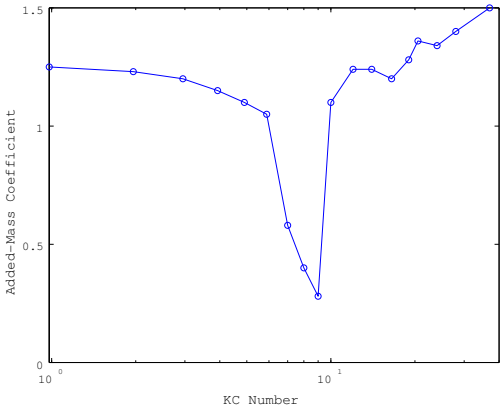

Figure 3.13: Values of C_i

numerical implementation of the proposed prediction model. The simulation results presented by Lin *et al.* (1996) are used for $KC < 4$. Figs. 3.12 and 3.13 show the values of C_{Dmean} and C_i used in the numerical implementation. Finally, large-amplitude vibrations due to synchronization events and a low m^* value are the main characteristics of the long flexible riser model presented in this section. Therefore, a value of ξ of 0.3% was included in the prediction model using as a reference the value of ξ presented by Huera-Huarte *et al.* (2006).

It is also important to highlight that during synchronization, the riser vibration is only limited by its structural damping. However, once the amplitude reaches about $1.0D$, its vibration becomes self-limiting. Blevins (1990) stated that in-line VIV usually occurs with twice of the shedding frequency in the range $2.7 < U_r < 3.8$. The occurrence of both in-line and cross-flow synchronization events is carried out by computing U_r at each time step and if its value is between 2.7 and 3.8, the fluctuating drag force part of Eq. (3.5) is included in the calculation. On the other hand, if U_r is located in between 4 and 8, the increased mean drag coefficient model is used to compute the magnitude of the drag force.

In the numerical implementation of the proposed prediction model, hydrodynamic forces are first applied using fixed values of drag and added-mass coefficients. These forces are applied during 14 cycles. Then, at the end of the first stage, in-lines amplitudes are calculated and used to update the drag coefficients based on KC values, at the same time the cross-flow forces are applied during

6 additional cycles. Synchronization events in both in-line and cross-flow are included in the third stage when the values of C_{Dmean}, C_i and C_L are updated. This stage lasts 48 additional cycles. This procedure is summarized in Table 3.4. The computation of the in-line and cross-flow forces is carried out by the in-house FORTRAN subroutine and then input to the FE model of the riser at each time step. f_L mainly depends on the KC number and S_t. Therefore, S_t is numerically calculated based on the empirical formulation proposed by Norberg (2003).

Table 3.4: Subroutine Procedure

First Stage	Second Stage	Third Stage
14 cycles	6 cycles	48 cycles
fixed C_i and C_{Dmean}	updated C_i and C_{Dmean}	updated C_i and C_{Dmean}
	fixed C_L	updated C_L
in-line force	in-line and cross-flow forces	consideration of lock-in

The numerical implementation of Eq. (3.6) requires the correct calculation of $\theta(z)$. However, the initial riser's response is transient due to a time-varying load. It takes approximately 4 seconds for the wave originated at the top end of the riser to completely excite its bottom end. Then, the steady response is achieved and all sections of the model are excited at different frequencies, amplitudes and phase angles. Therefore, an algorithm is used to approximately compute $\theta(z)$ by using the difference between the time required for each section of the model to achieve its maximum in-line displacement and the time at the top end of the riser to achieve the same condition. Therefore, $\theta(z)$ allows the correct application of $F_{Ty}(z,t)$ at the end of the first stage. The main consideration behind the use of this parameter is that it considers the existing differences in the in-line phase angles for all the sections in which the riser is divided. As a result, $F_{Ty}(z,t)$ is correctly applied at the beginning of the second stage. Otherwise, wrong in-line amplitudes obtained during the transient response may under-estimate the phase angle and lead to out-of-phase response between the in-line and the cross-flow motions of the riser. In the following sections the simulation results are provided using as a reference the three regimes previously proposed by Zhou & Graham (2000).

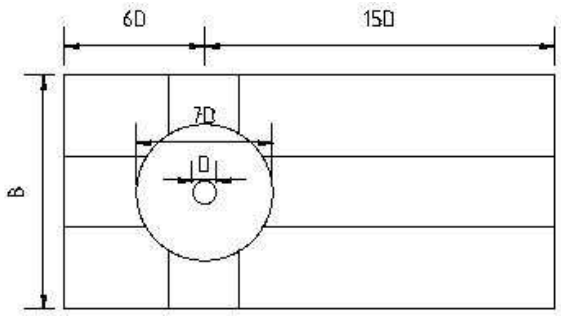

Figure 3.14: Computational Domain

3.3.3 Inertia Regime

As previously mentioned, existing semi-empirical models for response prediction of risers highly depend on the experimentally derived values of hydrodynamic force coefficients. Therefore, most of those models rely on large databases of force coefficients. On the other hand, the quasi-steady approach assumes that hydrodynamic force coefficients can be used for oscillating flexible risers. As a result, static fluid forces due to oscillatory flow can be used to predict hydrodynamic forces acting on an oscillating body.

A more straightforward approach is the modeling of the sinusoidal movement of the cylinder in the in-line direction while computing the cross-flow forces due to shed of vortices. The cylinder is therefore allowed to freely move in the cross-flow direction. At low amplitudes it is expected similar simulation results for the cases of oscillatory flow acting on a fixed cylinder and an oscillating cylinder in otherwise calm water. In this section, a CFD-based model for prediction of in-line hydrodynamic force coefficients is developed using the commercial finite volume CFD code, named FLUENT (2007). Its validation is carried out using experimental and simulation results from previous studies in fixed cylinders. Fig. 3.14 depicts the computational domain assembled in GAMBIT (2007). A blockage ratio (D/B) of 10% is selected in this section based on the simulation results presented by Anagnostopoulos & Minear (2004), who performed a parametric study using blockage ratios ranging from 10% to 50% and found that the blockage effect is almost negligible for blockage ratios lower than 20%.

The final grid is composed of 17494 nodes. The cylinder is placed in the center of a circular domain composed of triangular cells. The remaining regions of the computational domain are composed of quadrilateral cells. The solution is time-dependent (time step of 0.01 sec.). Therefore, an unsteady solver is used herein allowing the modeling of the oscillatory flow condition. The experimental model presented in this section is sinusoidally excited at Re numbers up to 600 and KC numbers up to 5, which correspond to a β parameter of 120.

Based on the Re numbers achieved by the riser, a laminar viscous model is selected. The proposed model is first validated for steady flow at Re=100. Zhou & Graham (2000), using a vortex-based method to simulate flow around a circular cylinder, found a value of C_{Dmean} of 1.37. They compared this value with 15 experimental and numerical results and found good agreement in their comparisons. The model proposed in this section is therefore implemented for the same simulation conditions presented by Zhou & Graham (2000). The C_{Dmean} value computed from the proposed model is remarkably similar to the one presented by Zhou & Graham (2000) having a value of 1.38. Fig. 3.15 shows the C_{Dmean} values computed from the proposed model. It is possible to observe good agreement between the computed values and the experimental values presented by Anderson (1991).

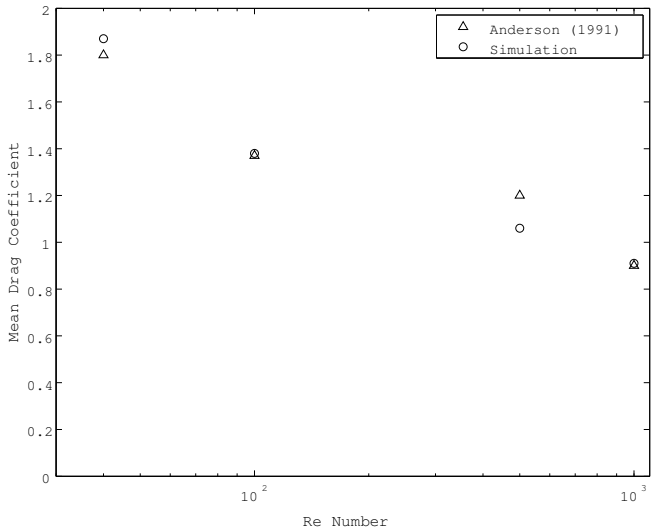

Figure 3.15: Computed C_{Dmean} vs Experimental Values

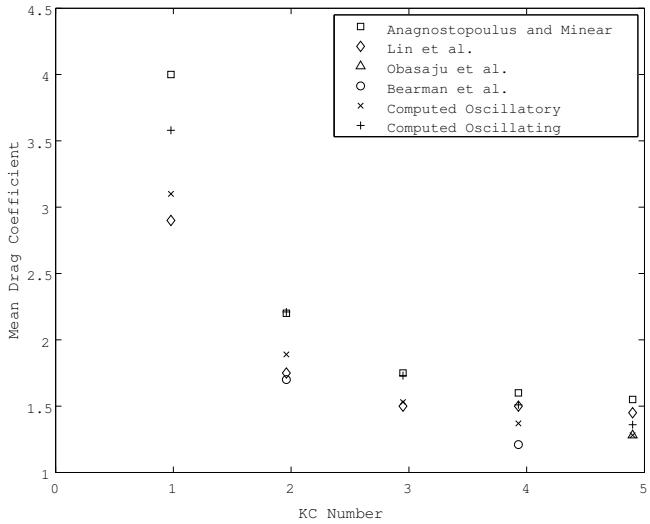

Figure 3.16: C_{Dmean} Oscillatory Flow

Oscillatory flow with amplitudes ranging from 0.0025 m to 0.0125 m and period of 2 sec. is simulated using a user defined function (UDF) developed by the author. C_{Dmean} and C_m are then calculated through least squares fit of the force time series. As previously mentioned, Obasaju *et al.* (1988) experimentally found that there is a range of β in which C_{Dmean} is not sensitive to changing β. It was identified that the upper boundary of the range lies between $\beta = 964$ *and* 1204. Therefore, the simulation results obtained from the proposed model are compared with the ones found by Anagnostopoulos & Minear (2004) at β=50, Obasaju *et al.* (1988) at β=196, Lin *et al.* (1996) at β=70 and Bearman *et al.* (1985) at β=200 as shown in Figs. 3.16 and 3.17. Finally, the proposed CFD-based model is numerically implemented for the oscillating body case. The moving/deforming mesh capability provided by FLUENT (2007) is used herein to sinusoidally move the cylinder in the in-line direction while applying pressure forces in the cross-flow direction based on the explicit Euler formulation presented in Eq. (3.8) . The main idea of this procedure is to use the computed velocities at which the cylinder is excited in both in-line and cross-flow directions and then allows the cylinder to move in accordance with these velocities. In order to improve the simulation results, a time step Δt of 0.001 sec. is selected in Eq. (3.8).

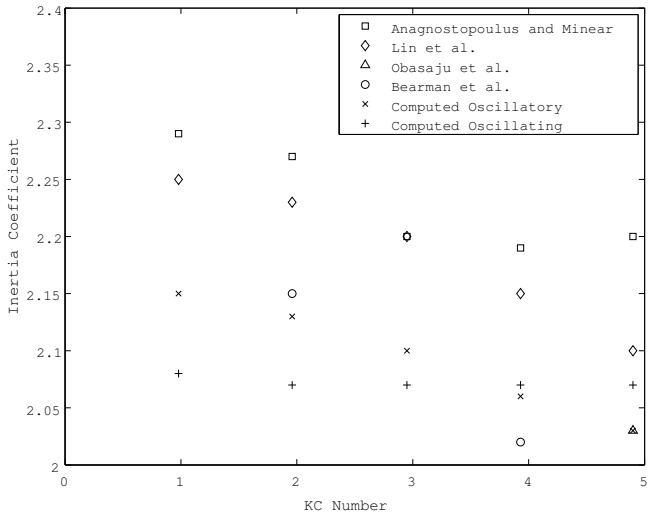

Figure 3.17: C_m Oscillatory Flow

$$v_t = v_{t-\Delta t} + \frac{F_p}{m}\Delta t \tag{3.8}$$

where v_t is the velocity of the cylinder in the cross-flow direction and F_p is the pressure force in the same direction at a given value of time t. The cylinder is then allowed to sinusoidally move in the in-line direction with amplitudes ranging from 0.0025 m to 0.0125 m and period of 2 sec. In the cross-flow direction, the computed pressure forces are used to move the cylinder based on the cross-flow velocity computed from Eq. (3.8). The aforementioned procedure is repeated at each time step. The simulation results for the oscillating body case are also presented in Figs. 3.16 and 3.17. The oscillatory flow and oscillating body results are related to a fixed cylinder excited by oscillatory flow and an oscillating body in otherwise calm water, respectively.

It can be seen from Fig. 3.16 that the values of the C_{Dmean} computed from the oscillatory flow and oscillating body cases are in good agreement with the experimental and simulation data provided by previous studies. The simulation results presented in this section also support the statement given by Obasaju *et al.* (1988) as previously mentioned. The simulation results presented in Fig. 3.17 show that it is important to consider the value of β in the calculation of C_m. It is also important to highlight that for the oscillating body case C_i is

obtained through least squares fit of the force time series and it is assumed that C_m=C_i+1.0. Finally, it is observed that there is no significant variation of C_m for the KC numbers presented in this section. The computed values of C_m show lower values than the ones obtained from the oscillatory flow case showing the importance of fluid-structure interaction, which is expected to be significant at large amplitudes.

Time series response during 20 seconds obtained from the proposed prediction model and experimental data are shown in Figs. 3.18, 3.19 and 3.20. In-line and transverse responses were computed at depths of 5 m, 7 m, 9 m, 10 m, 12 m and 15 m. The experimental data were passed through a 6th order high-pass Butterworth filter with a 0.1 Hz cutoff. The in-line phase angles were corrected in order to improve the quality of the graphical results. Variations in the phase angles were found when the experimental results were compared with simulation results. These variations may be caused in part by the initial unsteady response of the riser.

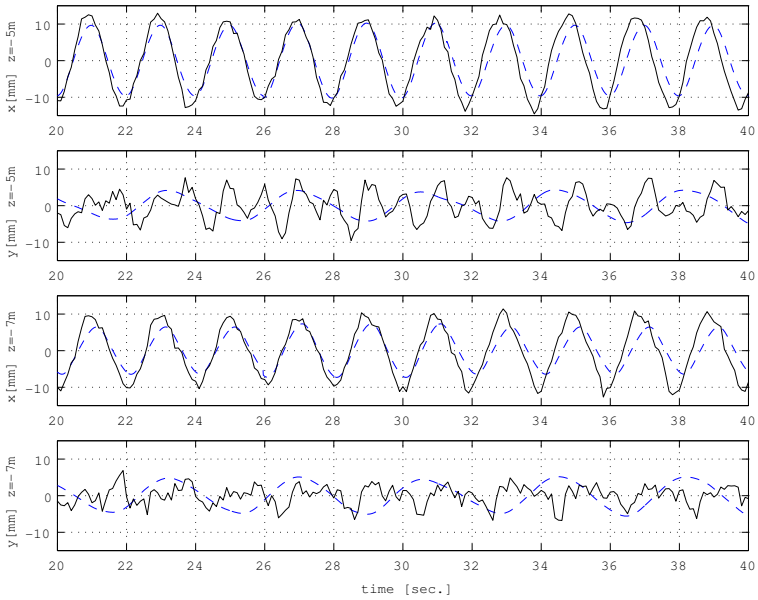

Figure 3.18: Time History Response Case 1 at z = -5 m and -7 m ––Simulation -Experiment

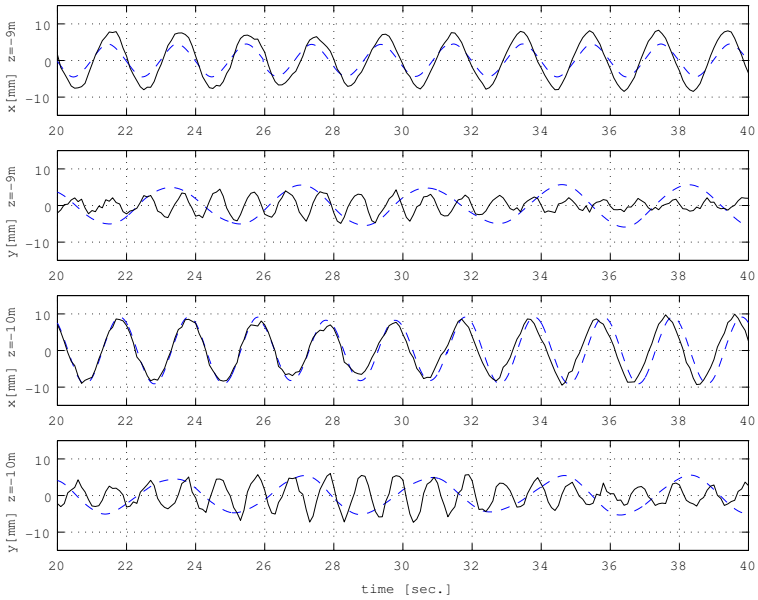

Figure 3.19: Time History Response Case 1 at z = -9 m and -10 m ––Simulation -Experiment

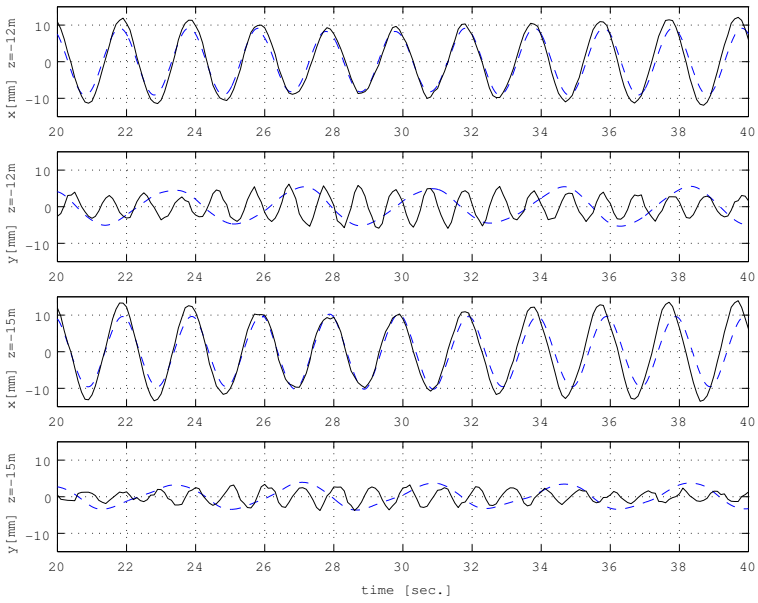

Figure 3.20: Time History Response Case 1 at z = -12 m and -15 m ––Simulation -Experiment

The in-line response is relatively well predicted in both amplitude and frequency content. It can be observed that although the experimental model is sinusoidally excited at its top end, the experimental data show that there is a variation in the amplitude involving a nonlinear phenomenon almost impossible to model using numerical simulation. It is also observed a variation in the frequency content. As previously mentioned, the *classical* lock-in condition is not considered in this section and although it is widely recognized that the Strouhal law is not followed and the frequency of the motion in the cross-flow direction does not coincide with the shedding frequency during synchronization events, it can be seen from the experimental data that the cross-flow frequencies significantly deviate from the cross-flow frequencies of the simulated time series responses. The CFD analysis previously presented showed that there exist two dominant frequencies for the model tested in the inertia regime. Nevertheless, the shedding frequency is proportional to the in-line velocity at a given section and therefore is expected that at low KC numbers the cross-flow frequency decreases. According to the Strouhal law, the experimental model presented in this section achieves a maximum value of f_S of approximately 0.4 Hz. It is clear that there are significant deviations in the cross-flow frequencies. However, these deviations can be partially explained by the unpredicted nature of the phase angle in the cross-flow direction. The phase angle is related to the energy transfer from the fluid to the body. According to Morse & Williamson (2006), for very low-mass damping, the energy dissipated is very low, and thus the phase is close to 0° or close to 180°. It seems that a more powerful scheme using an appropriate model for the calculation of the phase angle can somehow account for this deviation. The main difficulty is that the development of such model involves challenges such as the exact location of a jump in the phase angle for a specific reduced velocity.

The accurate prediction of the cross-flow response in flexible risers is still challenging due to its highly nonlinear nature. In addition, the assumption that only one frequency dominates the cross-flow response may introduce considerable deviations in its numerical calculation. Using the experimental data at z=-5 m and z=-15 m, it is possible to observe that the KC numbers achieved by the sections of the riser in these regions have similar values, as shown in Figs. 3.18 and 3.20. The values of the KC numbers obtained from the numerical simulation

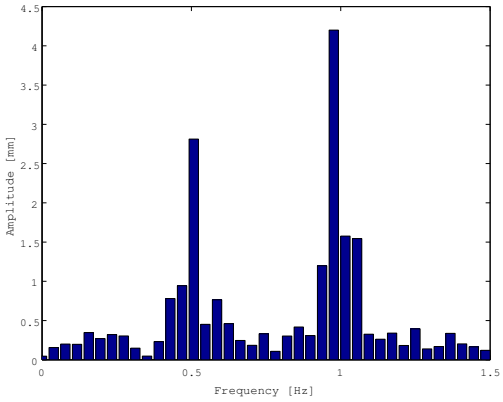

Figure 3.21: Fourier Spectrum Case 1 Cross-Flow at z = -5 m

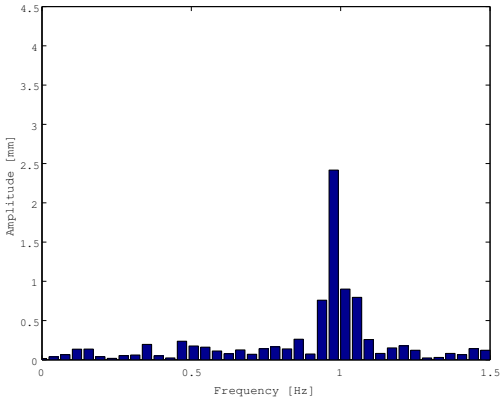

Figure 3.22: Fourier Spectrum Case 1 Cross-Flow at z = -15 m

at z=-5 m and z=-15 m are 4.55 and 4.39, respectively. However, the transverse response at z=-5 m is considerable different to the one achieved at z=-15 m, as shown in Figs. 3.21 and 3.22. When Fourier analysis of the experimental data in the cross-flow direction at z=-5 m and z=-15 m is carried out, the differences become more evident in both amplitude and frequency content as shown in Figs. 3.21 and 3.22. Furthermore, there is no clear distinction of the f_L that must be used at z=-5 m.

A CFD-based approach for response prediction of oscillating flexible risers at low values of β parameter was presented. Experimental data obtained from a 20-meter riser model, sinusoidally excited at its top end with amplitude of 0.01 m and period of 2 sec., were used to validate the proposed response prediction model. The selection of the amplitude of the force oscillation was based on the fact that the quasi-steady assumption is still valid at low amplitudes. The clear definition of the range in which quasi-steady models can be used to predict the dynamic response of oscillating flexible risers is still a topic of active research. Therefore, a CFD-based model was developed in this section in order to compute hydrodynamic force coefficients using oscillatory flow. The simulation results were then compared with experimental data and simulation results collected from previous studies performed for steady and oscillatory flows. Good agreement was observed in these comparisons. The CFD-based model was then used to model the case of an oscillating cylinder. The main idea of this procedure is to develop a model

completely independent of the quasi-steady assumption allowing fluid-structure interaction to be considered in the CFD-derived hydrodynamic force coefficients. At low amplitudes it is expected good agreement between the simulation results obtained from the oscillatory flow case and the oscillating body case. Therefore, the validation of the proposed CFD-based model for oscillating cylinders is carried out using the simulation results obtained from the oscillatory flow case. Good agreement was observed in the computed drag coefficients and a tendency of the oscillatory flow case to over-predict inertia coefficients when those coefficients are used to predict hydrodynamic forces on an oscillating cylinder highlighting the importance of considering fluid-structure interaction. Finally, maximum amplitudes in both in-line and cross-flow directions for the experimental and simulation results are presented in Table 3.5.

Table 3.5: Maximum Amplitudes Case 1

Depth(m)	In-line(exp)	In-line(sim)	Cross-flow(exp)	Cross-flow(num)
5.0	12.93	10.23	7.63	4.34
7.0	11.39	7.31	6.85	5.16
9.0	8.24	4.51	4.45	5.68
10.0	9.89	9.13	6.00	5.55
12.0	12.00	9.10	6.15	5.54
15.0	13.93	10.26	3.35	3.91

3.3.4 Inertia/Drag Regime

The experimental validation of the proposed prediction model is conducted at 4 different regimes based on the classification provided by Obasaju *et al.* (1988). As shown in Table 3.3, the amplitudes and periods of the harmonic excitation force provide experimental validation on a wide range. In addition, the region around KC=10 where there exist a large variation in the values of hydrodynamic force coefficients is included in this study.

In-line and cross-flow responses are computed at depths of 5 m, 7.5 m, 9 m, 10 m, 12.5 m and 15m for cases 2, 3, 4 and 5 according to Table 3.3. Figs.

3.23, 3.24 and 3.25 show the time history response of the riser during 14 sec. for case 2, Figs. 3.26, 3.27 and 3.28 for case 3, Figs. 3.29, 3.30 and 3.31 for case 4 and Figs. 3.32, 3.33 and 3.34 for case 5. It can be observed that the proposed model predicts in-line response relatively well in both amplitude and frequency content. It is also possible to observe some differences in amplitude response for cases 2 and 3. Especially, those regions of the riser excited at KC values close to 10. As previously explained, there is a large variation in both drag and added-mass coefficients in this region. It can partially explain these differences. In-line response in other regions is well predicted by the proposed model. It is also important to highlight that inertial force affects more significantly the dynamic response of the riser at low KC values. Therefore, the different values of β parameter used in the experimental data provided by Obasaju *et al.* (1988) and the riser model may cause some deviations in the response prediction. On the other hand, it is observed that in cases 4 and 5, which correspond to larger KC values, in-line amplitudes are well predicted. Due to the fact that in the diagonal and third vortex regimes drag forces are more dominant. Finally, an inflection point may also have some implications in the response prediction model due to a variation of in-line amplitudes. The experimental data for case 2 show the location of an inflection point around z=-10 m. Finally, it is also possible to observe some variations in in-line amplitude due to nonlinear effects that cannot be accounted by numerical simulation.

Although cross-flow response prediction shows some differences in frequency content, its amplitude is relatively well predicted. It is important to note that outside synchronization regions the force experienced by the riser will contain both the Strouhal and body oscillations [Sarpkaya (2004)]. On the other hand, synchronization causes the matching of the vortex shedding and oscillation frequencies leading to *an increase in the spanwise correlation of the vortex shedding and a substantial amplification of the cylinder's vibrational response* [Willden & Graham (2006)]. Another important factor to be considered is the low mass-damping parameter of the riser model presented in this section. According to Willden & Graham (2006), at low values of mass ratio, the fluid is dominant over the structure leading to a joint response dominated by the fluid and therefore their joint response frequency (riser and its surrounding fluid) will be controlled by the

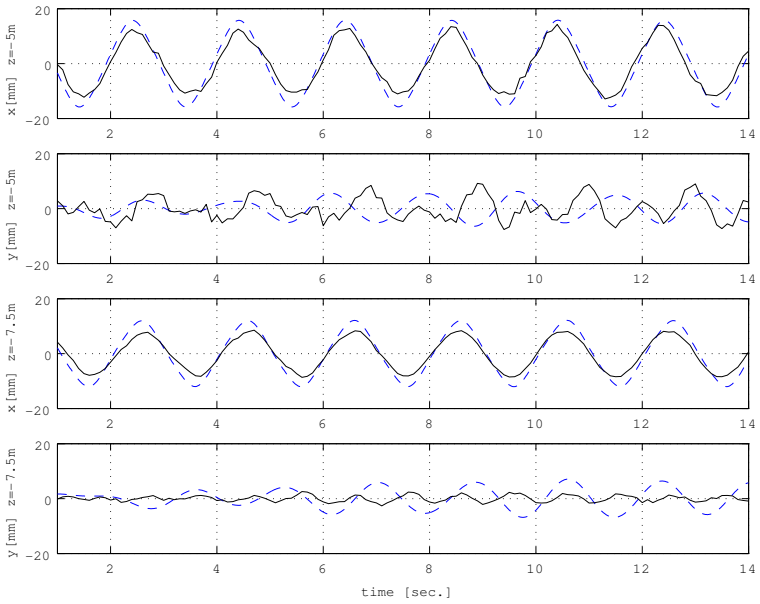

Figure 3.23: Time History Response Case 2 at z = -5 m and -7.5 m ––Simulation -Experiment

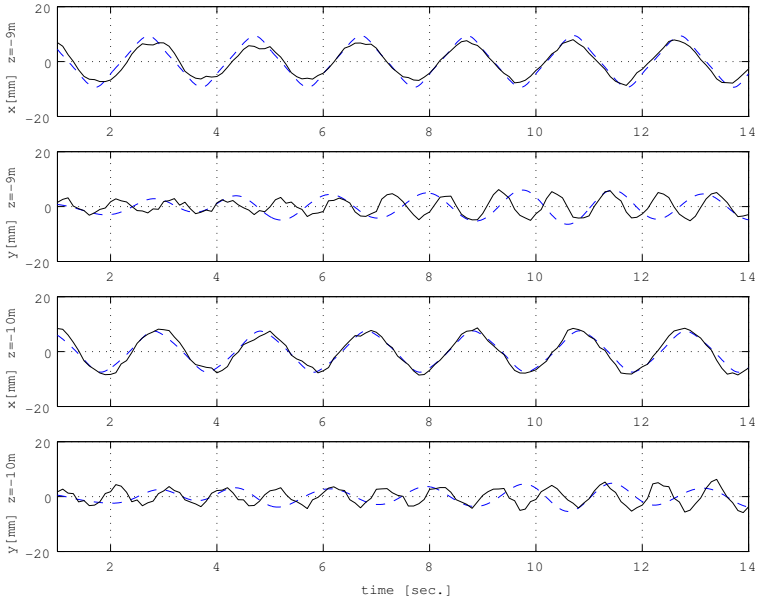

Figure 3.24: Time History Response Case 2 at z = -9 m and -10 m ––Simulation -Experiment

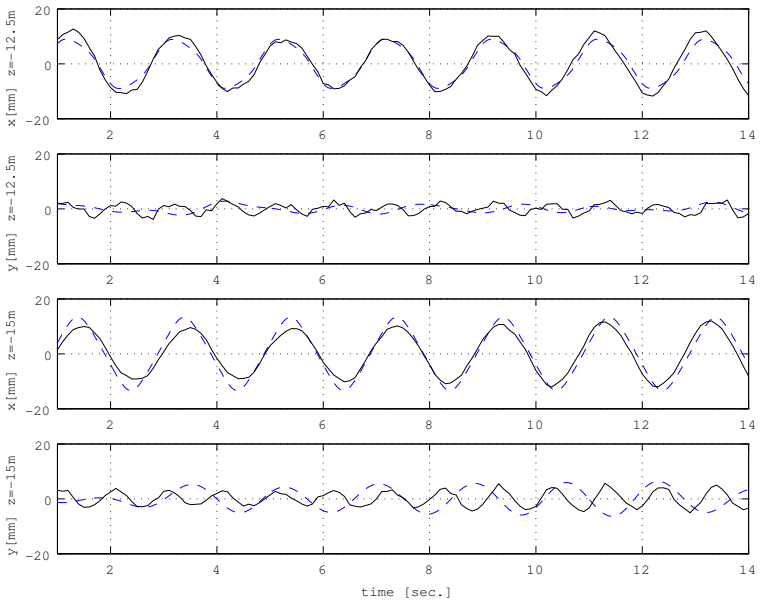

Figure 3.25: Time History Response Case 2 at z = -12.5 m and -15 m ––Simulation -Experiment

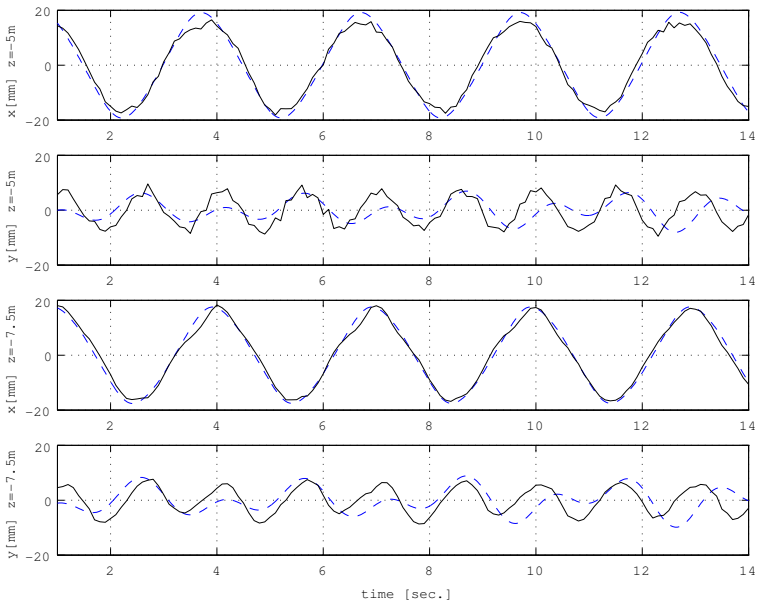

Figure 3.26: Time History Response Case 3 at z = -5 m and -7.5 m ––Simulation -Experiment

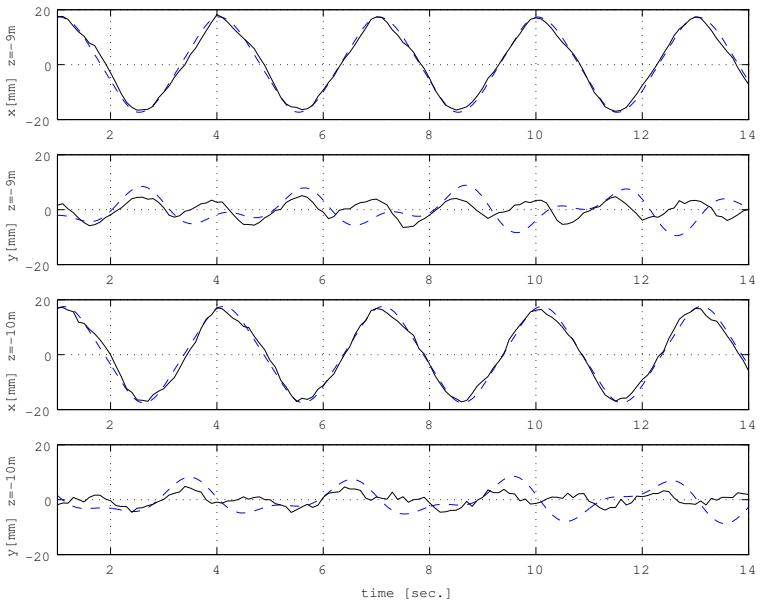

Figure 3.27: Time History Response Case 3 at z = -9 m and -10 m ––Simulation -Experiment

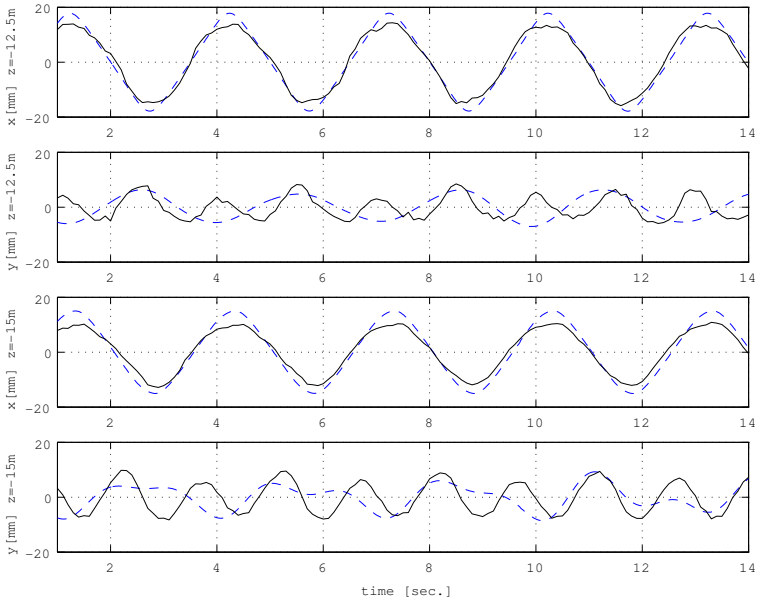

Figure 3.28: Time History Response Case 3 at z = -12.5 m and -15 m ––Simulation -Experiment

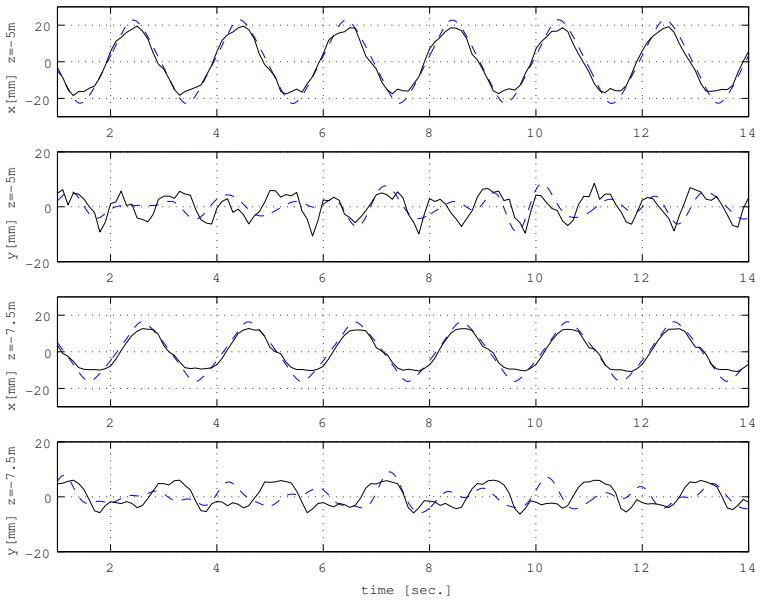

Figure 3.29: Time History Response Case 4 at z = -5 m and -7.5 m ––Simulation -Experiment

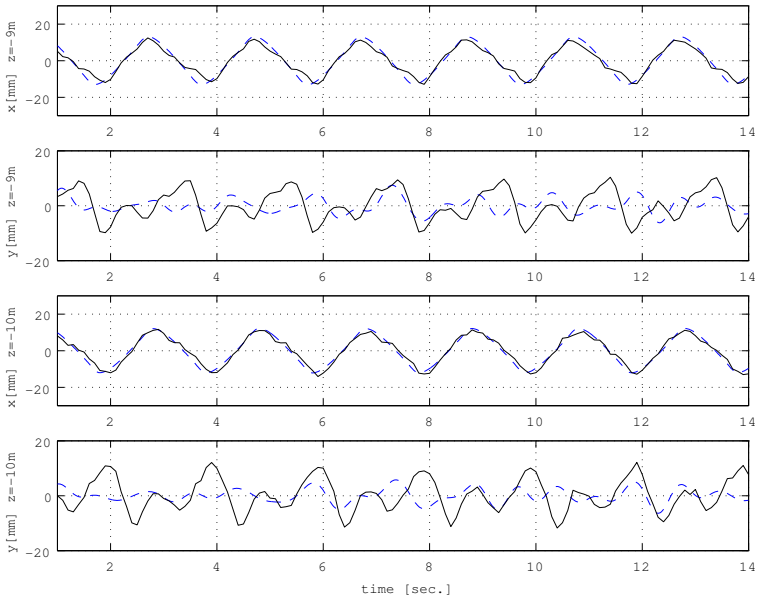

Figure 3.30: Time History Response Case 4 at z = -9 m and -10 m ––Simulation -Experiment

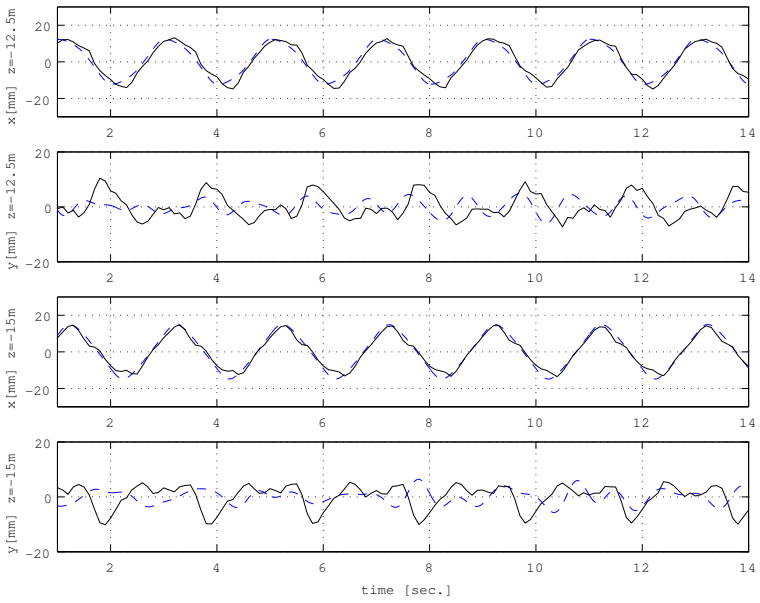

Figure 3.31: Time History Response Case 4 at z = -12.5 m and -15 m ––Simulation -Experiment

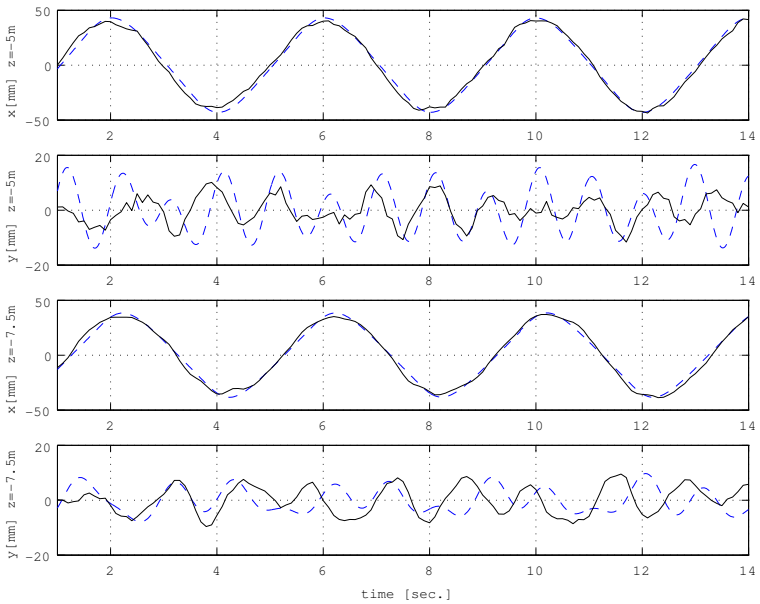

Figure 3.32: Time History Response Case 5 at z = -5 m and -7.5 m ––Simulation -Experiment

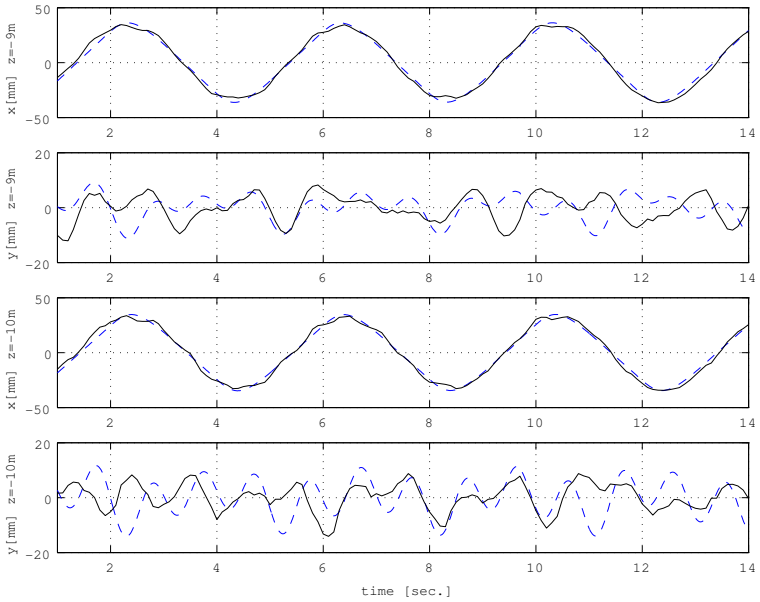

Figure 3.33: Time History Response Case 5 at z = -9 m and -10 m ––Simulation -Experiment

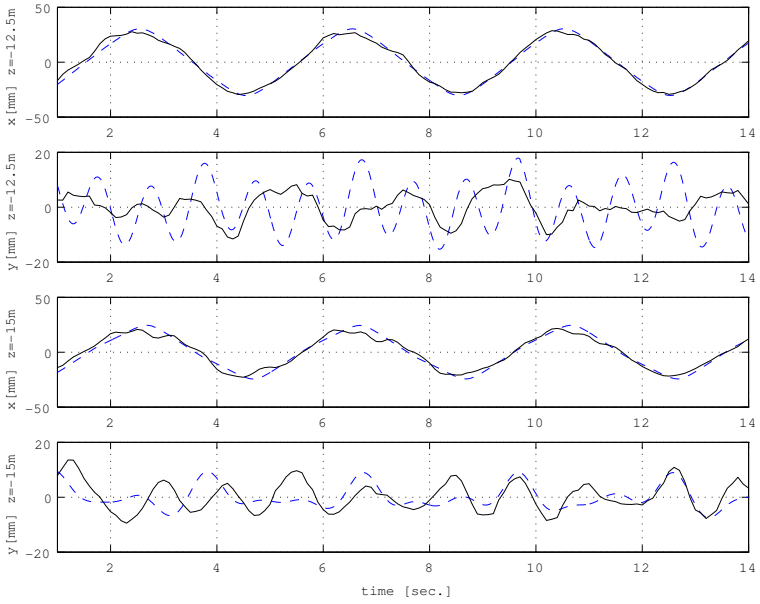

Figure 3.34: Time History Response Case 5 at z = -12.5 m and -15 m ––Simulation -Experiment

Strouhal frequency. Actually, the accurate prediction of the cross-flow response in flexible risers is still challenging due to its highly nonlinear nature. In addition, the assumption that only one frequency dominates the cross-flow response may introduce considerable deviations in its numerical calculation. Finally, for low mass-damping, a small variation of the phase angle can cause the system to change from positive to negative excitation [Morse & Williamson (2006)].

The range of experimental validation provided in this section considers the asymmetric, transverse, diagonal and third vortex regimes. Good agreement in amplitude response was found for both in-line and cross-flow displacements. Some differences were found in the predicted response in the in-line direction for the model tested in the asymmetric and transverse regimes. This is partially caused by the large variation of the hydrodynamic force coefficients in these regions that cannot be accurately accounted by the proposed prediction model. In the transverse, diagonal and vortex regimes, the proposed model accurately predicts in-line response. Finally, maximum amplitudes in both in-line and cross-flow directions for the experimental and simulation results are presented in Tables 3.6, 3.7, 3.8 and 3.9.

Table 3.6: Maximum Amplitudes Case 2

Depth(m)	In-line(exp)	In-line(sim)	Cross-flow(exp)	Cross-flow(num)
5.0	14.26	15.78	9.19	6.25
7.5	8.52	12.10	2.58	7.08
9.0	7.96	9.42	6.16	5.99
10.0	8.60	7.59	6.27	4.84
12.5	12.69	8.97	3.76	2.78
15.0	12.01	13.35	5.66	6.33

3.3.5 Drag Regime

In-line and cross-flow responses are computed at depths of 3.5 m, 6.5 m, 9 m, 12 m, 14.5 m and 17 m. Figs. 3.35, 3.36 and 3.37 show the time history response of the riser during 14 sec. In-line response in both amplitude and frequency content

Table 3.7: Maximum Amplitudes Case 3

Depth(m)	In-line(exp)	In-line(sim)	Cross-flow(exp)	Cross-flow(num)
5.0	16.51	19.23	9.57	6.94
7.5	18.27	17.58	7.63	8.82
9.0	18.19	17.36	5.12	8.87
10.0	17.17	17.54	4.81	8.46
12.5	14.33	17.83	8.47	6.33
15.0	10.89	15.04	9.78	9.24

Table 3.8: Maximum Amplitudes Case 4

Depth(m)	In-line(exp)	In-line(sim)	Cross-flow(exp)	Cross-flow(num)
5.0	19.46	22.91	8.54	8.39
7.5	12.70	16.37	6.05	9.03
9.0	12.40	13.18	10.36	7.44
10.0	11.63	12.20	12.12	5.76
12.5	13.10	12.33	10.39	4.91
15.0	14.80	14.97	5.51	6.39

is well predicted. The response prediction model correctly accounts for drag force amplification during synchronization events. On the other hand, although experimental data show some nonlinearities in the in-line response, the simulation results follow the main trend of the riser's response.

Cross-flow response is also relatively well predicted for the cases presented in Figs. 3.35, 3.36 and 3.37. It can be observed that the sinusoidal approximation widely used to describe the cross-flow response based on the dominant frequency is not applicable for practical applications. Even though transverse force is calculated based on Eq. (3.6), the experimental data show large fluid-structure interaction leading to non-sinusoidal cross flow response as shown in Figs. 3.35, 3.36 and 3.37. As previously mentioned, the initial riser's response is unsteady due to time varying load. Therefore, when comparisons between experimental data and simulation results were conducted, it was necessary to modify in-line phase angles in order to improve the quality of the graphical results presented in

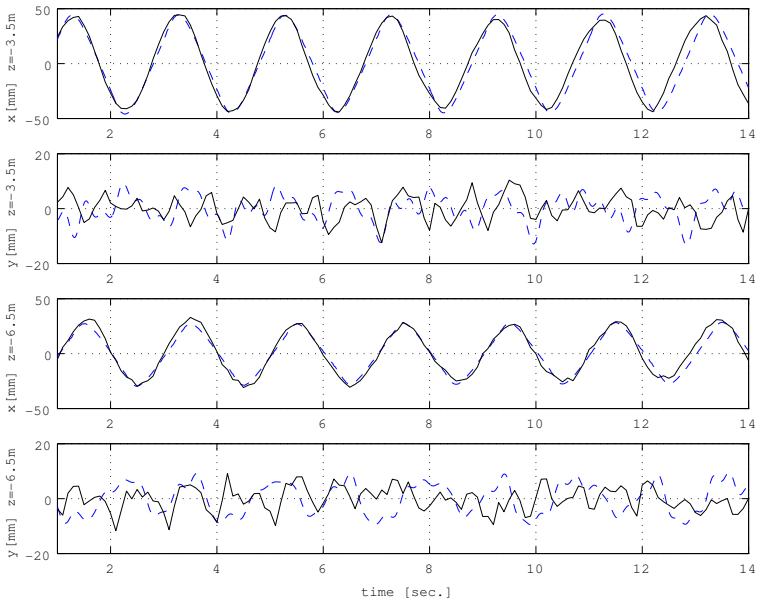

Figure 3.35: Time History Response Case 6 at z = -3.5 m and -6.5 m ––Simulation -Experiment

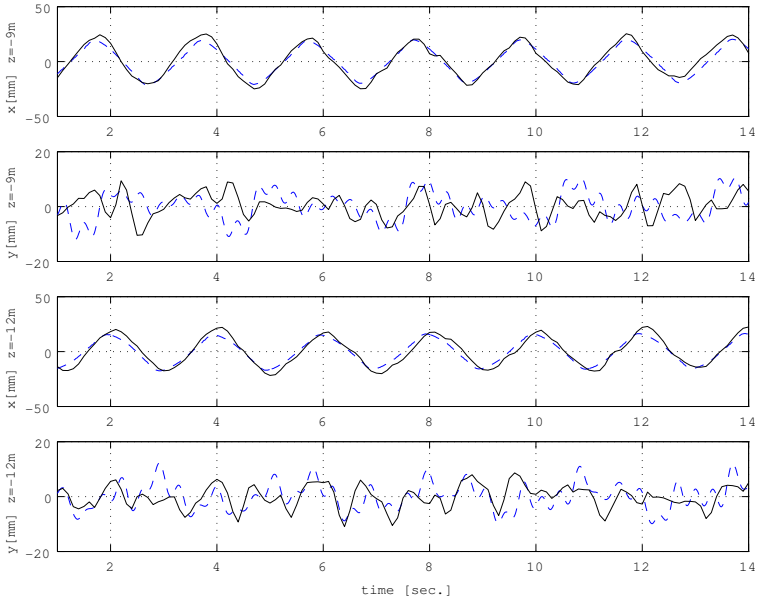

Figure 3.36: Time History Response Case 6 at z = -9 m and -12 m ––Simulation -Experiment

Table 3.9: Maximum Amplitudes Case 5

Depth(m)	In-line(exp)	In-line(sim)	Cross-flow(exp)	Cross-flow(num)
5.0	42.05	43.05	10.12	16.64
7.5	37.08	38.45	9.49	9.69
9.0	34.55	36.25	8.22	9.09
10.0	33.65	34.74	8.77	11.66
12.5	28.59	30.44	10.16	17.84
15.0	21.62	24.45	13.56	9.32

Figs. 3.35, 3.36 and 3.37.

According to Blevins (1990), the dominant frequency in the quasi-steady regime can be approximately calculated as 6 times the value of its corresponding in-line frequency. However, the experimental data show high variation in both amplitude and frequency content in the cross-flow response. Based on the aforementioned, the response prediction model accounts for the main features of the riser response and achieves good agreement in both amplitude and frequency content. This is basically a current limitation in the theory related to main factors that influence the response of oscillating flexible risers. Finally, maximum amplitudes in both in-line and cross-flow directions for the experimental and simulation results are presented in Table 3.10.

Table 3.10: Maximum Amplitudes Case 6

Depth(m)	In-line(exp)	In-line(sim)	Cross-flow(exp)	Cross-flow(num)
3.5	44.33	45.03	10.37	9.19
6.5	32.88	28.45	9.13	9.45
9.0	25.33	20.21	9.37	10.39
12.0	22.82	16.36	8.63	12.26
14.5	24.10	16.48	6.64	9.81
17.0	15.82	12.92	10.32	9.51

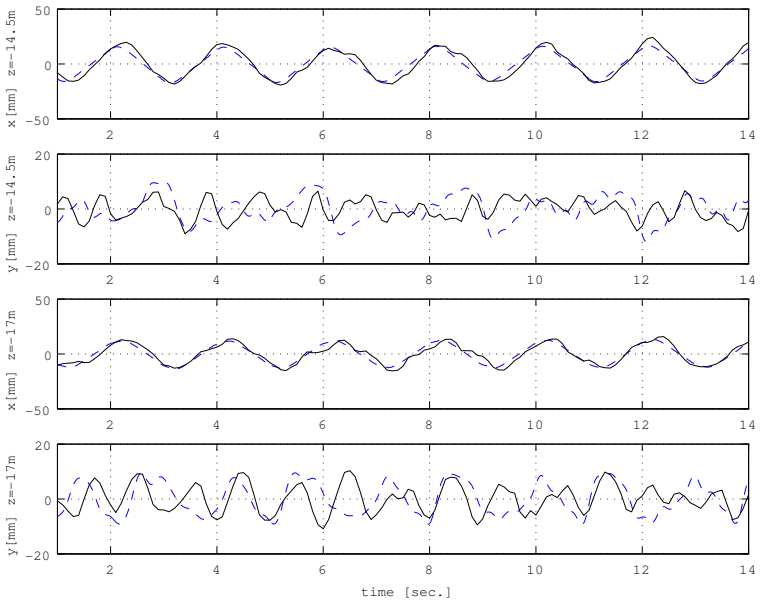

Figure 3.37: Time History Response Case 6 at z = -14.5 m and -17 m ––Simulation -Experiment

3.4 Response Prediction Model for Hanging Flexible Risers

3.4.1 Experimental Model

In this section a flexible riser hanging from its top end support is used to experimentally validate the proposed prediction model employing a 35-meter riser model. The experimental model presented in this section is sinusoidally excited at Re numbers up to 1900 and KC numbers up to 8. The riser's response is mainly located in the asymmetric region [Obasaju *et al.* (1988)]. According to Blevins (1990), in this region the dominant frequency is approximately twice the frequency of the oscillating frequency in the in-line direction ($f_S/f = 2$) as shown in Table 2.1. The main features of the experimental riser model are presented in Table 3.2. The only parameter that changes in Table 3.2 is the length of the riser model. This parameter changes from 20 m to 35 m.

The riser model has a fixed connection with the oscillator at its top end and

is excited along the x-axis is sinusoidally excited at its top end with amplitude of 0.02 m and periods ranging from 1.06 sec. to 1.56 sec. The oscillator and the top end of the riser move together as previously mentioned. Steel bars are added to the riser model in order to increase its self-weight. The total weight of the riser, including the steel bars, is 119.25 N. Fig. 3.38 depicts the details of the bottom support of the riser model. Two rigid connectors and two additional cable connectors are used to represent a fixed connection. In the simulation procedure it is assumed a gap of 2 mm in the negative direction of the z-axis in order to consider the gap between the lower support and connector B.

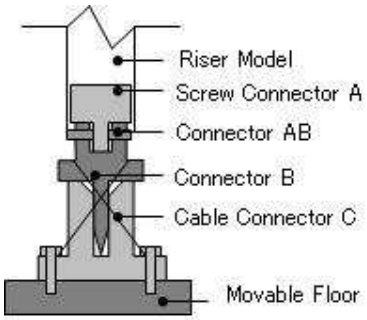

Figure 3.38: Bottom Connection of the 35-meter Riser Model

3.4.2 Numerical Implementation

The FE model of the 35-meter riser is assembled using 138 Euler-Bernoulli elements. Its self-weight is applied during the static step and hydrodynamic forces during the dynamic step as previously described. The model is fixed at its top end and the boundary condition at its bottom end, as shown in Fig. 3.38, is numerically represented by a system of linear springs, which constrain displacements and moments in x- and y-axis, an additional linear spring constrains the z-axis moment. A nonlinear spring is additionally used to allow vertical displacements up to a maximum of 2 mm in the downward direction; in the upward direction this nonlinear spring restrains axial displacements. The fixed boundary condition for this type of riser model, without tension forces acting at its top end, is selected herein due to the fact that the use of nonlinear springs in the z-axis partially

avoids the formation of gravity sag of the riser caused by a concentration of its self-weight in the vicinity of its bottom end.

The proposed prediction model first applies the drag forces during 25 cycles using a fix value of C_{Dmean} of 1.5. Then, at the end of the first stage, the in-lines amplitudes are calculated and used to update hydrodynamic coefficients based on KC values, at the same time the cross-flow forces are applied during 10 additional cycles. The lock-in condition in both in-line and cross-flow is included in the third stage when drag and lift coefficients are updated. This stage lasts 55 additional cycles. The computation of the in-line and cross-flow forces is carried out by the in-house FORTRAN subroutine and then input to the FE model of the riser at each time step.

3.4.3 Simulation Results

Figs. 3.39, 3.40 and 3.41 show the time history response of the riser during 20 seconds exited at a period of 1.06 sec. and Figs. 3.42, 3.43 and 3.44 at a period of 1.56 sec. In-line and transverse responses were computed at depths of 5 m, 10.5 m, 15 m, 20 m, 25 m and 27.5 m. The experimental data were passed through a 6th order high-pass Butterworth filter with a 0.1 Hz cutoff. The in-line phase angles were corrected in order to improve the quality of the graphical results. Large displacements at the bottom end may be less dominant in the real boundary condition. In addition, a local damping mechanism is likely to be acting at the bottom end and its numerical simulation may involve a highly nonlinear behavior. Although nonlinear springs are used to avoid gravity sag at the bottom end due to the riser's self-weight, it is impossible to completely eliminate this effect during the simulation.

It can be seen from Figs. 3.39 and 3.40 that the in-line force magnitude is over-predicted. This tendency is also observed in Figs. 3.42 and 3.43. As previously mentioned, Lin *et al.* (1996) identified the existence of a region located around KC=8 where there is a rapid rise of C_{Dmean} and decrease of C_m. C_{Dmean} rises approximately from 1.6 at KC=7 to 2.0 at KC=8. This phenomenon can partially explain the over-prediction of the drag forces; because the sections located near the top of the riser have values of KC numbers close to 8. In addition, an

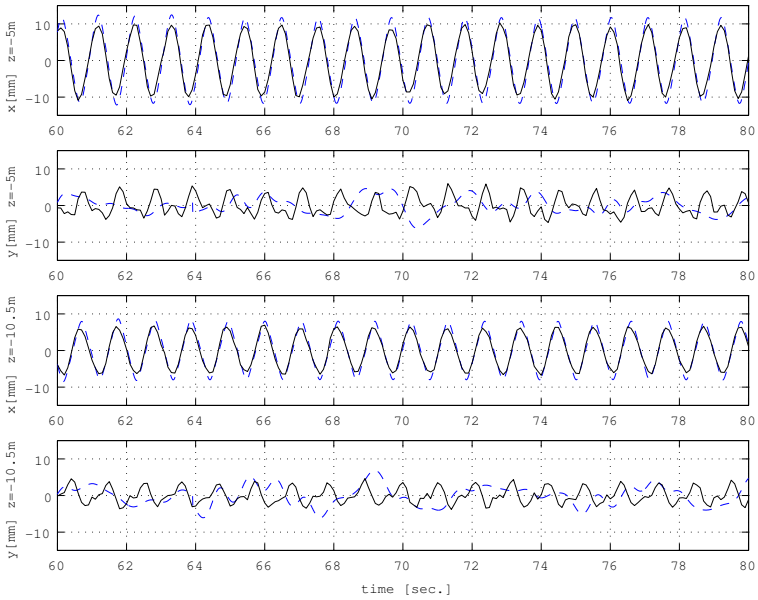

Figure 3.39: Time History Response 35-meter Riser Model (T=1.06 sec.) at $z =$ -5 m and -10.5 m ––Simulation -Experiment

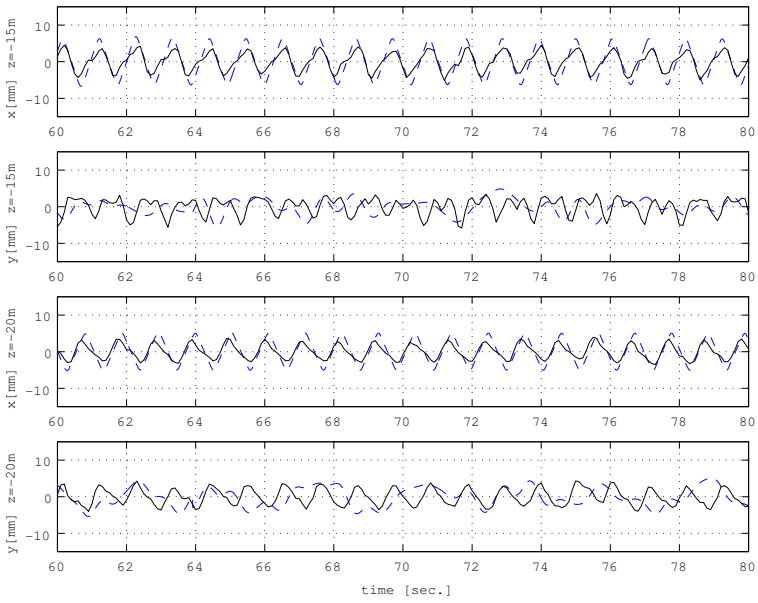

Figure 3.40: Time History Response 35-meter Riser Model (T=1.06 sec.) at $z =$ -15 m and -20 m ––Simulation -Experiment

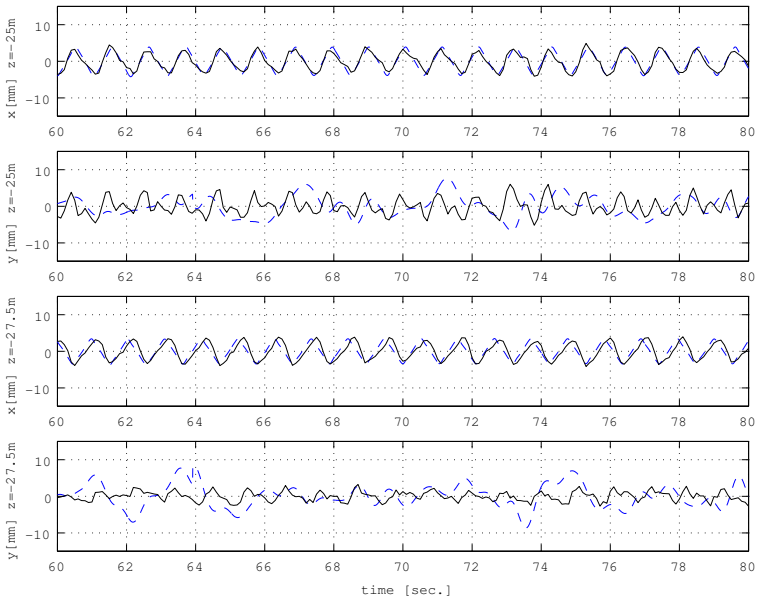

Figure 3.41: Time History Response 35-meter Riser Model (T=1.06 sec.) at $z =$ 25 m and -27.5 m ––Simulation -Experiment

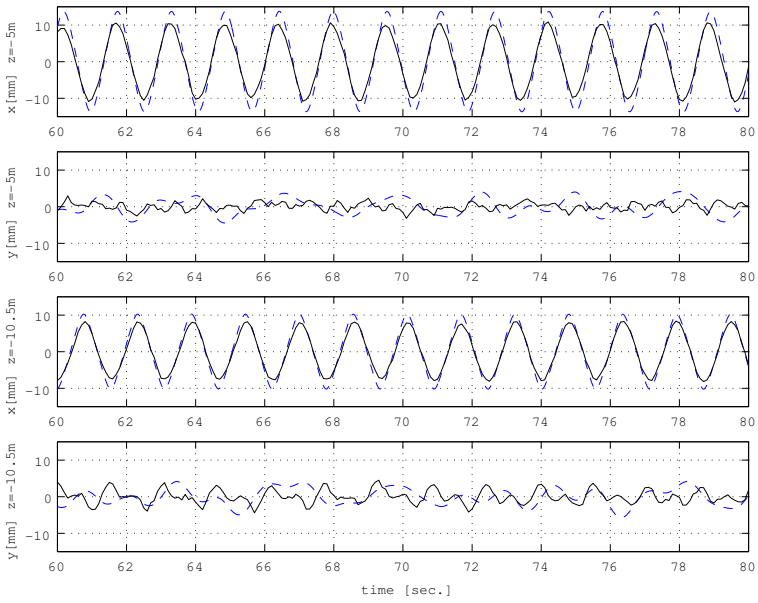

Figure 3.42: Time History Response 35-meter Riser Model (T=1.56 sec.) at $z =$ -5 m and -10.5 m ––Simulation -Experiment

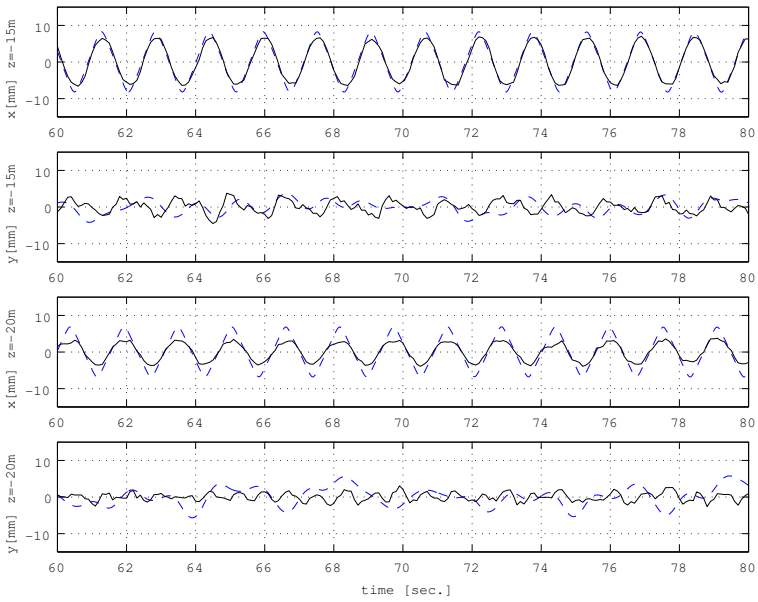

Figure 3.43: Time History Response 35-meter Riser Model (T=1.56 sec.) at $z =$ -15 m and -20 m ––Simulation -Experiment

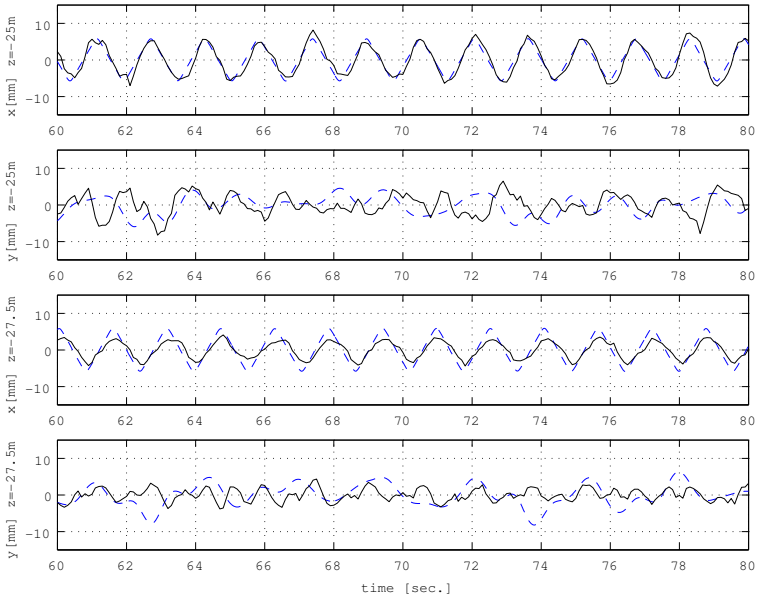

Figure 3.44: Time History Response 35-meter Riser Model (T=1.56 sec.) at $z =$ 25 m and -27.5 m ––Simulation -Experiment

error in the calculation of C_m is included in the simulation due to fluid-structure interaction neglect.

The period of excitation (T=1.06 seconds) induces a dynamic response having 36 elements of the FE model moving under lock-in considerations. On the other hand, when the period of excitation is increased to T=1.56 seconds, the number of FE elements under lock-in considerations is 62. When the number of sections under lock-in considerations is increased, the simulation results deviate from the experimental data. Lock-in affects both in-line and cross-flow response. Therefore, the quality of the transverse response prediction is relatively better for the low-period case. On the other hand, for the high-period case, there are significant differences in both in-line and cross-flow responses.

The in-line response is well represented by the proposed response model. There is a large region of the riser model located in the asymmetric region (mid section of the riser), where the lock-in condition is not achieved. In this region C_{Dmean} is approximately 1.5 according to Lin *et al.* (1996). Large amplitudes are observed for sections near the bottom end of the riser for the two cases presented in this section. If the magnitude of the displacements achieved by the riser model is taken into account, even a small displacement in the fixed connection can lead to a significant reduction in the cross-flow amplitudes. In addition, during the dynamic step due to the inherently nonlinear nature of the riser model it is possible to have additional vertical displacements that are not included in the initial deformed shape of the riser. In addition, a highly damping mechanism is likely to be acting at the bottom end of the riser.

3.4.4 Concluding Remarks

Some differences are found in the in-line amplitude response for the sections of the riser located near the upper end and it is assumed to be partially caused by underestimation of the drag coefficients or fluid-structure interaction neglect. The amplitude of the cross-flow response is relatively well predicted by the proposed response model. It was found that the numerical model of the boundary condition at the bottom end caused some errors in the dynamic response of the riser in regions located near the bottom end of the riser. The accurate modeling of a

boundary condition is still one of the major challenges in the structural mechanics field. In this section a system of linear and nonlinear springs was used to model the boundary at the bottom end. New modeling strategies must be considered in order to improve the quality of the dynamic response of the riser near the bottom end. The long flexible model due to its complex nonlinear behavior involves many challenges; the proposed prediction model using a numerical representation of the increased drag coefficient was able to represent the main features of the dynamic response of the riser model. An important issue to be considered in order to improve the response model presented in this section is the correct calculation of the hydrodynamic coefficients in the asymmetric region for this particular study. Although the values of these coefficients were taken from the best research work in that field, there are some modeling considerations that must be included in the numerical scheme, especially the segment of the 35-meter riser model located in the lock-out region. The main challenge is that the response from one region can dominate the total response of a flexible riser by disrupting the excitation process in other regions.

Chapter 4

Damage Assessment of Flexible Risers

The oil production industry is gradually moving into deeper waters demanding accurate and reliable damage detection tools for offshore structures. One of the most important structural components needed for oil extraction in deep waters is the riser system. Therefore, flexible risers are currently receiving considerable attention by the research community due to its complex dynamic response and its economical impact when large structural degradation mainly caused by Vortex-Induced Vibrations (VIV) affects its structural integrity.

Valdes & Ortega-Ramirez (2000) cited the case of inspection of marine facilities installed in the Gulf of Mexico, which are inspected thoroughly every five years. Long-term inspection program consists on five short-term programs (annual); during these, 20% of the long-term program must be covered. It was stressed that at the end of each short-term program, results must be analyzed in order to define possible modifications in subsequent inspection programs. They recommended the establishment of permanent monitoring systems of the meteorological, oceanographical, and seismc conditions and record systems of the structural response due to waves and earthquakes. According to Ohtsubo & Sumi (2000), monitoring, inspection, maintenance and repair of deep water risers are very costly activities. Advanced Systems and special equipment must be developed to reduce the cost and enhance the reliability of riser systems. Moreover,

difficulties may be encountered when marine growth becomes too thick. Therefore, the associated cost with the use of remotely operated vehicles equipped with video cameras and other instruments, widely used for visual inspection in deep water, become prohibited. On the other hand, autonomous underwater vehicles offer an attractive alternative to conventional pipeline inspection methods. However, no actual performance information is presently available in the open literature for such kind of vehicles.

An unhealthy marine structure is not reliable and demands more frequent inspection. In addition, during extraordinary events (hurricanes, conflagrations, accidents, etc.) an unhealthy marine structure is prone to collapse. Current inspection techniques for marine structures are either visual or local experimental methods such as ultrasonic or acoustic methods, magnetic field methods, radiographs, eddy current methods and thermal field methods. The major drawbacks of these local experimental methods are that the location of damage must be known a *priori* and that there is a relatively high level of dependency on the practical skills of the engineers who carry out structural inspections. Visual inspection methods might not be the best solution for marine structures when the accessibility conditions represent potential danger to the inspectors.

4.1 Vibration-Based Damage Detection

Inman *et al.* (2005) pointed out the importance of damage diagnosis among the engineering community. In addition, there are great economic incentives motivating this topic's development. Damage identification is an inverse problem, so, it is in principle an unsolvable problem. This type of problem is well know in the mathematical community. Therefore, according to Inman *et al.* (2005), the challenge is to define some methods better adapted to predicting structural damage. On the other hand, recent advances in sensing technology are making possible the use of sensing systems to assess the current health state of civil structures; the main idea behind this approach is that measured modal parameters can be used to detect structural damage.

According to Rytter (1993), a robust vibration-based damage detection system is divided into four levels: identification of damage that has occurred at a very

early stage (Level I), localization of damage (Level II), quantification of damage (Level III) and prediction of the remaining useful life of the structure (Level IV). Although damage monitoring of civil structures has generated a lot of research over the past years, there is still a debate whether the measured deviations are significant enough to be a good indicator of structural degradation. It is widely recognized from sensitivity studies using FE models and from *in-situ* tests of artificially damaged structures that the decrease of frequencies is often relatively low. Furthermore, although the local stiffness drop at a local damage site may be high, the global stiffness results in relatively small frequency changes, which can only be detected with precise measurement and identification procedures.

Vibration-based damage detection methods, which are able to locate and quantify structural damage, are based on the premise that the mass of a structure does not change appreciably as a result of structural damage. This assumption may not be true for offshore structures due to variation of structural mass or marine growth, which can cause uncertainty in the measured modal parameters. In addition, when an offshore structure is used to support tanks, the fluid in tanks can also vary its mass. Many studies have been conducted in this area showing that damage-induced frequency shifts are difficult to distinguish from shifts resulting from increased mass. Furthermore, structural damage usually causes changes in the order of the mode shapes; highlighting the importance of identifying a mode shape as well as its corresponding resonant frequency to accurately track its changes, which is not easy considering the adverse marine conditions commonly affecting offshore structures. An innovative approach to assess the current health state of a structure is the statistical analysis of its measured vibration data. This approach offers several advantages over existing modal-based damage detection methods. Modeling errors and modal identification limitations are avoided in this approach making it more attractive and affordable for the development of a vibration-based damage detection framework for flexible risers.

4.1.1 Modal-Based Damage Detection Approach

There are essentially two types of vibration test. The first one is defined as ambient vibration test, where the responses are measured under normal operation of

the structure. The second is defined as force vibration test, where the structure is excited with a known input. Note that although the excitation is unknown for an ambient test, the ambient vibration test is more suitable for continuous health monitoring. In addition, to obtain the correct scaling of the mode shapes, the applied force has to be known and for very large structures or structures affected by a combination of several ambient loads, it becomes very difficult to apply sufficient artificial excitation to surpass the vibration levels from the ambient excitation which is always present. Therefore, if the purpose of the test is continuous monitoring only ambient excitation can be used.

The modal-based damage detection approach proposed in this section consists of three steps; in the first step, ambient excitation sources are employed to extract the free response behavior of a riser (impulse response synthesis from ambient measurements). Once time domain impulse response functions are obtained, The Eigensystem Realization Algorithm (ERA) is employed for identifying the modal parameters. In ERA, the Hankel matrix is formed using the response vector obtained from synthesized free-response, this step is defined as system identification. Finally, by comparing the obtained modal parameters of the healthy and damaged states of the riser, a deterministic damage detection algorithm locates damaged sites. These methods are described in the following sections.

4.1.1.1 Impulse Response Synthesis from Ambient Measurements

Farrar & James (1997) found that if an unknown excitation is a white-noise random process, the cross-correlation function between two response measurements would have the same form as the free response of the structure. This method is known as the Natural Excitation Technique (NExT) and it is very important due to physical limitations to calculate the magnitude of the exciting forces during an ambient excitation test. This statement, therefore, allows us to use fluid forces to excite a flexible riser and obtain its free response.

4.1.1.2 System Identification

The use of accurate modal information for system identification will lead to reliable damage detection results. The most commonly used system identification

methods are the extended Kalman filters [Toshiba & Saito (1984)], the polyreference time domain method [Zhang *et al.* (1985)], the multivariate Auto-Regressive and Moving Average (ARMA) model [Phan *et al.* (1990)], the Q-Markov cover algorithm [Lin & Skeleton (1993)], and the Eigensystem Realization Algorithm (ERA) [Juang & Pappa (1985)]. In this section, ERA is selected for system identification. This algorithm has been successfully used during the last two decades for several researchers showing good performance due to its ability to handle measurement data corrupted by noise and indicators that allow quantification of the obtained modal parameters.

The ERA was originally developed to identify a state space representation of a system from frequency response functions. The use of ERA with free response data is presented indicating that the state space matrices can be obtained from free response records. Modal parameters of a structure can be identified from these two matrices as explained in the following paragraphs. The mathematical formulation of the ERA uses the Hankel matrix, which is formed using the response vector obtained from synthesized free-response. The generalized Hankel matrix consisting of Markov's parameters is constructed as shown in Eq. (4.1).

$$[H\,(k-1)] = \begin{bmatrix} [Y\,(k)] & \cdots & [Y\,(k+s-1)] \\ [Y\,(k+1)] & \cdots & [Y\,(k+s)] \\ \vdots & \ddots & \vdots \\ [Y\,(k+r-1)] & \cdots & [Y\,(k+r+s-2)] \end{bmatrix} \tag{4.1}$$

where $\mathbf{[Y(k)]}$ is the Markov's parameter obtained from structural impulse response at kth time step. The number of columns and rows are represented by r and s, respectively. The Hankel matrix is then evaluated for the $\mathbf{[H(0)]}$, and a singular value decomposition technique is performed as shown in Eq. (4.2).

$$[H\,(0)] = [P]\left[\backslash C\backslash\right][Q]^T \tag{4.2}$$

The diagonal matrix $\left[\backslash C\backslash\right]$ contains singular values that correspond to structural modes. However, small singular values are likely to appear in the diagonal values of the matrix $\left[\backslash C\backslash\right]$. Therefore, this diagonal matrix is condensed in order to retain the largest N singular values and then minimize the effect of computational modes. The matrices $\mathbf{P}$ and $\mathbf{Q}$ are square and unitary. The matrices C_N,

P_N, and Q_N are obtained without considering computational modes. The basic ERA's theorem states that, if the dimension of any minimal realization is N, then the triplet shown in Eq. (4.3) is the minimum realization.

$$\begin{aligned} [R] &= [E_p]^T [P_N] [C_N]^{1/2} \\ [F] &= [D_N]^{-1/2} [P_N]^T [H(1)] [C_N]^{-1/2} \\ [G] &= [C_N]^{1/2} [Q_N]^T [E_q] \end{aligned} \tag{4.3}$$

where E_p is defined as $[\,[I]\,[0]\;\cdots\;[0]^T\,]$, and E_q is defined similarly. The unknown matrix $\mathbf{A}$ contains the eigenvalues and modal damping values of the structure and the matrix $\mathbf{R}$ is used for the transformation of the corrupted eigenvectors, in the state space matrix, to the physical states model.

4.1.1.3 Deterministic Damage Detection

The Damage Index (DI) method [Stubbs *et al.* (1995)] is adopted here for damage detection. This method has been extensively used in previous damage detection studies showing its best performance over other existing damage detection methods [Farrar & Jauregui (1996) and Barroso & Rodriguez (2004)]. The selection criteria for this method are based on previous research work that can be summarized as follows: Tang & Leu (1991) showed that changes in the mode shapes of the structure were more sensitive indicators of damage than natural frequencies. Pandey *et al.* (1991) demonstrated the use of changes in the curvature of the mode shapes to detect and locate damage. They also found that both the Modal Assurance Criterion (MAC) and the Coordinate Modal Assurance Criterion (COMAC) were not sensitive enough to detect damage in its earlier stages. Chance *et al.* (1994) found that measuring curvature directly using strain measurements gives very improved results than those of the curvature calculated from the displacements. Also, Chen & Swamidas (1994) found that strain mode shapes facilitated the location of a crack in a cantilever plate using finite element method simulation. Yam *et al.* (1996) have found that the strain mode shape is more sensitive to structural local changes than the displacement mode shape. Quan & Weiguo (1998) showed that for the steel deck of a bridge, the curvature mode shapes

are the best among three damage recognition indices based on mode shapes (the COMAC, the flexibility, and the curvature mode shape).

The DI method was developed by Stubbs *et al.* (1995) to detect the existence and location of damage in a structure and is based on the assumption that strain energy stored in damaged regions will decrease after the occurrence of damage. The damage index, γ_{ij}, is estimated by the change of the curvature of a particular mode shape, which is related to mode strain energy changes at location j. γ_{ij} is then defined in Eq. (4.4).

$$\gamma_{ij} = \frac{\left(\int_a^b [\ddot{\psi}_i^*(x)]^2 dx + \int_0^{L_e} [\ddot{\psi}_i^*(x)]^2 dx\right) \int_0^{L_e} [\ddot{\psi}_i(x)]^2 dx}{\left(\int_a^b [\ddot{\psi}_i(x)]^2 dx + \int_0^{L_e} [\ddot{\psi}_i(x)]^2 dx\right) \int_0^{L_e} [\ddot{\psi}_i^*(x)]^2 dx} \tag{4.4}$$

where $\ddot{\psi}_i$ and $\ddot{\psi}_i^*$ are the second derivatives of the ith mode shape before and after the occurrence of damage, respectively. L_e is the length of the beam element in which damage is being evaluated, and a and b are the limits of this beam element. It is important to clarify that it is assumed that the whole model is divided into several sections. Therefore, the limits previously defined correspond to each section. The damage index for the selected mode shapes is obtained by adding the individual contribution of the damage index of each of the selected mode shapes.

The damage index procedure can be summarized as follows: (1) calculate the mode shapes amplitudes for the nodes where sensors are located; (2) estimate the amplitudes of the mode shapes for the nodes where no sensors are located by interpolating the instrumented nodes using cubic-spline functions; and, (3) take a second derivative of the interpolation function at each node. Finally, treating γ_{ij} as a realization of a normally distributed random variable γ, a normalized damage index is computed as shown in Eq. (4.5).

$$Z_j = \frac{\gamma_j - \overline{\gamma}}{\sigma_\gamma} \tag{4.5}$$

where $\overline{\gamma}$ and σ_γ are the mean and standard deviation of the damage index, respectively. The jth substructure is defined as damaged when $Z_j > 2$, which corresponds to a hypothesis testing with 95% confidence level. The DI method

is implemented in this section using the graphical user interface DIAMOND developed at Los Alamos National Laboratory [Doebling *et al.* (1997)].

4.1.2 Nonlinear Principal Component Analysis NLPCA

Principal Component Analysis (PCA) is a procedure to identify patterns in data allowing identification of their similarities and differences. One of the major advantages of this procedure is the significant reduction of the number of dimensions without much loss of information. PCA has been recently applied to the field of fault detection. However, PCA can only map linear correlations among the variables. NLPCA accounts for nonlinear correlations presented in the data making it more attractive for fault detection implementations. Therefore, a kernel-based algorithm for NLPCA is selected in this section. This algorithm was developed by Scholkopf *et al.* (1998) and states that the following steps must be followed in order to perform a kernel-based PCA. First, compute the matrix $K_{ij} = (k(y_i, y_j))_{ij}$ given a set of centered observations, $y_k = 1, \cdots, y_k \in R^N$, $\sum_{k=1}^{M} y_k = 0$, then solve the equation $M\eta\varsigma = K\varsigma$ by diagonalizing K and normalize the eigenvector expansion coefficients ς_n by requiring $\eta(\varsigma_n \bullet \varsigma_n)$=1. Finally, extract the principal components (corresponding to the kernel k) of a test point $\mathbf{y}$ by computing the projections on the eigenvectors as shown in Eq. (4.6) allowing the calculation of the nonlinear principal components corresponding to Φ. The complete derivation procedure of this algorithm can be found in Scholkopf *et al.* (1998).

$$(V_n \bullet \Phi(y)) = \sum_{i=1}^{M} \varsigma_n k(y_i, y) \tag{4.6}$$

As reported by Scholkopf *et al.* (1998), this procedure corresponds to a standard PCA in some high-dimensional feature space, but avoiding expensive computations in that space. For fault detection, the kernel-based PCA is first implemented using the signals obtained from the healthy state and during normal operational conditions. The main assumption is that when structural damage occurs, the structure may show large deviations in the values of the principal components. Therefore, the Mahalanobis squared distance between the two conditions is used to find significant differences related to structural damage.

4.1.3 Statistical Pattern Recognition Technique

Sohn *et al.* (2003a) presented a comprehensive report providing an overview of existing damage detection methods. The main conclusion that can be drawn from this report is that modal-based damage detection methods usually require large amount of high-quality data and considerable number of sensors strategically located, requirements that are almost impossible to meet in the field. Therefore, the research community has been recently exploring the use of pattern recognition approaches to tackle the problem of reliable damage detection when vibration data are measured at limited locations.

Sohn *et al.* (2001) developed an AR-ARX prediction model, which is solely based on signal analysis of measured vibration data. This model has been successfully implemented in various damage detection problems as reported by Sohn *et al.* (2001). The mathematical derivation of the model begins by using standardized time signals as shown in Eq. (4.7).

$$x(t) = \frac{x_i(t) - \mu_{x_i}}{\sigma_{x_i}} \tag{4.7}$$

where $x(t)$ is the standardized signal of the initial signal $x_i(t)$ at the time step t and and are the mean and standard deviation of $x_i(t)$, respectively. The next step consists on the construction of AR(p) models for each sensor channel. One of the damage identification features that is proposed in this section involves the use of the coefficients of the AR(p) models. Therefore, a computationally efficient stepwise least squares algorithm for the estimation of AR(p) parameters is used herein in conjunction with the AR-ARX model proposed by Sohn *et al.* (2001).

An AR model using the Yule-Walker method as proposed by Sohn *et al.* (2001) is then replaced by the ARfit algorithm proposed by Neumaier & Schneider (2001). This algorithm computes the model order, p_{opt}, that optimizes the order selection criteria using a QR factorization of a data matrix to evaluate, for a sequence of successive orders, the model order and to compute the parameters of the AR(p_{opt}) model. Then, the AR(p_{opt}) model can be represented as shown in Eq. (4.8).

$$x(t) = \sum_{j=1}^{p_{opt}} \varphi_{xj} x(t-j) + e_x(t) \tag{4.8}$$

Once the AR(p_{opt}) model has been constructed, the residual error of the model, $e_x(t)$, is computed by subtracting the data obtained from the AR(p_{opt}) model from the standardized signal, $x(t)$. The AR(p_{opt}) coefficients, will later be used to locate damaged sites. Finally, the residual error, $e_x(t)$, is employed in the construction of the ARX model as shown in Eq. (4.9) by assuming that this residual error, defined by the difference between the measured and the predicted values obtained from the AR model, is mainly caused by an unknown external input.

$$x(t) = \sum_{i=1}^{c} \nu_i x(t-i) + \sum_{j=1}^{d} \tau_j e_x(t-j) + E_x(t) \tag{4.9}$$

where E_x is the residual error after subtracting the ARX(c,d) model from the standardized signal, $x(t)$. Similar results are obtained for different values of c and d as long as the sum of c and d is kept smaller than p_{opt} as reported by Sohn *et al.* (2001). The residual errors from the healthy state are defined as E_x and the residual errors after the occurrence of structural damage are defined as E_y. Finally, using the standard deviations of E_x and E_y, the ratio, $\sigma(E_y)/\sigma(E_x)$, is then defined as the first damage sensitivity feature. A threshold value for this ratio must be computed using measured vibration data obtained from different operational conditions. Therefore, a value of this ratio larger than the computed threshold value indicates the occurrence of damage (Level I). The standard deviation of the Mahalanobis squared distance between healthy and damaged AR(p_{opt}) coefficients is then used to locate structural damaged sites as shown in Eq. (4.10).

$$\chi = \sigma((\varphi_{xj}^{d} - \overline{\varphi}_{xj}^{h})^T s^{-1} (\varphi_{xj}^{d} - \overline{\varphi}_{xj}^{h})) \tag{4.10}$$

where φ_{xj}^{d} are the AR(p_{opt}) coefficients from the damaged state, $\overline{\varphi}_{xj}^{h}$ are the mean values from the healthy state and s is the covariance matrix of φ_{xj}^{h}. The Mahalanobis squared distance is independent of the scale of the AR(p_{opt}) coefficients. Therefore, vibration data collected at the sensor channel closest to the location

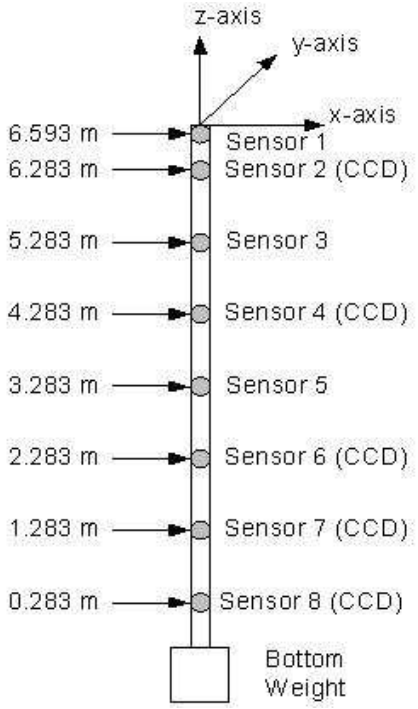

Figure 4.1: Riser Geometry and Sensor Locations

of the structural damage would have the largest values of χ. The proposed AR-ARX prediction model uses two damage sensitivity features, $\sigma(E_y)/\sigma(E_x)$ and χ, to identify and locate structural damage, respectively.

4.2 Comparative Study of Damage Detection in Flexible Risers

The experimental model presented by Senga & Koterayama (2005) is used herein. The properties of the model are provided in 3.2.1. Ten CCD cameras were used to measure the motion of the riser model; each pair of cameras is arranged at the same level in the x-y direction. For the numerical implementation of the vibration-based damage detection approaches, sensors are located where CCD cameras are placed. Two additional sensors were located at points 3 and 5 as shown in Fig. 4.1. Acceleration records are collected at sensor locations in x-axis and y-axis.

One of the main economical constraints for deep-water oil production is related to the design of risers for large safety factors on fatigue damage, which has been found to occur indiscriminately, and with the same magnitude, along the in-line and cross-flow directions as reported by Trim *et al.* (2005). Therefore, in this section structural damage is associated with fatigue damage. Hinge connections are used initially to represent six damage scenarios and are inflicted node-by-node for each of the instrumented locations as shown in Fig. 4.1. The mechanism of the hinge connection is numerically represented by a zero-moment node. Thus, the rotational degree-of-freedoms are released allowing the elements that limit the hinge connection to rotate freely relatively to the zero-moment node. Only intermediate locations are considered. Therefore, hinge connections at sensor locations 2, 3, 4, 5, 6, 7 are used. Table 4.1 shows the proposed damage scenarios and corresponding locations of the hinge connections.

Table 4.1: Damage Scenarios Short Flexible Riser

Damage Scenario	DS1	DS2	DS3	DS4	DS5	DS6
Location of Hinge	2	3	4	5	6	7

The acceleration records of the riser in its healthy state (HS) are collected only at instrumented locations as shown in Fig. 4.1. A time step of 0.01 sec. and a total duration of 24 sec. are used for all the signals in the healthy and damaged states of the riser. Under normal operational conditions the healthy state characterization of the dynamic response of a flexible riser may show deviations that must be considered in order to build the baseline condition of the flexible riser. Because of the inherently limitations of any numerical simulation approach, in this section the baseline condition is defined invariant and is constructed using the experimentally validated response previously presented [3.2.1].

Although acceleration records are collected in the in-line and cross-flow directions, only in-line response is considered in this section for the implementation of the vibration-based damage detection approaches. The main reason is that the VIV process is still not well understood and is extremely complex exhibiting rapid and unpredictable shifts when its response is stationary. Furthermore,

although the sheared flow generating the VIV process can be considered steady, the cross-flow response is mainly non-stationary.

4.2.1 Simulation Results

To evaluate the performance of the three proposed vibration-based damage detection approaches, numerical simulations are performed using a limited number of structural responses to simulate the use of measurements from sensors. The acceleration records at these locations, obtained during the steady state response of the flexible riser, are used for the analysis. The simulation results obtained from the two proposed approaches are presented in the following sections.

4.2.1.1 Modal-Based Damage Detection Results

The first step in the implementation of the proposed modal-based damage detection approach is the calculation of free vibration records from the loading excitation process. NExT is used to estimate impulse response functions from the acceleration records. The reference channel used to calculate the cross-correlation corresponds to sensor 3.

Table 4.2: Identified Modal Parameters

	HS	DS1	DS2	DS3	DS4	DS5	DS6
Freq. (Hz)	0.1038	0.1179	0.1108	0.1196	0.1062	0.1084	0.1120
Sensor 1	1.0000	1.0000	1.0000	1.0000	1.0000	1.0000	1.0000
Sensor 2	0.9604	0.9667	0.9601	0.9646	0.9585	0.9613	0.9582
Sensor 3	0.7872	0.8147	0.7904	0.8117	0.7875	0.7943	0.7880
Sensor 4	0.5289	0.5933	0.5467	0.5920	0.5464	0.5555	0.5503
Sensor 5	0.2407	0.3346	0.2841	0.3338	0.2505	0.2667	0.2864
Sensor 6	-0.0041	0.1028	0.0425	0.1060	-0.0036	0.0291	0.0433
Sensor 7	-0.2092	-0.0923	-0.1532	-0.0962	-0.1843	-0.1843	-0.1634
Sensor 8	-0.3216	-0.2120	-0.2745	-0.2158	-0.3213	-0.3213	-0.2989

Free vibration records calculated from NExT are then used for system identification using ERA. As previously mentioned in section 3.2.2, Senga & Koterayama

(2005) found that their riser model has fundamental periods of 11 sec., 4.8 sec., 3.1 sec. and 2.3 sec. Therefore, only one mode can be identified considering the value of the forced oscillation period defined by Senga & Koterayama (2005) as 8 sec., which is identifiable for a Nyquist frequency equals to a half of the sampling frequency (50 Hz). 40 columns and 200 rows were used to compute the Hankel matrix. Table 4.2 shows the identified modal parameters for the healthy state (HS) and the six damage scenarios.

Table 4.3: Damage Detection Results (Damage Index Method)

Depth (m)	DS1	DS2	DS3	DS4	DS5	DS6
6.5 - 6.0	**1.86**	0.35	0.24	0.03	0.36	0.33
6.0 - 5.5	0.77	0.85	-0.72	-0.12	0.02	-0.41
5.5 - 5.0	-1.07	**1.22**	-1.88	-0.29	-0.46	-0.35
5.0 - 4.5	0.01	0.11	-0.33	0.35	0.46	-0.37
4.5 - 4.0	1.38	-0.54	**1.35**	1.02	1.47	-0.25
4.0 - 3.5	0.26	-0.13	0.29	0.22	0.25	-0.08
3.5 - 3.0	-1.02	-1.05	-0.39	**-0.04**	0.68	-1.65
3.0 - 2.5	-0.51	-0.68	-0.45	0.67	1.04	-1.09
2.5 - 2.0	0.26	0.83	-0.42	1.36	**0.42**	0.88
2.0 - 1.5	0.44	1.33	-0.50	0.93	0.06	1.81
1.5 - 1.0	0.05	0.61	-0.17	-0.32	-0.57	**1.65**
1.0 - 0.5	-0.85	-0.84	0.97	-1.59	-1.56	0.69
0.5 - 0.0	-1.60	-2.07	2.03	-2.21	-2.18	-0.50

Finally, the DI method is used to locate damage. For the implementation of the DI method the riser is divided into 13 segments; the length of each segment is approximately 0.5 m. Table 4.3 shows the damage detection results for the six damage scenarios. Bold numbers indicate the location of the hinge for each of the damage scenarios and therefore it is expected that the damage index, presented in Eq. (4.5), shows the existence of structural damage for these locations. It can be seen from Table 4.3 that none of the damage scenarios is correctly identified. The required confidence level of 95% is not achieved, but there is a clear tendency in DS1, DS2, DS3 and DS6 to identify the location of the hinge with a lower

confidence level. In the case of DS4 and DS5 the DI method failed to locate damage.

There is only one inflection point located in between sensors 5 and 6. At these locations the hinge connection does not considerably affect the dynamic response of the riser after damage. It can partly explain why the DI method failed to identify cases DS4 and DS5. It can also be observed from Table 4.2 that the location of the inflection point moves to a different location as a result of structural damage. The simulation results show that for all damage scenarios the variations of the identified mode shapes, as a result of damage, are not large enough to be detected by the DI method. Although structural damping was not included in the numerical simulations, the hydrodynamic damping induces a non-proportional damping to the riser model. One of the main limitations of any modal-based damage detection approach is that progressive structural damage is a non-stationary phenomena. Furthermore, measured vibration data are also influenced by a non-stationary effect related to the unavoidable variations during normal operational conditions.

Lucor *et al.* (2006) performed full-scale experiments for riser modal identification. A main feature of riser modes, as described by Lucor *et al.* (2006), is that they are complex showing variations in amplitude and phase along the length of the riser and are mainly a mixture of traveling and standing waves. According to Lucor *et al.* (2006), the amount of energy input to a specific region of a riser is a function of the local Strouhal frequency. This amount of energy is then carried away to be dissipated to a different region of the riser, where the local Strouhal frequency is different and the fluid force resists the traveling wave, providing a damping force.

The frequency content of the in-line response is usually lower than the cross-flow response. Higher modes may produce better damage detection results, but considering the cross-flow response, which has a frequency content approximately four times higher that the in-line response in the riser model presented in this section, its results may not be realistic for damage detection, because in sheared flows local response from one region may dominate the total response of a flexible riser by disrupting the excitation process in other regions [Lucor *et al.* (2006)].

4.2.1.2 NLPCA Results

The acceleration records at the specified locations, obtained during the steady state response of the flexible riser, are used for the analysis. The simulation results obtained from the implementation of the NLPCA are presented in Table 4.4. The simulation results show that the kernel-based PCA failed to locate five damage scenarios.

4.2.1.3 AR-ARX Prediction Model Results

The acceleration records are standardized according to Eq. (4.7). Then, the AR-ARX model is implemented for all the signals obtained from the previous step at each sensor channel. The first damage sensitivity feature, $\sigma(E_y)/\sigma(E_x)$, is then used to identify the occurrence of damage (Level I). The threshold value selected for this study is 1.0.

It is important to highlight that it is necessary to define a threshold value for each sensor channel under normal operational conditions, because some regions of the riser are more sensitive to structural damage than the others. Therefore, when new measured vibration data, in the damage state, are collected, one or more sensor channels may indicate significant deviations due to an abnormal structural condition while other sensor channels may indicate that the riser has not suffered structural damage. The results of the first damage sensitivity feature, $\sigma(E_y)/\sigma(E_x)$, for the six damage scenarios, are presented in Table 4.5.

In Table 4.5, sensor 4 shows the largest deviations in the calculation of the first damage sensitivity features for four damage scenarios. Sensor 3 and 5 are also sensitive to damage scenarios DS5 and DS4, respectively. On the other hand, sensor 6 is almost insensitive to any damage scenario due to its proximity to the inflection point, but locations of the inflection points are extremely important in the area of structural health monitoring due to the fact that an abnormal response in this region may be automatically related to structural damage. Furthermore, these regions are almost insensitive to environmental conditions, which, in some cases, induce large variations in the measured vibration data and therefore false identification of structural damage.

Table 4.4: Kernel-Based PCA Results

	DS1	DS2	DS3	DS4	DS5	DS6
Sensor 1	6.223	6.779	6.355	6.584	6.235	6.782
Sensor 2	6.350	6.938	6.558	6.832	6.468	7.022
Sensor 3	6.015	6.712	6.039	6.302	5.823	6.575
Sensor 4	5.930	6.821	5.918	6.224	5.783	6.612
Sensor 5	5.970	6.775	5.983	6.196	5.806	5.538
Sensor 6	6.027	6.722	6.005	6.225	6.720	6.514
Sensor 7	6.061	6.469	6.045	6.209	5.789	6.329
Sensor 8	6.146	6.194	6.166	6.150	6.077	6.172

Table 4.5: First Damage Sensitivity Feature Results (Short Flexible Riser)

	DS1	DS2	DS3	DS4	DS5	DS6
Sensor 1	1.000	0.992	0.983	1.001	0.981	1.000
Sensor 2	0.952	1.083	1.440	1.004	1.289	1.041
Sensor 3	1.105	1.302	1.489	1.028	1.508	1.215
Sensor 4	1.298	1.369	1.846	1.248	1.484	1.247
Sensor 5	1.189	1.071	1.329	1.346	1.019	1.003
Sensor 6	0.903	0.940	0.905	0.960	1.088	0.910
Sensor 7	1.014	0.983	1.154	0.973	1.157	1.170
Sensor 8	0.981	0.870	0.988	1.029	1.058	0.911

The second step in the proposed AR-ARX prediction model is the calculation of the second sensitivity feature, χ, which is related to the location of structural damage (Level II). The order of the AR model using the ARfit algorithm was 104 and a ARX(10,10) model was selected for all damage scenarios. In Table 4.6, the calculation of the second sensitivity features for all damage scenarios is presented. It can be seen from Table 4.6 that structural damage is correctly located for five damage scenarios, only the case DS3 is not located properly. Nevertheless, the value of the second sensitivity feature for the real location of damage in DS3 shows a small deviation from the maximum values obtained from sensor channels 5, 6 and 7.

Table 4.6: Second Damage Sensitivity Feature Results (Short Flexible Riser)

	DS1	DS2	DS3	DS4	DS5	DS6
Sensor 1	3.286	3.264	1.669	3.822	1.664	3.825
Sensor 2	7.507	5.933	4.726	6.494	5.180	5.943
Sensor 3	6.774	6.689	3.873	5.765	4.735	5.402
Sensor 4	5.692	4.609	4.992	5.722	4.717	5.088
Sensor 5	5.499	4.850	4.998	7.441	4.394	5.341
Sensor 6	5.933	5.433	5.007	5.961	5.837	6.054
Sensor 7	5.410	5.149	5.288	5.535	5.410	6.706
Sensor 8	5.717	5.231	4.381	6.480	5.011	6.097

The numerical results presented in Tables 4.5 and 4.6 show that structural damage was identified and located using the proposed damage sensitivity features. In order to study the sensitivity of the presented AR-ARX prediction model to identify and locate structural damage, when the hinge connection due to fatigue is created in nodes where sensors are not located, three additional damage scenarios are defined using Fig. 4.1. The proposed damage scenarios are DS7, DS8 and DS9 having hinge connections at depths of 3.5 m, 2.5 m and 1.5 m, respectively. The numerical results for the three additional damage scenarios are presented in Table 4.7.

The numerical results presented in Table 4.7 show that the first damage sensitivity feature indicates the occurrence of damage especially at locations of sensors 4, 5 and 6. The location of damage in these damage scenarios is not related to a single sensor location, the inflicted damage may affect a region of the riser, which in some cases can not be measured by only one sensor channel highlighting the importance of having a dense array of sensors for continuous damage monitoring implementations. Finally, a comparative study is presented in this section using the previously defined six damage scenarios, but instead of using hinge connections, structural damage is modeled as a 10% stiffness reduction of elements at locations defined in Table 4.8. The node locations of the damaged elements are expressed in meters. Then, the reduction of stiffness in an element length of 0.217 m represents the formation of the hinge connection at its initial stage.

Table 4.7: Damage Detection Results (Cases DS7, DS8 and DS9)

	$\sigma(E_y)/\sigma(E_x)$			χ		
	DS7	DS8	DS9	DS7	DS8	DS9
Sensor 1	3.286	3.264	1.669	3.822	1.664	3.825
Sensor 2	7.507	5.933	4.726	6.494	5.180	5.943
Sensor 3	6.774	6.689	3.873	5.765	4.735	5.402
Sensor 4	5.692	4.609	4.992	5.722	4.717	5.088
Sensor 5	5.499	4.850	4.998	7.441	4.394	5.341
Sensor 6	5.933	5.433	5.007	5.961	5.837	6.054
Sensor 7	5.410	5.149	5.288	5.535	5.410	6.706
Sensor 8	5.717	5.231	4.381	6.480	5.011	6.097

Table 4.8: Damage Scenarios Short Flexible Riser

Damage Scenario	DSA	DSB	DSC	DSD	DSE	DSF
Upper node of damaged element	6.5	5.5	4.5	3.5	2.5	1.5
Lower node of damaged element	6.283	5.283	4.283	3.283	2.283	1.283

Table 4.8 shows the distances, measured from the top end of the riser, corresponding to the upper and the lower nodes that limit the damaged elements. The damage detection results from the damage scenarios at their initial stages are presented in Tables 4.9 and 4.10. It can be seen from Table 4.9 that the first sensitivity feature has values closer to the previously defined threshold value. Sensors 4, 5 and 6 do not clearly indicate the occurrence of damage in contrast to the numerical results considering hinge connections. There is a large deviation in the presented values of DSA, which may be caused due to its proximity to the top end of the riser model. In Table 4.10, only the damage scenario DSA is correctly located showing that the occurrence of damage presented in Table 4.9, shows large deviation in its values, is correctly linked to the second sensitivity feature. The damage results presented in Table 4.10 show that the remaining damage scenarios are not correctly identified.

The modal-based damage detection approach suffers from limitations related to the correct identification of the mode shapes as previously explained. The

Table 4.9: First Damage Sensitivity Feature Results (Initial Stage)

	DS1	DS2	DS3	DS4	DS5	DS6
Sensor 1	0.998	0.983	0.999	1.000	0.995	0.982
Sensor 2	1.206	1.200	1.224	1.148	1.018	1.018
Sensor 3	1.244	1.229	1.218	1.084	1.033	1.031
Sensor 4	1.431	1.363	1.201	1.011	1.086	1.116
Sensor 5	1.316	1.218	1.064	1.064	1.045	1.080
Sensor 6	1.011	1.148	1.103	1.147	1.063	1.096
Sensor 7	1.068	1.147	1.048	0.998	1.037	1.043
Sensor 8	0.982	1.043	1.001	1.094	1.027	1.043

Table 4.10: Second Damage Sensitivity Feature Results (Initial Stage)

	DS1	DS2	DS3	DS4	DS5	DS6
Sensor 1	3.820	1.661	3.820	3.824	3.805	1.663
Sensor 2	6.820	5.261	6.827	6.802	6.593	5.016
Sensor 3	6.031	4.558	6.131	5.951	5.691	4.172
Sensor 4	5.998	5.178	6.404	6.237	5.967	4.734
Sensor 5	6.353	4.447	6.297	6.270	6.141	4.080
Sensor 6	6.147	4.471	6.087	6.323	5.889	4.096
Sensor 7	6.746	5.666	6.409	6.374	5.938	4.901
Sensor 8	6.026	4.467	6.533	6.809	6.190	4.524

simulation results presented in this section show that the proposed modal-based approach could not identify with acceptable level of confidence the existence of structural damage as shown in Table 4.3. Similar results were obtain for NLPCA as shown in Table 4.4. On the other hand, the presented AR-ARX prediction model is independent of the aforementioned problems related to modal identification in risers and therefore is solely based on measured vibration data. The simulation results presented in Table 4.5 show that it is possible to have at least one sensor channel sensitive enough to identify the occurrence of structural damage. Table 4.6 shows that additional information related to the location of damage, which is extremely useful for work site inspection prioritization, can be

obtained from the presented AR-ARX model.

Finally, the undesirable non-stationary effect related to progressive damage is avoided by the AR-ARX prediction model as shown in Tables 4.9 and 4.10, where the structural damage at its initial stage is not reported for most of the damage scenarios. Therefore, false damage identification, which is also of concern for its economical implications, is therefore partially avoided. A threshold value obtained from measured data at different operating conditions can tell the owner when a significant deviation of the measured vibration data collected in real time significantly deviate from normal operational conditions, which is extremely useful for health integrity of riser's systems.

4.2.2 Concluding Remarks

The numerical implementation of three vibration-based damage detection approaches on a flexible riser model was presented. A numerical scheme for dynamic response of flexible risers developed by the author was used to obtain the dynamic response of the flexible riser model under different structural conditions. The healthy condition of the flexible riser model was experimentally validated.

The modal-based damage detection approach presented in this section consists of three widely recognized methodologies namely NExT, ERA and the Damage Index method. The main objective of this implementation was to show the limitations of the modal approach when is used in flexible risers. The main difficulties arise from variation of the structural mass, non-stationary response in the cross-flow direction and hydrodynamic damping.

The Damage Index method could locate the damage scenarios presented in this section with a low confidence level. However, it was impossible to locate structural damage when it was inflicted near the inflection point. The use of the higher modes was avoided in order to present more realistic results, because the VIV process is still not well-understood involving non-stationary response and a self-regulated process. The numerical results of the NLPCA show a similar trend.

A statistical pattern recognition method based on time series analysis was used to show a more attractive approach for flexible risers. Acceleration records were collected at location of sensors and analyzed in order to obtain the two

damage sensitivity features presented in this section. Six damage scenarios were studied, the first damage sensitivity feature was able to indicate the occurrence of damage and the location of five damage scenarios was correctly identified for the second sensitivity feature.

Three additional damage scenarios were used to show the ability of the proposed statistical-based approach. The occurrence of damage was identified. However, the location of damage was spread into a larger identified region. Finally, the initial stages of the proposed damage scenarios were simulated by reducing the stiffness of short elements located in sensor regions. Although damage was not clearly identified, the stability of the proposed statistical-based approach was demonstrated.

A flexible riser involves many challenges due to its complex nonlinear behavior. The numerical scheme for dynamic response of flexible risers presented in this section was developed in order to be used in damage detection studies. Other approaches may be extremely computationally demanding when several damage scenarios have to be simulated as in the study case presented in this section, mainly those approaches involving the calculation of the fluid forces using CFD.

4.3 Damage Detection in Long Flexible Risers

4.3.1 Optimum Sensor Placement

Several researchers have made remarkable contributions to the development of methodologies for optimum sensor placement. One of these methodologies is the effective independence method developed by Kammer (1991). This method is based on the concept that sensors must be placed in order to obtain mode shapes linearly independent of each other as possible. In the formulation of this method, Kammer (1991) used the Fisher Information Matrix (FIM) defined in Eq. (4.11).

$$[G]_{m\times m} = [\psi]^T_{m\times N}\,[\psi]_{m\times N} = \sum_{i=1}^{N}([\psi]_i^T\,[\psi]_i) \tag{4.11}$$

where $[\psi]_i = [\psi_{i1}, \psi_{i2}, \cdots, \psi_{im}]$ is a row vector of the mode shapes corresponding to the ith DOF, N is the number of DOF, and m is the number of the selected

mode shapes, which must be mass-normalized. $\mathbf{G}$ is symmetric and positive definite and its eigensolution is determined as shown in Eq. (4.12).

$$([G] - [\lambda]_i[I])[\Psi]_i = 0 \tag{4.12}$$

where λ_i and Ψ_i are the ith eigenvalue and corresponding eigenvector of $\mathbf{G}$, respectively. $[\Psi]_i = [\Psi_{i1}, \Psi_{i2}, \cdots, \Psi_{im}]$ is a row vector of eigenvectors of $\mathbf{G}$ corresponding to ith DOF. The product $\psi\Psi$ is a matrix of values containing the projection of the mode shapes into the m-dimensional space spanned by the vectors contained in the matrix Ψ. Squaring each element in the matrix $\psi\Psi$ results in a matrix in which each element represents the contribution of each DOF to each mode. If weighted by the inverse of the corresponding natural frequency of the mode, each element in this matrix has equal importance. The effective independence vector distribution vector, E_d, represents the contribution of each DOF to the selected mode shapes and is obtained by the summation of all terms corresponding to each DOF. The DOF corresponding to the largest element of E_d is the DOF that contributes most to the rank of $\mathbf{G}$, and thus should be retained. By repeating the process of removing the DOF with the smallest contribution to the rank of $\mathbf{G}$ until the desired number of sensors is achieved, the sensor locations can be determined.

4.3.2 Numerical Implementation

The first step in the numerical implementation of the statistical pattern recognition technique is the optimum location of sensors using the effective independence method. It is important to note that the selected mode shapes are relevant in the calculation of the optimum sensor locations. Basically, the range of frequencies in which a flexible riser is excited may determine the mode shapes involved in any optimum sensor placement procedure. In this section, the selection of the mode shapes for optimum sensor placement is based on the value of the frequency of the exciting force at the top end of the riser. Therefore, the first two modes in the x-axis are selected. These modes correspond to values of frequencies lower than 0.5 cycles/sec. The optimum distribution of sensors is depicted in Fig. 4.2. Accelerations records are then recorded at sensor locations in x-axis and y-axis.

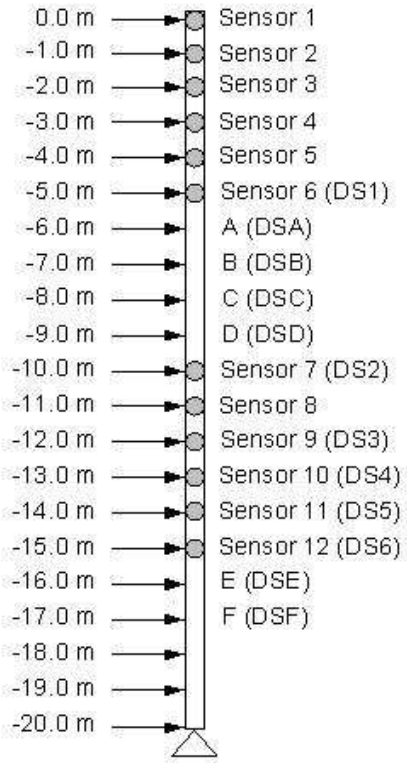

Figure 4.2: Sensor Locations and Damage Scenarios

As previously mentioned, structural damage is associated with fatigue damage. Therefore, hinge connections are used to represent twelve damage scenarios. The first six cases are coincident with sensor locations. The locations of the hinges for the other six cases correspond to non-instrumented regions as shown in Fig. 4.2. Tables 4.11 and 4.12 show the proposed damage scenarios and corresponding locations of the hinge connections. The acceleration records of the riser in its healthy state are collected only at instrumented locations as shown in Fig. 4.2. A time step of 0.01 sec. and a total duration of 30 sec. are used for all the signals in the healthy and damaged states of the riser.

Table 4.11: Damage Scenarios (Case I)

Damage Scenario	DS1	DS2	DS3	DS4	DS5	DS6
Location of Hinge	6	7	9	10	11	12

Table 4.12: Damage Scenarios (Case II)

Damage Scenario	DSA	DSB	DSC	DSD	DSE	DSF
Location of Hinge	A	B	C	D	E	F

4.3.3 Simulation Results

To evaluate the performance of the presented statistical pattern recognition technique, damage is inflicted to the nodes where hinges are placed and acceleration records are collected at sensor locations in order to simulate the use of measurements at limited locations. Vibration data are collected during the steady state. The acceleration records are standardized according to Eq. (4.7). Then, the AR-ARX model is implemented for all signals. The first damage sensitivity feature, $\sigma(E_y)/\sigma(E_x)$, is then used to identify the occurrence of damage (Level I). According to Sohn *et al.* (2003b), if $\sigma(E_y) \geq 1.4\sigma(E_x)$, the riser is considered to have reached the damaged condition. On the other hand, if $\sigma(E_y) \leq 1.2\sigma(E_x)$, the riser is considered to be undamaged. However, if $1.2\sigma(E_x) \leq \sigma(E_y) \leq 1.4\sigma(E_x)$, the condition of the riser cannot be assessed and it is necessary to collect additional measurements in order to identify a possible abnormal condition.

The simulation results for the first damage sensitivity feature are presented in Table 4.13. It can be seen from Table 4.13 that all damage scenarios are correctly identified. The values found for the first damage sensitivity feature are located in the damaged region having values larger than 1.4 as previously explained. The second step in the presented statistical pattern recognition technique accounts for the calculation of the second sensitivity feature, χ, which is related to the location of structural damage. Table 4.14 presents the results obtained for the second damage sensitivity feature.

Table 4.13: First Damage Sensitivity Feature Results (Case I)

	DS1	DS2	DS3	DS4	DS5	DS6
Sensor 1	1.002	1.000	0.999	0.998	1.003	1.004
Sensor 2	1.019	1.008	1.022	1.029	1.027	1.047
Sensor 3	1.038	1.024	1.085	1.092	1.107	1.123
Sensor 4	1.046	1.013	1.068	1.086	1.094	1.107
Sensor 5	1.056	0.994	1.091	1.113	1.126	1.150
Sensor 6	1.467	1.020	1.161	1.158	1.162	1.193
Sensor 7	1.544	1.540	1.066	1.157	1.164	1.155
Sensor 8	0.982	1.224	1.522	1.512	1.455	1.227
Sensor 9	0.944	1.108	1.371	1.056	1.189	1.233
Sensor 10	1.052	1.076	1.083	1.617	1.161	1.159
Sensor 11	0.985	1.013	1.011	0.996	1.385	1.061
Sensor 12	1.044	1.058	1.068	1.078	1.097	1.503

The numerical results presented in Table 4.14 show that two damage scenarios are correctly located. It can also be observed that sensor 5 is sensitive to the second damage sensitivity feature. In the part of the riser where sensor 5 is located there is a change in the curvature of the second mode shape. This fact can partially explain this sensitiveness. The results from the second damage sensitivity feature can be used to provide additional information related to the occurrence of damage. Although the second damage sensitivity feature results are less accurate than the first damage sensitivity feature results, when structural

Table 4.14: Second Damage Sensitivity Feature Results (Case I)

	DS1	DS2	DS3	DS4	DS5	DS6
Sensor 1	6.35	6.72	6.39	5.65	6.30	5.81
Sensor 2	6.35	4.74	6.47	5.00	5.23	5.39
Sensor 3	3.11	5.26	3.06	3.25	1.95	1.79
Sensor 4	5.70	5.38	6.41	6.72	7.86	9.92
Sensor 5	9.53	4.57	9.52	13.84	14.97	14.70
Sensor 6	10.92	5.62	8.50	7.69	9.74	10.51
Sensor 7	5.02	13.44	6.80	8.12	6.44	11.07
Sensor 8	4.03	6.34	6.37	4.69	5.56	5.46
Sensor 9	4.36	6.03	2.95	2.01	2.74	2.96
Sensor 10	4.34	5.76	5.95	10.24	6.80	6.45
Sensor 11	5.71	9.19	6.29	6.98	12.48	6.43
Sensor 12	3.01	2.82	6.84	6.31	4.92	13.38

damage is evident, the information of the second sensitivity feature can be used to prioritize the regions of the riser to be inspected.

The simulation results presented in Table 4.14 show a tendency of large values at sites where damage is inflicted. Only the case DS3 does not show this tendency having small differences among the computed values. In order to study the sensitivity of the presented statistical pattern recognition technique to identify structural damage when a hinge connection, related to fatigue damage, is created in nodes where sensors are not located, six additional damage scenarios are simulated as shown in Table 4.12. The simulation results for the first damage sensitivity feature obtained from the six additional cases, where hinges are located at non-instrumented nodes, are presented in Table 4.15.

The simulation results presented in Table 4.15 show that only the damage scenarios DSB and DSF are not correctly identified. The location of damage in the damage scenarios presented in Table 4.15 is not related to a single sensor location, the inflicted damage may affect a region of the riser, which in some cases cannot be detected by only one sensor channel highlighting the importance of having a dense array of sensors for continuous damage monitoring implementations. Due

Table 4.15: First Damage Sensitivity Feature Results (Case II)

	DSA	DSB	DSC	DSD	DSE	DSF
Sensor 1	1.002	1.002	0.999	0.998	1.002	0.999
Sensor 2	1.037	1.041	1.032	1.031	1.063	1.030
Sensor 3	1.099	1.115	1.108	1.097	1.155	1.087
Sensor 4	1.087	1.087	1.105	1.078	1.150	1.053
Sensor 5	1.095	1.127	1.132	1.122	1.172	1.095
Sensor 6	1.164	1.174	1.158	1.171	1.202	1.156
Sensor 7	1.094	1.139	1.137	1.216	1.813	1.132
Sensor 8	1.527	1.145	1.548	1.654	1.454	0.994
Sensor 9	1.056	0.990	1.082	1.037	1.263	1.075
Sensor 10	1.102	1.125	1.139	1.125	1.175	1.108
Sensor 11	1.017	1.022	1.029	1.015	1.076	0.994
Sensor 12	1.079	1.095	1.090	1.069	1.159	1.061

to the proximity of the damage scenario DSF to the bottom end of the riser it is expected low amplitude responses at nearby sensor channels and therefore limitations in finding significant differences during a time series analysis. In the in-line response there is only one inflection point located at B in the second mode shape, which corresponds to the case DSB. At this location the hinge connection does not considerably affect the dynamic response of the riser after damage. It can partially explain why the statistical pattern recognition technique failed to identify correctly case DSB. However, the instrumentation of inflection points is extremely important in the area of structural health monitoring due to the fact that an abnormal response in this region may be automatically related to structural damage. Furthermore, these regions are almost insensitive to environmental conditions as previously mentioned. The second damage sensitivity feature results for case II are presented in Table 4.16. The same tendency presented in Table 4.14 is also observed for the simulation results presented in Table 4.16, but it is important to note that damage is not related to a single damage location for case II. Finally, three additional sensors are used to study the cases in which damage was not identified. New sensors locations at -6 m, -9 m -16m are obtained

Table 4.16: Second Damage Sensitivity Feature Results (Case II)

	DSA	DSB	DSC	DSD	DSE	DSF
Sensor 1	6.28	6.22	5.97	6.11	5.59	6.20
Sensor 2	6.09	5.89	5.70	4.37	4.86	8.52
Sensor 3	2.28	2.59	2.44	3.47	2.34	2.67
Sensor 4	7.49	7.28	8.57	7.38	9.67	6.56
Sensor 5	12.91	9.14	18.37	14.13	16.33	10.14
Sensor 6	10.37	9.64	7.46	9.82	11.21	5.81
Sensor 7	7.25	7.75	10.35	6.46	14.59	8.22
Sensor 8	5.28	5.28	5.84	11.44	6.30	5.80
Sensor 9	2.56	2.89	2.18	2.29	4.40	2.14
Sensor 10	6.78	6.48	8.10	5.96	7.62	5.42
Sensor 11	8.67	11.04	7.69	6.26	6.37	6.39
Sensor 12	5.22	7.40	6.53	5.28	7.91	4.78

from the effective independence method. The damage detection results are shown in Table 4.17.

4.3.4 Concluding Remarks

In this section, the numerical implementation of a statistical pattern recognition technique for vibration-based damage detection in flexible risers was presented. The proposed semi-empirical prediction model for oscillating flexible risers was used to perform the damage detection study. The healthy state of the riser was experimental validated. Good agreement in amplitude response was observed between experimental data and simulation results as previously mentioned. The statistical pattern recognition technique used in this section was selected based on previous research work that proves the best performance of this technique over other existing vibration-based methods, especially modal-based approaches. Acceleration records were collected at optimal sensor locations and analyzed in order to obtain two damage sensitivity features related to identification and location of structural damage. The numerical results show that the presented statistical pattern recognition technique was able to identify the occurrence of damage with

Table 4.17: Damage Detection Results (Cases DSB and DSF)

	$\sigma(E_y)/\sigma(E_x)$		χ	
	DSB	DSF	DSB	DSF
Sensor 1	0.999	0.999	5.57	5.76
Sensor 2	1.040	1.030	7.73	9.22
Sensor 3	1.116	1.087	4.71	3.51
Sensor 4	1.088	1.054	7.91	8.10
Sensor 5	1.127	1.095	6.40	3.42
Sensor 6	1.175	1.157	8.88	7.63
Sensor 13	1.178	1.104	11.00	9.41
Sensor 14	1.335	1.113	7.48	7.20
Sensor 7	1.138	1.133	14.29	6.24
Sensor 8	1.145	0.995	6.47	6.93
Sensor 9	0.994	1.080	4.44	3.65
Sensor 10	1.130	1.112	6.89	5.75
Sensor 11	1.022	0.994	13.44	9.78
Sensor 12	1.095	1.061	4.77	3.77
Sensor 15	1.075	1.031	5.30	11.58

relatively good resolution. The second sensitivity feature locate the structural damage with a lower resolution that the first sensitivity feature, so it can be used to provide additional information of the regions of the riser that must be inspected.

Vandivier (1998) presented a comprehensive analysis of the main challenges related to instrumented marine risers. Basically, the use of accelerometers introduces a gravitational error component into the signals. On the other hand, other alternatives such as strain gages are expensive and difficult to install and calibrate. The optimum sensor placement method presented in this thesis may also have a practical limitation for deep-water riser's implementations due to the large number of excited modes. Therefore, in order to provide a practical methodology for sensor placement, it is necessary to identify the riser's structural modes that are likely to be excited during normal operating conditions. The AR-ARX pre-

diction model can be easily incorporated in full-scale instrumentation projects if a reliable baseline condition of the flexible riser is provided. The statistical treatment of the proposed damage sensitivity features must be considered in order to improve the presented statistical-based damage detection approach. The numerical implementation presented in this section showed that it is possible to partially solve the problem of structural deterioration using s vibration-based approach, which indeed optimize the use of visual inspection and Non-Destructive Evaluation (NDE) techniques. The envisioned Structural Health Monitoring (SHM) approach for marine risers must integrate global SHM and local NDE Techniques.

Chapter 5

Conclusions

A response prediction model for flexible risers was presented in this thesis. Experimental data obtained from a 20-meter and a 35-meter riser models, sinusoidally excited at their top end, were used to validate the proposed prediction model. A quasi-steady model was used to predict the cross-flow response using amplitude-dependent lift coefficients. It was also employed an increased mean drag coefficient model in order to consider drag amplification during synchronization events. Good agreement in amplitude response was found for both in-line and cross-flow displacements. Some differences were found in the predicted response in the in-line direction for the model tested in the asymmetric and transverse regimes. It is important to highlight that in this thesis it is assumed amplitude-dependent lift coefficients. Therefore, cross-flow response is more accurately predicted when $A_y/D < 0.5$. As previously mentioned, VIV oscillations become more nonlinear when $A_y/D > 0.5$. Most of the cross-flow displacements achieved by the experimental models are located beyond the aforementioned limit.

The response prediction of an oscillating flexible riser involves several challenges due to the nonlinear and self-regulated nature of the VIV process. It has been sufficiently proved that synchronization events cause an increase of cross-flow displacements leading to a sudden increase in the drag force and therefore affect the whole in-line response of the riser. Furthermore, the dynamic response of a flexible riser having a value of mass ratio lower than 3.3 is more complex due to the existence of 3 modes of response in contrast with the 2 modes of response found in risers having values of mass ratio larger than 10. Although VIV can

occur in both steady currents and oscillatory flow, only the oscillatory flow case was presented in this thesis. In steady currents, in the lock-in region, the VIV process may also induce large oscillating amplitudes in the riser as the reduced velocity is increased to a critical value, but when the cross-flow amplitude reaches a certain value, the vortex shedding changes and then the cross-flow amplitude decreases. The oscillatory flow case exhibits more complex behavior because the lock-in conditions can be achieved several times. Considering the nonlinear and self-regulated nature of the VIV process, especially during synchronization events that leads to large displacements and sudden changes in the phase angle of the lift force, this thesis presents a practical methodology for response prediction of oscillation flexible risers.

In the second part of this thesis, the numerical implementation of a statistical pattern recognition technique for fault detection in flexible risers was presented. One of the main economical constraints for deep-water oil production is related to the design of risers for large safety factors on fatigue damage, which has been found to occur indiscriminately, and with the same magnitude, along the in-line and cross-flow directions. Therefore, in this thesis structural damage is associated with fatigue damage. Hinge connections were used to represent damage scenarios at different locations. One important issue to be considered for future implementations is the use of wireless monitoring systems for SMH systems as proposed by Lynch (2002). Therefore, high level research must be conducted in the area of sensing technology in order to accompany the experimental implementation on riser systems. The sensor unit developed by Lynch (2002), having embedded software, is one of the best available sensing technologies for SHM systems. It is expected that the cost of such sensing units will be gradually reduced make them more affordable for large-scale implementations. Considering current accessibility limitations and the danger associated to labor inspections in riser's systems, this study shows a practical statistical-based approach for damage monitoring of flexible risers. The riser's health condition obtained from this approach can improve the procedure currently employed in inspection works.

Appendix A

Associated Publications

Award

- Best Student Paper Award (Modi Prize) (2007). International Society of Offshore and Polar Engineers ISOPE, USA.

Peer Review Journal Publications

- Riveros, C., Utsunomiya, T., Maeda, K. and Itoh, K. Response prediction of long flexible risers subject to forced harmonic vibration. *Journal of Fluids and Structures*, in review.

- Riveros, C., Utsunomiya, T., Maeda, K. and Itoh, K. Dynamic response of oscillating flexible risers under lock-in events. *International Journal of Offshore and Polar Engineering*, in review.

- Riveros, C., Utsunomiya, T., Maeda, K. and Itoh, K. Modelling the response of flexible risers in the quasi-steady regime. *Journal of Applied Mechanics JSCE*, in press.

- Riveros, C., Utsunomiya, T., Maeda, K. and Itoh, K. (2008). Damage detection in flexible risers using statistical pattern recognition techniques. *International Journal of Offshore and Polar Engineering*, **18(1)**, 35-42.

- Riveros, C., Utsunomiya, T., Maeda, K. and Itoh, K. (2007). Vibration-based damage detection in flexible risers using time series analysis. *Structural Engineering/Earthquake Engineering*, **24(2)**, 62s-72s.

- Riveros, C., Utsunomiya, T., Maeda, K. and Itoh, K. (2007). CFD modeling of fluid-structure interaction for oscillating flexible risers. *Journal of Applied Mechanics JSCE*, **10**, 1099-1108.

- Riveros C., Utsunomiya, T., Maeda, K. and Itoh, K. (2006). Numerical scheme for dynamic response of deep-water risers. *Journal of Applied Mechanics JSCE*, **9**, 1149-1158.

Peer Review Conference Publications

- Riveros, C., Utsunomiya, T., Maeda, K. and Itoh, K. (2007). Damage detection in flexible risers using statistical pattern recognition techniques. Proceedings of the 17th International Offshore and Polar Engineering Conference ISOPE-2007, Lisbon, Portugal, 2746-2753.

- Riveros, C., Utsunomiya, T., Maeda, K. and Itoh, K. (2007). Dynamic response of oscillating flexible risers under lock-in events. Proceedings of the 17th International Offshore and Polar Engineering Conference ISOPE-2007, Lisbon, Portugal, 2730-2737.

Conference Publications and Presentations

- Riveros, C., Utsunomiya, T., Maeda, K. and Itoh, K. (2008). Response prediction of oscillating flexible risers at large values of Keulegan-Carpenter number. The 20th Conference of the Japan Society of Naval Architects and Ocean Engineers, Nagasaki, Japan.

- Riveros, C., Utsunomiya, T., Maeda, K. and Itoh, K. (2008). Numerical prediction of dynamic reponse of oscillating flexible risers. The 63th JSCE Annual Meeting, Sendai, Japan.

- Riveros, C., Utsunomiya, T., Maeda, K. and Itoh, K. (2008). Experimental validation of a response prediction model for flexible risers in the inertia/drag regime. The 10th International JSCE Summer Symposium, Tokyo, Japan.

- Riveros, C., Utsunomiya, T., Maeda, K. and Itoh, K. (2007). A quasi-steady approach for dynamic response of flexible risers at low values of beta parameter. The 19th Conference of the Japan Society of Naval Architects and Ocean Engineers, Tokyo, Japan.

- Riveros, C., Utsunomiya, T. (2007). Signal analysis of measured vibration data for fault detection in flexible risers. The 9th International JSCE Summer Symposium, Yokohama, Japan.

- Riveros, C., Utsunomiya, T. (2007). Calculation of hydrodynamic force coefficients for oscillating flexible risers using numerical simulation. The 62th JSCE Annual Meeting, Hiroshima, Japan.

- Riveros, C., Utsunomiya, T. (2006). Dynamic prediction model for risers in sheared flow. The 19th KKCNN Symposium on Civil Engineering, Kyoto, Japan.

- Riveros, C., Utsunomiya, T. (2006). Numerical simulation of vortex-induced vibrations for flexible risers at low Reynolds numbers. The 8th International JSCE Summer Symposium, Nagoya, Japan.

- Riveros, C., Utsunomiya, T. (2006). Dynamic response of a flexible riser sinusoidally excited at its top-end using the quasi-steady model. The 61th JSCE Annual Meeting, Kusatsu, Japan.

References

ABAQUS (2007). *Standard User's Manual, Version 6.7*. 31, 46

Al-Jamal, H. & Dalton, C. (2005). The contrast in phase angles between forced and self-excited oscillations of circular cylinder. *Journal of Fluids and Structures*, **20**, 467–482. 28

Anagnostopoulos, P. & Minear, R. (2004). Blockage effect of oscillatory flow past a fixed cylinder. *Applied Ocean Research*, **26**, 147–153. 50, 52

Anderson, J.D. (1991). *Fundamentals of Aerodynamics*. McGraw-Hill. 51

Barroso, L. & Rodriguez, R. (2004). Damage detection utilizing the Damage Index method to a benchmark structure. *Journal of Engineering Mechanics ASCE*, **130**, 142–151. 83

Bearman, P., Graham, J., Naylor, P. & Obasaju, E. (1981). The role of vortices in oscillatory flow about bluff cylinders. In *Proceedings of the International Symposyum on Hydrodynamics in Ocean Engineering*. 19

Bearman, P., Graham, J. & Obasaju, E. (1984). A model equation for the transverse forces on cylinders in oscillatory flows. *Applied Ocean Research*, **6**, 166–172. 38

Bearman, P., Downie, M., Graham, J. & Obasaju, E. (1985). Forces on cylinders in viscous oscillatory flow at low Keulegan-Carpenter number. *Journal of Fluid Mechanics*, **154**, 337–356. 52

Beyle, A.I., Gustafson, C., Kulakov, V. & Tarnopolskii, Y. (1997). Composite risers for deep-water offshore technology: Problems and prospects 1. metal composite riser. *Mechanics of Composite Materials*, **33(5)**, 1997. 9

Bishop, R. & Hassan, A. (1964). The lift and drag forces on a circular cylinder oscillating in a flowing flow. *Proceedings of Royal Society of London*, **277A**, 51–75. 24

Blevins, R.D. (1990). *Flow-induced Vibration*. Krieger Publishing Co. 13, 20, 22, 23, 24, 41, 48, 69, 70

Blevins, R.D., Jacob, P., Saint-Marcoux, J.F. & Wu, M. (2006). Assessment of flow-induced jumper interference for hybrid riser tower. In *Proceedings of the 16th International Offshore and Polar Engineering Conference*. 8

Campos, L. & Martins, C. (2001). Nonlinear dynamic response of a steel catenary riser at the touch-down point. In *Proceedings of the 11th International Offshore and Polar Engineering Conference*. 6

Carberry, J., Sheridan, J. & Rockwell, D. (2005). Controlled oscillations of cylinders: Forces and wake modes. *Journal of Fluid Mechanics*, **538**, 31–69. 40, 46, 47

Chakrabarti, S.K. (2002). *The Theory and Practice of Hydrodynamics and Vibration*. World Scientific Publishing. 5, 12, 14, 16

Chance, J., Tomlinson, G. & Worden, K. (1994). A simplified approach to the numerical and experimental modeling of the dynamics of a cracked beam. In *Proceedings of the 12th International Modal Analysis Conference*. 83

Chaplin, J., Bearman, P., Cheng, Y., Fontaine, E., Graham, J., Herfjord, M., Isherwood, M., Lambrakos, K., Larsen, C., Meneghini, J., Moe, G., Triantafyllou, M. & Willden, R. (2005a). Blind predictions of laboratory measurements of vortex-induced vibrations of a tension riser. *Journal of Fluids and Structures*, **21**, 25–40. xi, 28, 31, 32, 33, 34, 43

Chaplin, J., Bearman, P., Huera-Huarte, F. & Pattenden, R. (2005b). Laboratory measurements of vortex-induced vibrations of a vertical tension riser in a stepped current. *Journal of Fluids and Structures*, **21**, 3–24. 25

Chen, Y. & Swamidas, A. (1994). Dynamic characteristics and modal parameters of a plate with a small growing surface cracks. In *Proceedings of the 12th International Modal Analysis Conference*. 83

Doebling, S., Farrar, C. & Cornwell, P. (1997). DIAMOND: A graphical user interface toolbox for comparative modal analysis and damage identification. In *Proceedings of the 6th International Conference on Recent Advances in Structural Dynamics*. 85

Dowell, E. & Hall, K. (2001). Mode of fluid-structure interaction. *Annu. Rev. Fluid Mech.*, **33**, 445–490. 22

Duggal, A. & Niedzwecki, J. (1995). Dynamic response of a single flexible cylinder in waves. *Journal of Offshore Mechanics and Artic Engineering*, **117**, 99–104. 43

Dutsch, H., Durst, F., Becker, S. & Lienhard, J.H. (1998). Low-Reynolds-number flow around an oscillating circular cylinder at low Keulegan-Carpenter numbers. *Journal of Fluid Mechanics*, **360**, 249–271. 21

Etienne, S. (1999). *Contribution a la modelisation de l'ecoulement de fluide visqueux autour de faisceaux de cylindres circulaires*. Ph.D. thesis, Universite de la Mediterranee, Aix-Marseille, France. 32

Farrar, C. & James, G. (1997). System identification from ambient vibration measurements on a bridge. *Journal of Sound and Vibration*, **250**, 1–18. 81

Farrar, C. & Jauregui, D. (1996). Damage detection algorithms applied to experimental and numerical modal data from the I-40 bridge. Tech. rep., Technical Report LA-13074-MS, Los Alamos National Laboratory. 83

FLUENT (2007). *User's Guide, Version 6.3*. 50, 52

Gabbai, R. & Benaroya, H. (2005). An overview of modeling and experiments of vortex-induced vibration of circular cylinders. *Journal of Sound and Vibration*, **282**, 575–616. 23, 27

GAMBIT (2007). *User's Guide. Version 2.2*. 50

Guo, H. & Lou, M. (2008). Effect of internal flow on vortex-induced vibration of risers, in press. 10

Hartlen, R. & Currie, I. (1970). Lift oscillation mode for vortex-induced vibration. *Journal of Engineering Mechanics ASCE*, **96**, 577–591. 21

Henderson, R. (1995). Details of the drag curve near the onset of vortex shedding. *Phy. Fluids*, **7(9)**, 2102–2104. 13

Herfjord, K. & Kvamsdal, S.D.T. (1999). Assessment of vortex-induced on deepwater risers by considering fluid structure interaction. *ASME Journal of Offshore Mechanics and Artic Engineering*, **121**, 207–212. 32

Hong, Y. & Koterayama, K. (2004). Numerical simulation scheme for dynamics of flexible riser and its validation by forced oscillations experiments. *International Journal of Offshore and Polar Engineering*, **14(2)**, 110–117. viii, 35, 36, 37, 38, 39

Huera-Huarte, F., Bearman, P. & Chaplin, J. (2006). On the force distribution along teh axis of a flexible circular cylinder undergoing multi-mode vibrations. *Journal of Fluids and Structures*, **22**, 897–903. 39, 48

Inman, D.J., Farrar, C.R., Lopez, V. & Steffen, V. (2005). *Damage Prognosis for Aerospace, Civil and Mechanical Systems*. John Wiley and Sons, Ltd. 79

Juang, J. & Pappa, R. (1985). An eigensystem realization algorithm for modal parameter identification and model reduction. *Journal of Dynamic Systems, Measurement and Control ASME*, **8**, 620–627. 82

Jung, D., Park, H., Koterayama, W. & Kim, H. (2005). Vibration of a highly flexible hanging pipe in calm water. *Ocean Engineering*, **32**, 1726–1739. 43, 44

Kammer, D. (1991). Sensor placement for on-orbit modal identification and correlation of large space structures. *Journal of Guidance, Control and Dynamics*, **14(2)**, 251–259. 99

Khalak, A. & Williamson, C. (1999). Motions, forces and mode transitions in vortex-induced vibrations at low mass-damping. *Journal of Fluids and Structures*, **13**, 813–851. 25, 30, 33, 42, 43, 47

Kim, W. & Perkins, N. (2003). Coupled slow and fast dynamics of flow excited elastic cable systems. *Journal of Vibration and Acoustics*, **125**, 155–161. 24, 25

Koterayama, W. & Nakamura, M. (1988). Wave forces acting on a moving cylinder. *Journal of Offshore Mechanics and Artic Engineering ASME*, **110**, 315–319. 38

Lambrakos, L.F.K. & Maher, J. (1999). Time domain prediction of riser viv. In *Proceedings of the 4th International Conference on Advances in Riser Technologies*. 32

Larsen, C. (2000). *VIVANA Theory Manual MARINTEK 513102.01, Trondheim, Norway*. 32

Lienhard, J.H. (1966). Synopsis of lift, drag and vortex frequency data for rigid circular cylinders. Tech. rep., Washington State University, College of Engineering, Research Division Bulletin 300. viii, 13, 15

Lin, K. & Skeleton, R. (1993). Q-Markov covariance equivalent realization and its application to flexible structural identification. *Journal of Guidance, Control and Dynamics ASME*, **16**, 308–319. 82

Lin, X., Bearman, P. & Graham, J. (1996). A numerical study of oscillatory flow about a circular cylinder for low values of Beta parameter. *Journal of Fluids and Structures*, **10**, 501–526. 18, 19, 47, 48, 52, 72, 76

Lucor, D., Mukundan, H. & Triantafyllou, M. (2006). Riser modal identification in CFD and full-scale experiments. *Journal of Fluids and Structures*, **21**, 335–361. 92

Lynch, J. (2002). *Decentralization of Wireless Monitoring and Control Technologies for Civil Structures*. Ph.D. thesis, Stanford University. 110

Moe, G., Arntsen, O. & Hoen, C. (2001). VIV analysis by complex modes. In *Proceedings of the 11th International Offshore and Polar Engineering Conference*. 32

Morison, J., O'Brien, M., Johnson, J. & Schaaf, S. (1950). The force exerted by surface waves on piles. *Petrol. Trans. AIME*, **189**, 149–154. 17

Morse, T. & Williamson, C. (2006). Employed controlled vibrations to predict fluid forces on a cylinder undergoing vortex-induced vibration. *Journal of Fluids and Structures*, **22**, 877–884. 56, 66

Neumaier, A. & Schneider, T. (2001). Estimation of parameters and eigenmodes of multivariate autoregresive models. *ACM Transactions on Mathematical Software*, **27**, 27–57. 86

Norberg, C. (2003). Fluctuating lift on a circular cylinder: Review and new measurements. *Journal of Fluids and Structures*, **17**, 57–96. 14, 16, 30, 49

Obasaju, E., Bearman, P. & Graham, J. (1988). A study of forces, circulation and vortex patterns around a circular cylinder in oscillating flow. *Journal of Fluid Mechanics*, **196**, 467–494. 19, 29, 35, 36, 41, 44, 47, 52, 53, 58, 59, 70

Ohtsubo, H. & Sumi, Y. (2000). *Proceedings of the 14th International Ship and Offshore Structures Congress*. Elsevier. 9, 78

Pandey, A., Biswas, M. & Samman, M. (1991). Damage detection from changes in curvature mode shapes. *Journal of Sound and Vibration*, **145**, 321–332. 83

Pantazopoulos, M. (1994). Vortex-induced vibration parameters: Critical review. *Offshore Technology ASME OMAE*, **1**, 199–255. 5, 21, 22, 24

Park, H., Jung, D. & Koterayama, W. (2003). A numerical and experimental study on dynamics of a towed low tension cable. *Applied Ocean Research*, **25**, 289–299. 42

Phan, M., Juang, J. & Longman, R. (1990). Identification of linear systems from one set of input-output data via an asymptocally stable ARMA model by eigenvalue assignment. In *Proceedings of the 2nd NASA/USAF Workshop on System Identification and Health Monitoring of Precision Space Structures*. 82

Pickering, P., Hewitt, G., Watson, M. & Hale, C. (2001). The prediction of flows in production risers - truth and myth. In *IIR Conference*. 10

Quan, Q. & Weiguo, Z. (1998). Damage detection of suspension bridges. In *Proceedings of the 16th International Modal Analysis Conference*. 83

Rakshit, T., Atluri, S. & Dalton, C. (2008). VIV of a composite riser at moderate Reynolds number using CFD. *Journal of Offshore Mechanics and Artic Engineering ASME*, **130**, 1–10. 9

Rytter, A. (1993). *Vibration-based Inspection of Civil Engineering Structures*. Ph.D. thesis, Aalborg University, Denmark. 79

Saint-Marcoux, J. (2004). Meeting the callenges of ultra deep water riser systems. In *INTSOK Pipeline and Riser Workshop*. 5, 6, 8

Sarpkaya, T. (1977a). Inline and transverse forces on cylinders in oscillatory flow with high Reynolds numbers. *Journal of Ship Research*, **21**, 200–216. 18

Sarpkaya, T. (1977b). Transverse oscillations of a circular cylinder in uniform flow - part I. Tech. rep., Naval Post-Graduate School Technical Report No. NPS-69SL77071-R. 21

Sarpkaya, T. (1978). Fluid forces on oscillating cylinders. *ASCE Journal of Waterway, Port, Coastal, and Ocean Division*, **104**, 275–290. 25, 26

Sarpkaya, T. (1995). Hydrodynamic damping, flow-induced oscillations and biharmonic response. *Journal of Offshore Mechanics and Artic Engineering ASME*, **117**, 232–238. 21, 41

Sarpkaya, T. (2004). A critical review of the intrinsic nature of vortex-induced vibrations. *Journal of Fluids and Structures*, **19**, 389–447. 28, 41, 42, 59

Scholkopf, B., Smola, A. & Muller, K. (1998). Nonlinear component analysis as a kernel eigenvalue problem. *Neural Computation*, **10**, 1299–1319. 85

Senga, H. & Koterayama, W. (2005). An experimental and numerical study on vortex-induced vibrations of a hanging flexible riser with its top in irregular motion. *International Journal of Offshore and Polar Engineering*, **15(4)**, 274–281. viii, 36, 38, 39, 88, 90, 91

Skop, R., Griffin, O. & Ramberg, S. (1977). Strumming predictions for the Seacon II experimental mooring. In *Offshore Technology Conference OTC 2884*. 25

Sohn, H., Farrar, C., Hunter, N. & Worden, K. (2001). Structural health monitoring using statistical pattern recognition techniques. *Journal of Dynamic Systems, Measurement and Control ASME*, **123**, 706–711. 86, 87

Sohn, H., Farrar, C., Hemez, F., Shunk, D., Stinemates, D. & Nadler, B. (2003a). A review of structural health monitoring literature: 1996-2001. Tech. rep., LA-13976-MS. 86

Sohn, H., Farrar, C., Hunter, N. & Worden, K. (2003b). Statistical damage classification using sequential probabibility ratio tests. *Journal of Structural Health Monitoring*, **2(1)**, 57–74. 102

Stubbs, N., Kim, J. & Farrar, C. (1995). Field verification of a nondestructive damage localization and severity estimation algorithm. In *Proceedings of 13th International Modal Analysis Conference*. 83, 84

Sworn, A. (2005). Hybrid riser tower from an operator's perspective. In *Offshore Technology Conference OTC 17397*. 5, 8

Tang, J. & Leu, K. (1991). Vibration tests and damage detection of p/c bridge. *Journal of the Chinese Institute of Engineers*, **14**, 531–536. 83

Toshiba, M. & Saito, E. (1984). Structural identification by extended Kalman filter. *Journal of Engineering Mechanics ASCE*, **110**, 1757–1770. 82

Triantafyllou, M. (2003). *VIVA Extended User's Manual, Massachusetts Institute of Technology, Deparment of Ocean Engineering, Cambridge, MA, USA*. 32

Trim, A., Braaten, H., Lie, H. & Tongnarelli, M. (2005). Experimental investigation of vortex-induced vibration of long marine risers. *Journal of Fluids and Structures*, **17**, 1213–1236. 89

Valdes, V. & Ortega-Ramirez, R. (2000). Issues and challenges in the requalification of offshore platforms in Mexico. *Journal of Offshore Mechanics and Arctic Engineering ASME*, **122**, 65–71. 78

Vandivier, J. (1983). Drag coefficients of long flexible cylinders. In *Offshore Technology Conference OTC 4409*. 25, 30

Vandivier, J. (1998). Research challenges in the vortex-induced vibration prediction of marine risers. In *Offshore Technology Conference OTC 8698*. 107

Vandivier, J. (2003). *User's Guide for SHEAR7, , Massachusetts Institute of Technology, Deparment of Ocean Engineering, Cambridge, MA, USA*. 32

Willden, R. & Graham, J. (2004). Multi-modal vortex-induced vibrations of a vertical riser pipe subject to a uniform current profile. *European Journal of Mechanics B/Fluids*, **23**, 209–218. 32

Willden, R. & Graham, J. (2006). Three-distinct response regimes for the transverse vortex-induced vibrations of circular cylinders at low Reynolds numbers. *Journal of Fluids and Structures*, **22**, 885–895. 43, 59

Williams, D., Harte, A. & Grealish, F. (2005). Development of an analytical tool for the design of deep water riser/flow line thermal insulation systems. *Journal of Offshore Mechanics and Artic Engineering ASME*, **127**, 96–103. 10

Williamson, C. (1985). Sinusoidal flow relative to circular cylinders. *Journal of Fluid Mechanics*, **155**, 141–174. 19

Wu, J. (1981). Theory for aerodynamic force and moment in viscous flows. *AIAA Journal*, **19**, 4332–4441. 18

Yam, L., Leung, T., Li, D. & Xue, K. (1996). Theoretical and experimental study of modal strain energy. *Journal of Sound and Vibration*, **191**, 251–260. 83

Yamamoto, C., Meneghini, J., Saltara, F., Fregonesi, J.A. & Ferrari., J. (2004). Numerical simulations of vortex-induced vibration on flexible cylinders. *Journal of Fluids and Structures*, **19**, 467–489. 32

Zdravkovich, M. (1982). Modification of vortex shedding in the synchronization range. *Journal of Fluids Engineering*, **104**, 513–517. 22

Zhang, L., Kanda, H., Brown, D. & Allemang, R. (1985). A polyreference frequency domain method for modal parameter identification. Tech. rep., ASME-85-DEC-106, American Society of Mechanical Engineers. 82

Zhou, C. & Graham, J. (2000). A numerical study of cilinders in waves and currents. *Journal of Fluids and Structures*, **14**, 403–428. 18, 19, 44, 49, 51